UNIVERSITY OF THE WITWATERSRAND, JOHANNESBURG
SCHOOL OF MECHANICAL, INDUSTRIAL AND AERONAUTICAL ENGINEERING

Research Report (MECN 7018)

Title: Solid Particle Erosion of Ductile and Brittle Materials at Coal Fired Power Plants
Name: Hebendran Padayachee
Student Number: 1284486
Date: 17 June 2020

Abstract

Solid particle erosion is a major concern in coal fired power plants around the world. Failure due to solid particle erosion has an impact on power plants to produce electricity especially in South Africa where load shedding has had a significant bearing on the economy.

The aim of this research is to perform solid particle erosion experiments on commercially available erosion protection materials and then rank these materials in terms of its erosion resistance, this will enable the coal fired plant design and/or maintenance team to select the most appropriate erosion protection material/s for different coal fired power plant applications. The erosion value is defined as the volume loss of specimen material divided by the total mass of abrasive particles that impacted the specimen. The erosion value is reported as (mm^3/g).

Five pre-selected wear resistant materials were selected for this research. All experiments were performed using an ambient temperature solid particle erosion rig. The aluminium oxide (Al_2O_3) abrasive was selected for the experiments based on Quantitative Evaluation of Minerals by Scanning Electron Microscopy (QEMSCAN) results.

For carbon steel and VRN 400 (ductile materials), the maximum erosion value was observed at an impact angle of 30° and as the impact angle increases from 30° to 90°, the erosion value decreases. For 92% and 96% alumina tile (brittle materials), the maximum erosion value was observed at an impact angle of 90° and as the impact angle increased from 30° to 90°, the erosion value increased. For 316L stainless steel (semi-ductile material), the maximum erosion value was observed at an impact angle of 60°.

During the Scanning Electron Microscopy (SEM) analysis it was observed that room temperature erosion of carbon steel materials is due to cutting wear and plastic deformation. For brittle materials, pitting/pores was observed and as the impact angle is increased from 30° to 90°, the pitting/pores are observed to be more prominent and for semi-ductile materials, similar morphologies to ductile materials was noted.

The ranking of the pre-selected materials for each material in terms of best erosion protection material to worst erosion protection material from this research is as follows:

At 30° impact angle: 316L stainless steel > 96% alumina > VRN 400 > 92% alumina > carbon steel

At 60° impact angle: VRN 400 > 316L stainless steel > 96% alumina > carbon steel > 92% alumina

At 90° impact angle: VRN 400 > 316L stainless steel > carbon steel > 96% alumina > 92% alumina

Acknowledgements

I wish to thank all of those who assisted me throughout this project, but in particular:

- God, for the guidance and strength throughout the duration of this project.
- My supervisors, Prof Walter Schmitz and Dr Richard Curry for their excellent guidance, advise and support throughout this project.
- Mr Chris Du Toit and Mr Preeya Sukdeo from Eskom for their support and guidance in the initial stages of this research project.
- Mrs Soraya Abrahams from UCT for her assistance with SEM.
- Dr Chris Van Alphen for his assistance with QEMSCAN.
- Mr Jordaan Lourens from Thermaspray (SA) for accommodating and arranging for me to use the solid particle erosion rig at their facilities.

A special dedication to my dear wife and parents, for their love, support, encouragement and for their constant support over the years. A dedication to my late grandmother (passed away on 31/07/2019) who played a pivotal role in my life during my childhood.

Contents

List of Figures

List of Tables

Terminology

Definitions

Abrasive flow rate $(\mathrm{g/min})$	Quantity of the abrasive in grams per minute.
Erosion value $(\mathrm{mm^3/g})$	The volume loss of specimen material divided by the total mass of abrasive particles that impacted the specimen. The erosion value is volume based and, in the literature review, it is sometimes referred to as the erosion rate.
Erosion rate $(\mathrm{mg/g})$	The ratio of the mass loss of the specimen to the mass of erodent particles
FEM	The simulation of any given physical phenomenon using the numerical technique called Finite Element Method (FEM)
Normalized Erosion Rate	The normalized erosion rate is the erosion value $(\mathrm{mm^3/g})$ of specimen material divided by erosion value $(\mathrm{mm^3/g})$ of reference material
QEMSCAN	Quantitative Evaluation of Materials by Scanning Electron Microscopy is an automated mineral analyser. It is an analytical tool which provides rapid, reproducible and statistically reliable quantitative information on minerals and certain man-made materials for a variety of disciplines [48]
SEM	Scanning Electron Microscopy. It is microscopy that uses electrons rather than light to form an image. The SEM has a large depth of field which allows a large amount of sample to be in focus at a given time.
Specimen density $(\mathrm{g/cm^3})$	It is a quantitative expression of the amount of mass contained per unit volume.
UCLF	Unplanned Capacity Loss Factor

List of symbols

°C	degrees Celsius
α	angle of impact
σ_y	yield stress
ρ	rho (density)
ρ_p	particle density
ε	power law
µm	micrometres
Al_2O_3	aluminium oxide
c	particle shape factor
d_p	diameter
E_R	erosion rate
E_1	kinetic energy
g	grams
h	depth of penetration
H_t	material hardness
kg	kilograms
K_{Ct}	material toughness
kPa	kilo pascals
m_p	mass of particle
m	metres
mg	milligrams
mm	millimetres
N	Newtons
Ra	Surface roughness
R_p	particle size
s	seconds
$Si0_2$	silica sand
t	time
V	volume loss
v	velocity
W	weight

Chapter 1: Introduction

1.1. Problem statement

Coal fired power plants across the world have plant areas that are susceptible to erosive wear damage. These susceptible locations have been identified primarily in areas exposed to Pulverised Fuel (PF) and fly ash. The coal that is used in power plants in South Africa (SA) is mined from different parts of the country. Different coal sources provide SA power plants with different characteristics of coal. This coal is milled into fine powder via coal mills in the power plant. This fine powder is commonly called PF. The PF is then transported from the mills to the burners via ducting. The PF is then burnt in the boiler and hot flue gasses with fly ash are produced. This fly ash then moves through the boiler and as it travels through the boiler it loses energy and the particle velocity is reduced. The hot flue gas then passes through air heaters.

Coal quality plays a major role in affecting the erosion value. Silica (SiO_2) content in coal affects the erosive wear rate of components in coal fired power plants [4]. Fly ash in South Africa (SA) is rich in ash because of the local coal quality. Other variables that affect the erosion value in power plants include particle velocity, impact angle, particle size and particle shape.

Specific plant locations susceptible to erosive wear at coal fired power plants include burners, ducts, re-heaters, economisers, mills, PF pipes and air heaters to name a few. The areas affected by erosive wear are often on the PF scroll and PF pipe sections. The air heater inlet has been identified as a highly erosive area by power plants in SA. The areas in the boiler that are prone to fly ash erosion can be fitted with protection shields and/or deflector plates to reduce the erosion damage. Mills and PF pipes are also highly prone to erosion.

Wear protection materials for different plant areas (i.e. different applications) need to be tested to determine the most suitable wear protection material for each application; the cost, environment such as temperature and velocity, installation, inspection methods/technology and maintenance must be considered when selecting a suitable wear protection material.

Using suitable wear protection material/s in high erosive areas of power plants can increase the life and operation of the power plant. Increasing plant component life assists to reduce un-planned outages and indirectly helps to alleviate load shedding which currently has a significant bearing on the economy of SA.

The selection of a suitable wear protection material based on experimental test results can reduce the amount of Unplanned Capacity Loss Factor (UCLF), down-time and repair/replacement costs. Testing a variety of commercially available erosive wear resistant materials for different erosion

applications at a power plant will improve the erosion resistant materials knowledge allowing each power plant to select the most suitable material/s for a specific erosion application which will result in significant cost, time and safety benefit.

1.2. Objectives of this study

I. To perform solid particle erosion experiments on commercially available erosion protection materials and then rank these materials in terms of its erosion resistance, this will enable the coal fired plant design and/or maintenance team to select the most appropriate erosion protection material/s for different coal fired power plant applications.

II. To add to the international knowledge base of material wear protection characteristics by testing new materials that have not been published in open literature.

Chapter 2: Literature Review

2.1. Theories and models of erosion

The erosion of materials as the result of the impact of solid particles is a discrete and cumulative process involving prolonged periods of exposure under steady state or variable conditions. This form of wear is a complex phenomenon consisting of several simultaneous and interactive processes. A simplified approach to the problem consists in separating the effects due to the operative variables. Variables affecting the erosion rate can be broadly broken down into three types as listed and described below:

I. impingement variables describing the particle flow,

II. particle variables,

III. material variables [1]

The impingement variables are [1]

- particle velocity v,
- angle of impact α (frequently named attack angle being the angle between the particle velocity and the material surface),
- particle concentration.

Particle variables include [1]

- particle shape,
- particle density ρ_p,
- particle size R_p.
- particle hardness.

Material variables include all the target material mechanical properties [1]

- Young's modulus E_t, Poisson's modulus v_t,
- hardening behaviour and the microstructure,
- hardness H_t,
- toughness K_{Ct},
- grain size,
- structure of the material.

2.2. Mechanisms of erosive wear

The primary mechanisms of erosive wear are, erosion due to cutting wear (micro-machining action), repeated plastic deformation wear and weakening of tensile properties of the steel component at elevated temperature. The erosion at room temperature is due to cutting wear and plastic deformation as mentioned by Mbabazi et al [4].

2.2.1. Cutting wear

When a particle strikes the target material surface at an acute angle and at a higher velocity than the critical velocity needed for the penetration of the surface of the material, this results in the removal of some of the material. This removal process of the material is similar to the cutting action of a machine tool. At the point of impact, the particle loses a fraction of its kinetic energy to the target material in the form of heat and energy. Very high levels of shear strain may be induced in the material at this point. When the shear strain exceeds the elastic strain limit of the target material, the particle penetrates and ploughs through the surface, thus, removing material. It is assumed that the stresses acting at the contact point are constant during the wear process. The particle penetrating the surface of the material must overcome the material's resistance to deformation. The dynamic equation representing the depth of penetration (h) of a particle of mass (m_p) and diameter (d_p) as it penetrates through the surface of a material is given by the following differential equation [4]

$$m_p \frac{d^2h}{dt^2} = -\pi \frac{d_p}{2} hc\sigma_y \quad (1)$$

where t is the time, σ_y is the yield stress of the target material, c is a particle shape factor equal to 3 for a sphere and $m_p = \frac{1}{6} \rho_p \pi {d_p}^3$

2.2.2. Plastic deformation wear

During particle impact, the loss of material from an eroding metal surface is attributed to a combined extrusion-forging mechanism. Platelets are initially extruded from shallow craters made by the impacting particle. The high strain rate result in adiabatic shear heating in the surface region immediate to the impact site. A work-hardened zone forms beneath the immediate surface region. This is because, the kinetic energy of the impacting particles is enough to result in a considerably greater force being imparted to the metal than is required to generate platelets on the surface. The work-hardened zone reaches its stable hardness and thickness, which leads to steady-state erosion once the surface, is completely converted to platelets and craters. The reason that the steady-state erosion rate is the highest rate is that the subsurface cold-worked zone acts as an anvil, thereby increasing the efficiency of the impacting particles to extrude-forge platelets in the now highly strained and most deformable surface region. This cross-section of material moves down through the metal as erosion loss occurs. In the platelet mechanism of erosion, there is a localised sequential extrusion and forging of metal in a ductile manner, leading to removal of the micro-segments thus formed. During plastic deformation, the normal component of the particle's kinetic energy is used to extrude-forge the material. The normal component of the kinetic energy (E_1) of the particle is given by [4]

$$E_1 = \frac{1}{2}\frac{\pi {d_p}^3}{6}\rho_p V^2 \sin^2\alpha = \frac{\pi}{12}\rho_p {d_p}^3 V^2 \sin^2\alpha \quad (2)$$

Where d_p and ρ_p are the particle diameter and density, respectively, and V and α are the particle incident velocity and angle, respectively.

Removal of material occurs through the processes of micro-plastic deformation and/or brittle fracture. For ductile materials such as pure metals and alloys, the impact of the hard particles causes severe, localized plastic strain at the impact site on the surface. Material is removed when the strain exceeds the material's strain-to-failure. For brittle materials, such as ceramic and intermetallic compounds, the force of the impacting particle causes localized cracking at the surface [14]. These cracks propagate and eventually link together due to subsequent impact events and as a result the material becomes detached from the surface [15]. Therefore, the particle impingement angle on the surface affects each material in a different manner.

2.3. Angle of impingement of the abrasive

The angle of impingement is the angle between the particle velocity and the material surface. Material loss for ductile metals tends to peak at an oblique angle of impact, typically between 20° and 30°. However, material loss for brittle materials tends to increase with increasing impingement angle with maximum material loss occurring at 90° [16]. Alman's [17] studies on both ceramics and metals suggest that the attack angle is the best indicator for the erosion mechanism. Ductile materials exhibit maximum erosion rates at attack angles of about 20° - 40° while brittle materials exhibit a maximum erosion rate at an angle of 90°.

Das et al [2] developed a mathematical model to characterize the effect of silica content in boiler fly ash on erosion behaviour of boiler grade steel. The effect of silica content on the erosion rate of boiler grade steel at various impact angles are shown in Figure 1. The results show that a minor increase in the silica content level in fly ash can considerably aggravate the erosion rates of boiler grade steel. The silica content in fly ash plays a critical role in characterising erosion potential of fly ash - it was noted that a 15% increase in silica content of the fly ash has a significant impact on the erosion rate, which increased by more than 200% under similar particle impact conditions.

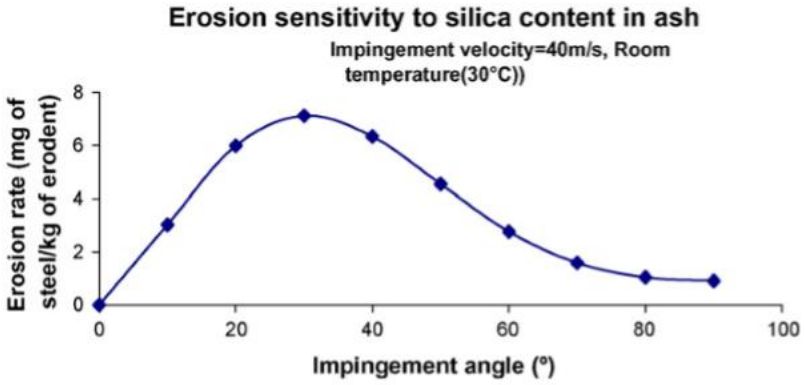

Effect of silica content on the erosion rate (1.25Cr–1Mo–V steel) (silica content = 55%, impingement velocity = 40 m/s, at room temperature).

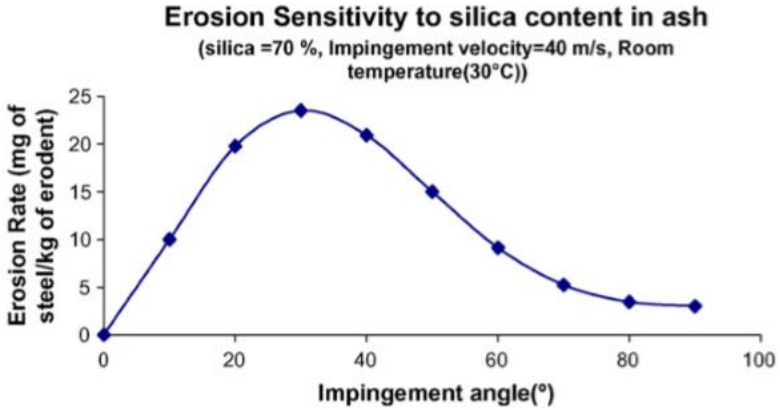

Effect of silica content on the erosion rate (1.25Cr–1Mo–V steel) (silica content = 70%, impingement velocity = 40 m/s, at room temperature).

Figure 1: Effect of silica content on the erosion rate of boiler grade steel at various impact angles [2]

Raask [3] performed erosion studies on mild steel materials at various impact angles and the erosion rate results from this experimental study is shown in Figure 2. The abrasive material was quartz (125–150 µm) and the impact velocity was 27.5 m/s.

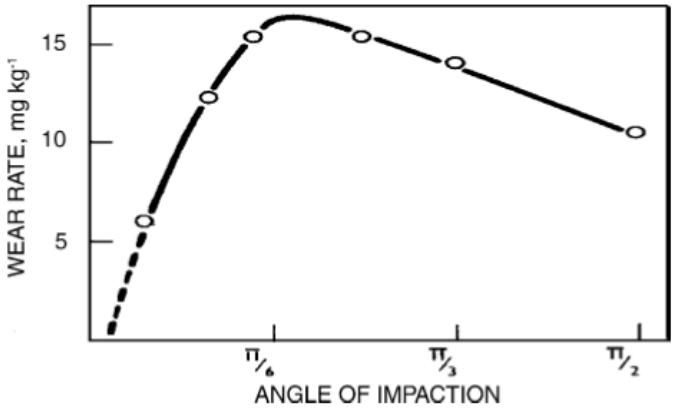

Figure 2: Erosion wear rate of mild steel materials at various impact angles [3]

From erosion studies performed by Mbabazi et al [4], they found that the erosion rate on mild steel and boiler grade steel respectively increases with an increase in the impingement angle, with the maximum erosion rate occurring at an impingement angle of about 30°. Thereafter, the erosion rate decreases with further increase in the impingement angle. The erosion rate for mild steel material at different impact angles for Matimba power station is shown in Figure 3. Mbabazi et al [4] noted via SEM micrographs that the eroded steel surface experienced cutting wear at low particle impingement angles and deformation wear at high angles.

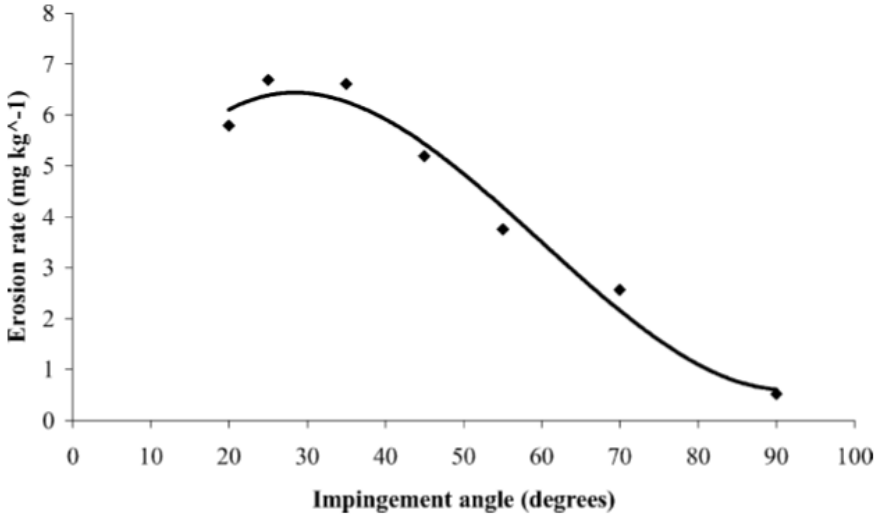

Figure 3: Mild steel erosion rate at various ash particle impingement angles with ash from Matimba: impact velocity 24.77m/s [4]

Yu-Fei Wang and Zhen-Guo Yang [13] developed a Finite Element Model (FEM) on ductile and brittle materials and found that the maximum impact angle appeared at about 30° for ductile materials (Ti - 6Al - 4V alloys) as shown in Figure 4.

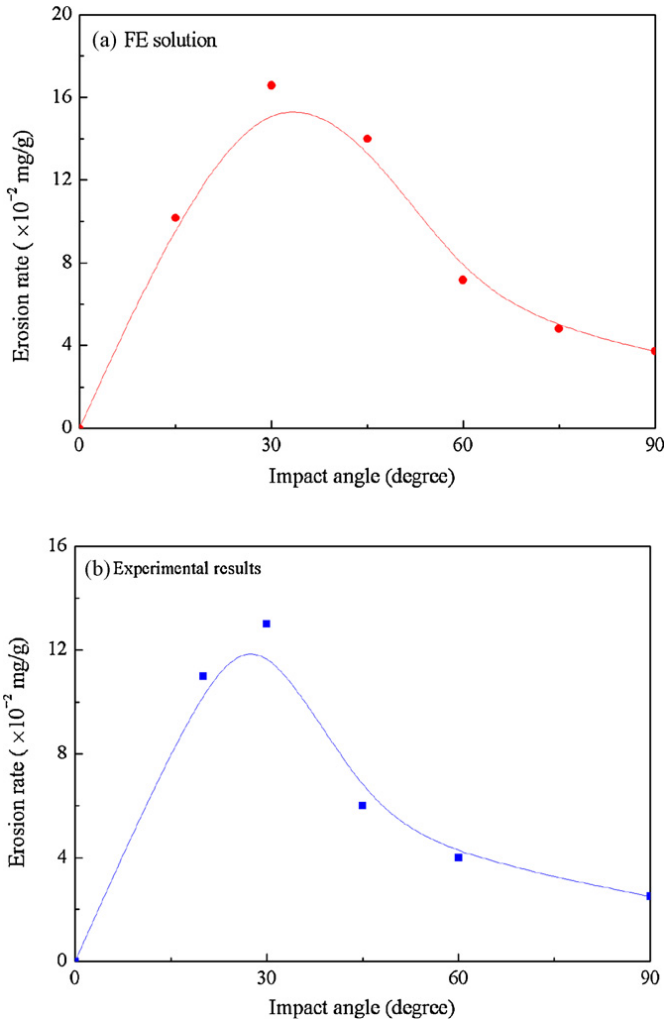

Figure 4: Variation of erosion rate with impact angle for ductile materials [13]

Tabakoff et al [25] performed an erosion study of different materials affected by coal ash particles and found that for all three velocities (as shown in Figure 5) tested in this experiment on 2024 aluminium alloy material, the erosion mass parameter (expressed as milligrams of material eroded per gram of abrasive impacted on the specimen surface) had a maximum value at an angle of attack of approximately 20°. As the angle of attack increases over 20° the erosion reduces to a residual value at 90°.

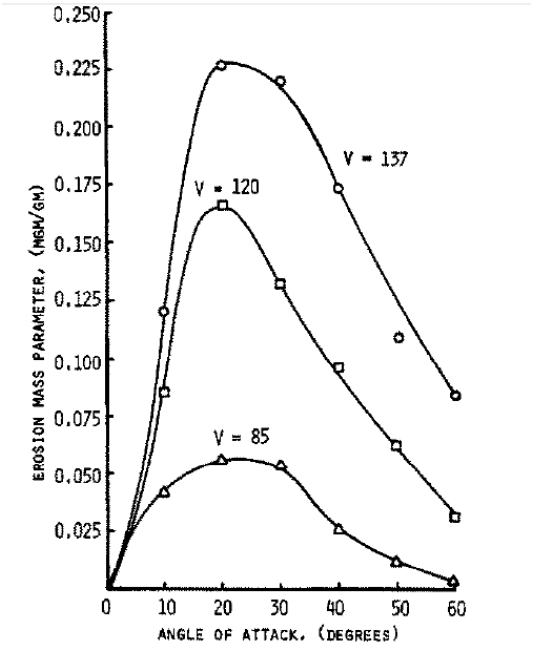

Figure 5: Angle of attack at different particle velocities (m/s) [25]

From studies performed by Shida & Fujikawa [33] the peak impingement angle was at acute impact angles of 20º - 30º as shown in Figure 6**,** with a tendency for the peak impact angle to be slightly higher at 300 ºC than at 650 ºC. The temperature effect was clearly observed in that the erosion rate at acute impingement angles increased significantly with the temperature suggesting that the steel tends to show behaviour characteristic of ductile materials as the temperature is increased [33]

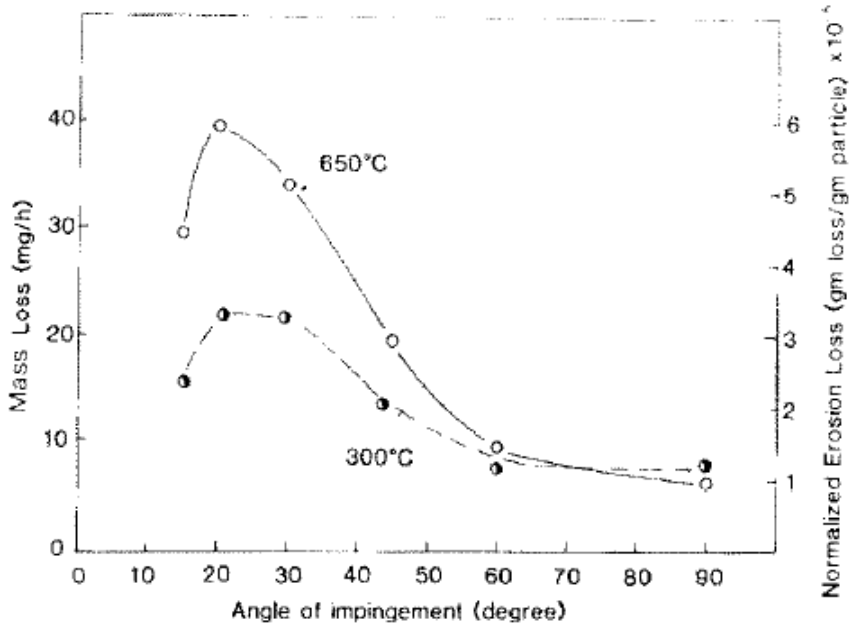

Figure 6: Effect of impingement angle on the erosion mass loss rate obtained for the 304 steel at 300 ºC and 650 ºC (velocity, 120 m/s; particle concentration, 120 g/m^3) [33]

Juan et al [8] investigated solid particle erosion on different metallic materials and found that most the materials displayed a ductile behaviour as their maximum erosion rate was reached at 30º and 45º and reduced considerably near or at 90º. The erosion rate was considerably decreased at higher incidence angles (60°, 75° and 90°) while stainless steels 304 and 316 had higher erosion damage at 60°. Juan et al also noted that wear scars were characterized by an elliptical shape at 30° and 45°, which is a characteristic feature when the specimens are impacted at low-impact angles ($\alpha \leq 45°$), whereas a nearly circular shape was observed at 60° and 90°.

Henk and Miko [19] investigated the ductile–brittle transition in solid particle erosion. They discussed brittle erosion and ductile erosion from their investigation. In the first case, material is removed by crack formation (maximum erosion at 90° impact angle), in the latter case by cutting and ploughing (maximum erosion around 30° impact angle). When very low particle kinetic energies are used to erode brittle targets, the impacts are not powerful enough to initiate cracks and the erosion is ductile instead of brittle. In this study, sharp Al_2O_3 particles for different sizes and velocities (particle size: 3 - 29 µm, velocity: 75 - 200 m/s) on the following three materials: soda lime glass, pyrex and silicon. The transition does not occur suddenly but extends over at least one decade of kinetic energy. During this transition, the kinetic energy exponent becomes much larger [19].

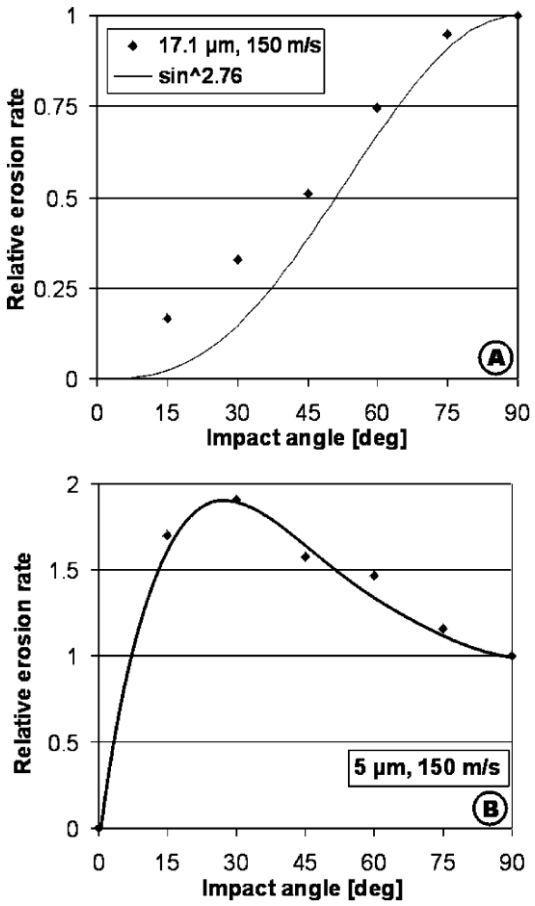

Figure 7: Relative erosion versus impact angle for soda lime glass, brittle (A) and ductile (B) erosion [19]

A study done by Ritesh et al [6] investigated polyester composite materials reinforced with five different glass fibre loading (10, 20, 30, 40 and 50 wt.-%). The results show that the maximum erosion rate occurs at a 60º impact angle while the minimum erosion rate occurs at 30º and 90º impact angles for all composites that was tested. The authors have indicated that these composites respond to solid particle impact which neither shows the brittle nor ductile behaviour but purely shows semi-ductile material behaviour.

Moumakwa and Marcus [11] investigated the long-term solid particle erosion of a range of oxide and nitride-fired SiC-based ceramics and alumina with the aim of reducing erosive wear damage in power plants. They found that the wear rate increases as the impact angle is increased, reaching a maximum at 90° which is the typical behaviour of brittle materials, rather than ductile materials, which have maximum erosion rates between 30° and 60° impact angles. Wang and Yang [13] developed a FE Model on erosive wear on ductile and brittle materials and found that brittle materials exhibit a maximum erosion rate at an angle of 90° as shown in Figure 8 .

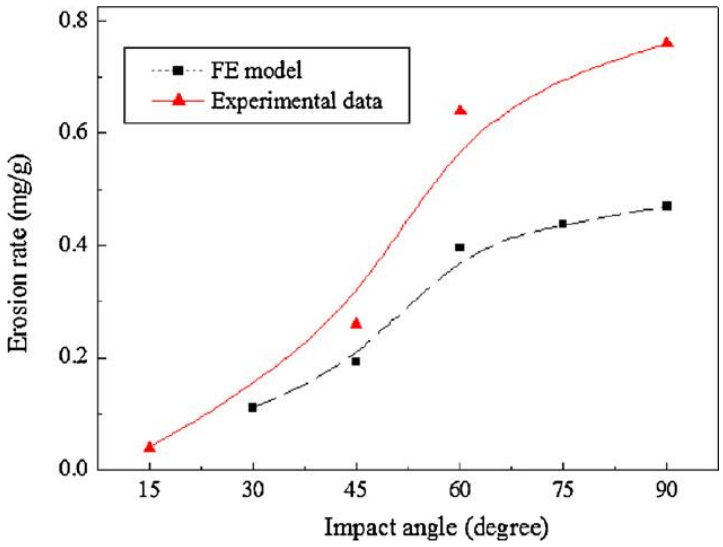

Figure 8: Variation of erosion rate with impact angle for brittle materials [13]

Jianren and Shyam [21] investigated the erosion characteristics of alumina ceramics at high temperatures. The dependence of erosion on impingement angle was examined in this work for Al4Si at 650 °C and at an impact velocity of 50 m/s. The results from this investigation shows (Figure 9) that even at 650 °C erosion rate peaks at 90°. This indicates the dominance of the brittle fracture mechanism in the erosion of the material at as high a temperature as 650 °C.

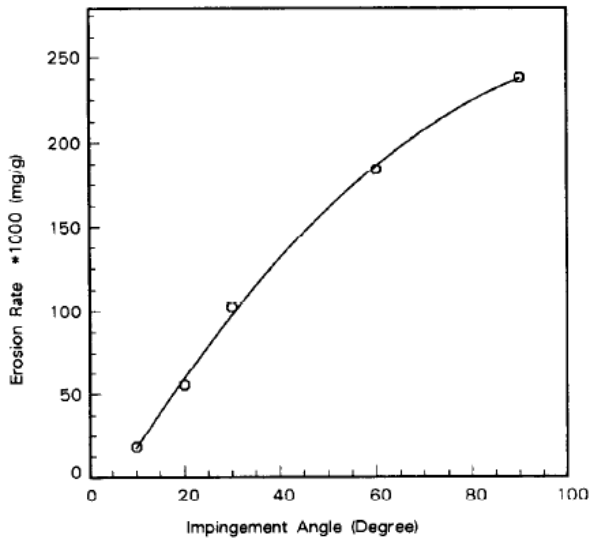

Figure 9: Variation of erosion rate as a function of impingement angle at 650 °C and impingement velocity 50 m/s [21]

Xiaojun Wang [24] investigated solid particle erosion of alumina ceramics at elevated temperature. The results are shown in Figure 10, the brittle alumina ceramics have the maximum erosion rate at

an impingement angle of 90° when eroded at room temperature and 800 °C, which is well consistent with those results in other literature.

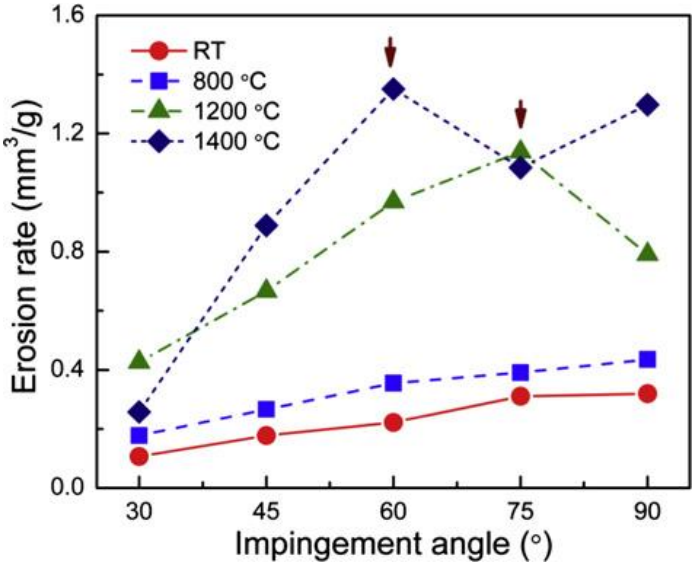

Figure 10: Variation of erosion rate as a function of the impingement angle with different temperatures [24]

2.4. Particle impact velocity and the particle velocity exponent

Tilly and Sage [27] developed a relationship between erosion rate (ε), and velocity (V) by the power law: $\varepsilon = a\, V^{\alpha}$, where a and α are material constants characterizing the relative erosivity and velocity exponent, respectively. They determined that the velocity exponent is close to 2.3 for 125 – 150 µm quartz particles for materials as diverse as plastics, ceramics and metals.

Mbabazi et al [4] developed a model to predict erosion on mild steel surfaces impacted by boiler fly ash particles. Boiler fly ash from Eskom's Matimba (0.2 - 351.48 µm), Matla (0.27 - 258.95 µm) and Lethabo (0.23 - 409.95 µm) power station was measured from a mass spectrometry analysis. The big and amorphous ash particles from Lethabo resulted in the lowest value of the velocity exponent, compared with the small and spherical ash particles from Matla that led to the highest value of the velocity exponent. The particle velocity exponent for Matimba, Matla and Lethabo was 3.09, 3.64 and 2.42 respectively subjected to mild steel (ductile) material. The variation of the erosion rate for mild steel follows a power law with the ash particle impact velocity. The value of the velocity exponent appears to be affected by the size and shape of the ash particles. Large, irregularly shaped particles from Lethabo Power Station resulted in a lower velocity exponent of 2.42 compared to 3.64 that was obtained for the small, rounded particles from Matla Power Station. The velocity

exponent of 3.09 that was obtained with fly ash from Matimba Power Station compares closely with the value of 3 that was derived in a fundamental model to predict erosion of mild steel.

Wang and Yang [13] generated Figure 11 from their FEM. The material used in this model was Ti-6Al-4V alloy (ductile) and the velocity exponent was found to be 2.2691 using 120 µm SiC particles at 30°.

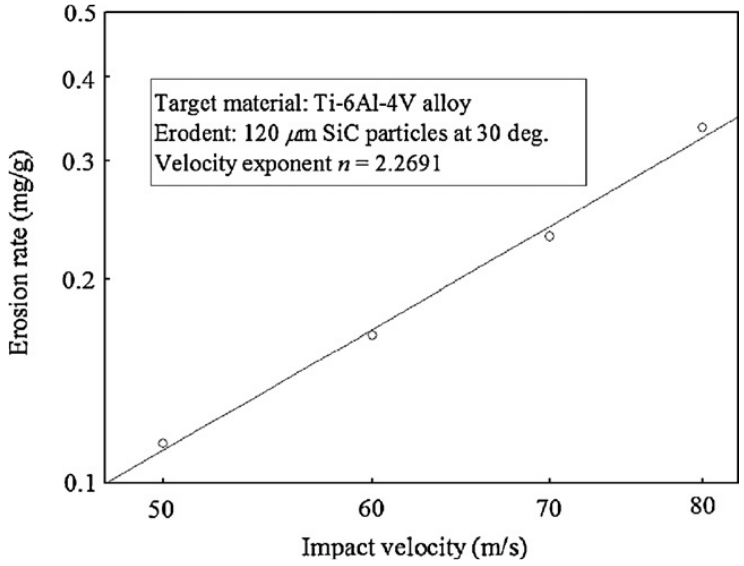

Figure 11: Variation of erosion rate with the impact velocity for ductile materials [13]

Wang and Yang [13] also found that from their FEM that the erosion rate of brittle materials also has an exponent relationship with the impact velocity. Figure 12 compares the FEM and experimental data results; the velocity exponent *n* for silicon carbide target materials via the FEM results was 2.0.

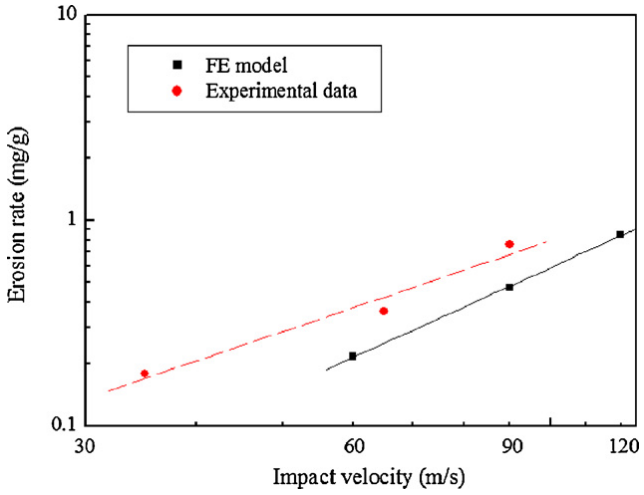

Figure 12: Variation of erosion rate with the impact velocity for brittle materials [13]

Moumakwa and Marcus [11] found that the erosion rates also increased with an increase in particle impact velocity, resulting in a velocity exponent (n) value of 1.5 for Alumina (brittle) material impacted by angular shaped silica sand particles (125 - 180 µm).

Jianren and Shyam [21] studied alumina ceramics (Al4Si) at 650 °C and in normal impact condition and their results are shown in Figure 13. From the straight-line behaviour on log-log scale, the velocity exponent of 1.6 was determined. This value is lower than 2.6 that were obtained for room temperature erosion [19]. The decrease here was attributed to the heating effects associated with large particle impacts. The external heating, as in our case, would also thus be expected to reduce the value of the exponent. The decrease in the value of the velocity exponent for Al_4Si at the elevated temperature is attributed to the dissipation of impact energy by the secondary glassy phase. At high temperatures, the secondary glassy phase softens and so undergoes more plastic deformation upon external impacts. **[21]**

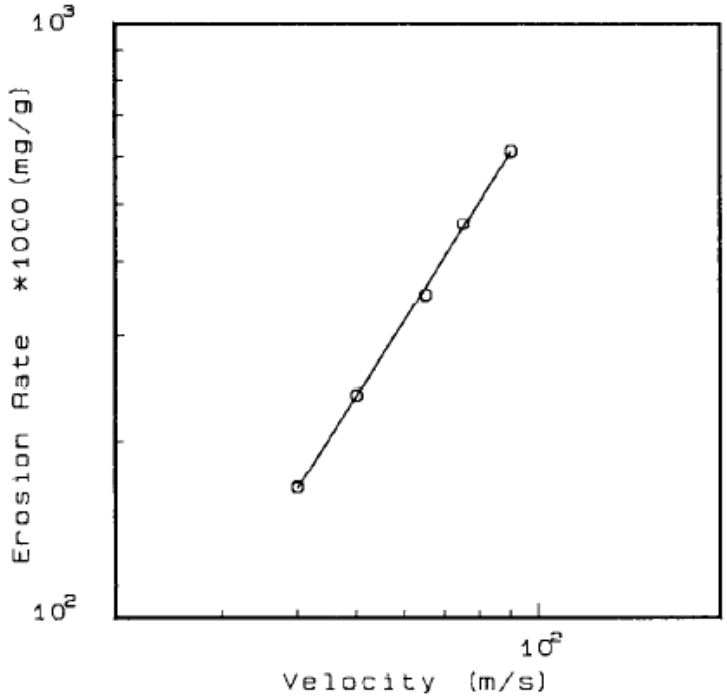

Figure 13: Variation of erosion rate as a function of impingement velocity at 650 °C and normal impact [21]

ElTobgy and Elbestawi [14] developed a FE Model on erosive wear and found that the erosion rate displayed an exponential relationship with particle velocity. The exponent magnitude of 2.25 acquired from the model is very close to those reported in other literature. The erosion rate showed a parabolic trend with the attack angle. This trend was also observed by both analytical models and results acquired experimentally.

Suckling [30] investigated the high temperature erosive wear of boiler tube steel, the effect of particle velocity was found to be substantial. Erosion rates were found to be proportional to the particle velocity raised to an exponent of 1.90 at 20°C for plant fly ash. SiC and SiO_2 velocity exponents were found to decrease slightly with increasing temperature as the steel becomes less sensitive to particle impact due to its decreasing strength and increasing ductility.

From studies performed by Shida & Fujikawa [33] on particle erosion behaviour of typical boiler tube materials at elevated temperatures up to 650°C using irregularly shaped silica particles, it was noted that the velocity exponents obtained at 300 °C and 650°C were both approximately 2.8 although the erosion rate was greater at 650°C than at 300°C as shown in Figure 14.

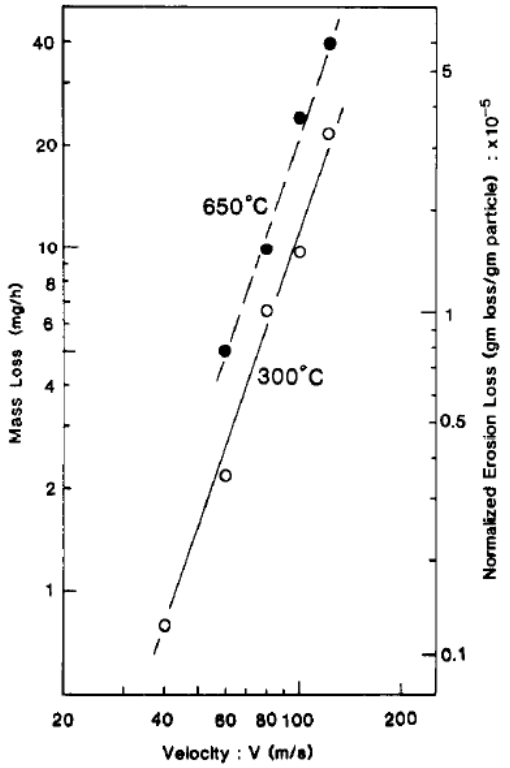

Figure 14: Effect of velocity obtained for the 304 steel at 300°C and 650°C at an impingement angle of 20° and a particle concentration of 120 g/mm^3 [33]

2.5. Particle size, shape and hardness

Mbabazi et al [4] used fly ash from three Eskom power stations and found that the different values of the velocity exponent may be explained in terms of variations in the ash particle sizes and shapes. The big and amorphous ash particles from Lethabo (0.23 - 409.95 µm) resulted in the lowest value of the velocity exponent, compared with the small and spherical ash particles from Matla (0.27 - 258.95 µm) that led to the highest value of the velocity exponent. The size of the ash particles

from Matimba Power Station varied between 0.2 and 351.48 µm, with a mean particle diameter of 57.46 µm. The silica content of the ash particles has a large influence on the erosion rate for mild steel during these experiments.

Tilly and Sage [27] carried out an experiment on titanium alloy and on 11% chromium steel materials to determine the effect of particle concentration on erosion under vacuum. Figure 15 shows two sizes of quartz dust that was used to determine whether the numerical concentration of particles was important, but this made no apparent difference. From Figure 15 it was noted that the smaller particle sizes causes less erosion in comparison to bigger particles sizes for both materials [27].

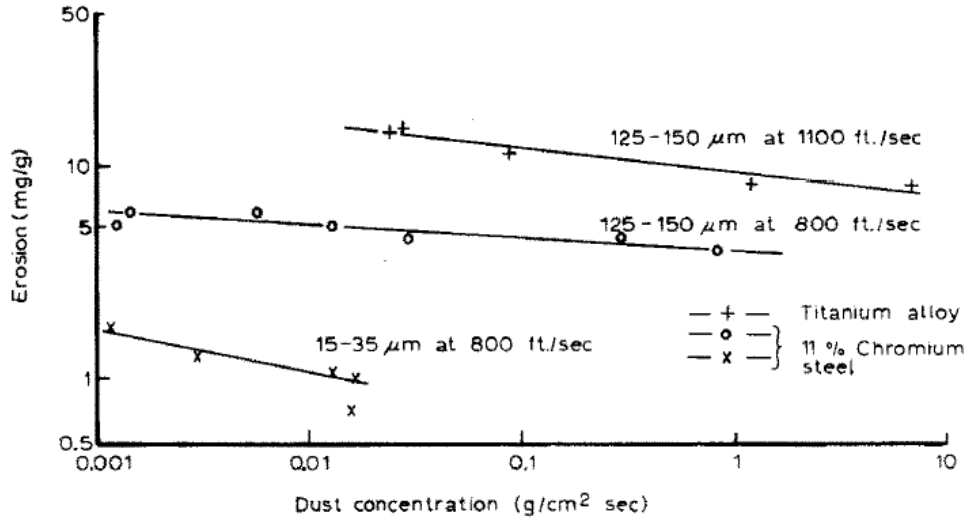

Figure 15: Influence of dust concentration on erosion [27]

Erosion due to quartz particles sizes are shown in Figure 16. It was observed that for steels, erosion peaks and then remains constant once the quartz size reaches 100 µm at a velocity of 800 ft/sec (243.84 m/s). It is also noted that erosion is much less for quartz particle sizes less than approximately 20 µm [27] .

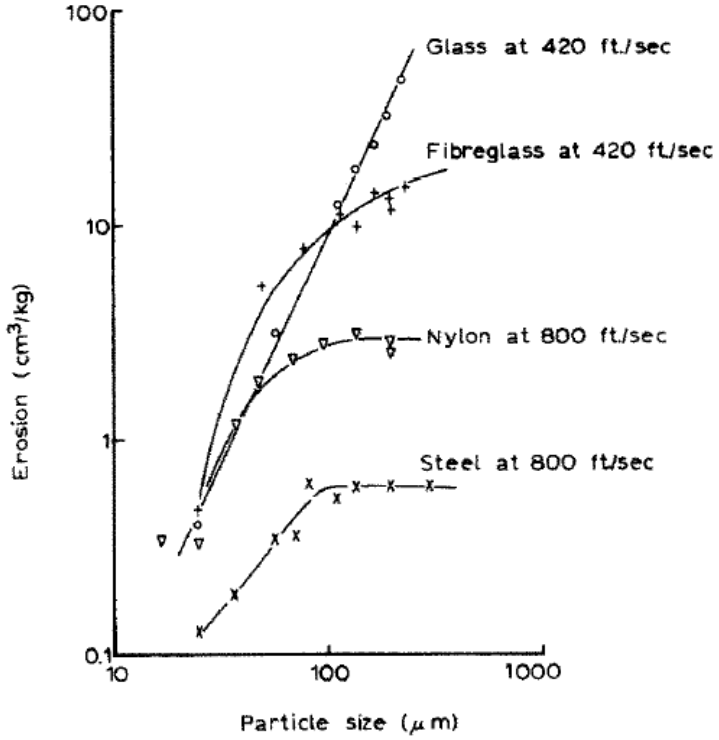

Figure 16: Influence of quartz size on erosion of different types of materials [27]

Tilly [28] and Yerramareddy and Bahadur [29] reported the relationship between the abrasive particles diameters and the erosion rate. They found through experiments that the erosion rate tends to increase considerably at particle size values below about 200 µm. This trend has also been observed through the FE model by Yu-Fei Wang [13] as shown in Figure 17.

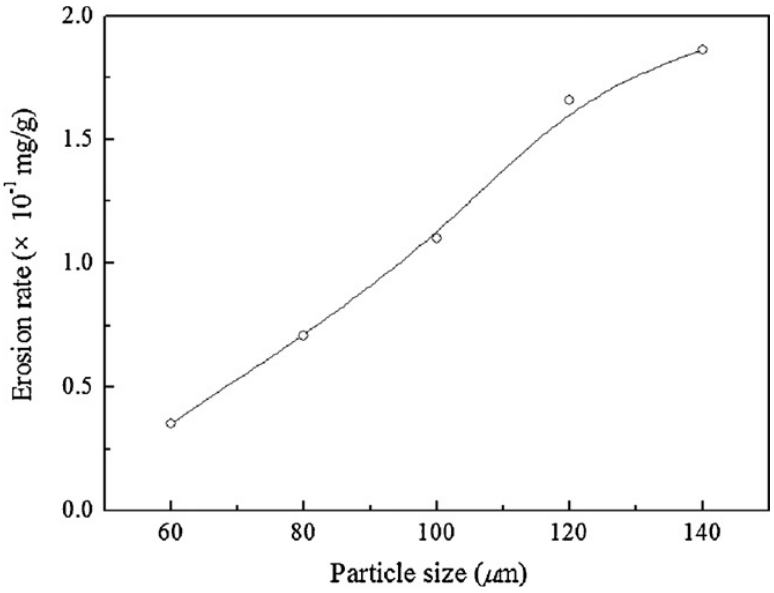

Figure 17: Variation of erosion rate with particle size for ductile materials [13]

Henk and Miko [19] found that when particle speed and size is decreased, eventually the particles are not able to initiate cracking and will only plastically deform the target. This change in erosion mode is called the ductile–brittle transition **[20]**.

Levy and Chik [26] studied the effects of abrasive composition and shape on the erosion of AISI 1020 carbon steel (H_v = 150 $\mathrm{kgf/mm^2}$). They used angularly shaped particles (180 - 250 µm) of five compositions with Vickers' Hardness H_v ranging from 115 to 3000 $\mathrm{kgf/mm^2}$ (Table 1). The effect of particle shape on erosivity was investigated using angular steel grit and spherical steel shot. They determined that the erosion rate increased with increasing particle hardness to a constant rate for particles with H_v > 700 $\mathrm{kgf/mm^2}$. Above 700 $\mathrm{kgf/mm^2}$, mild steel erodes at approximately the same rate regardless of the hardness-strength characteristics of the particle composition. They also noted that angular particles are more erosive than rounded or spherical particles. The hardness was a measure of the friability of the particle composition. When the particles were strong enough not to break up on impacting the AISI 1020 steel surface, the erosion rate became constant. It was also determined by using angular and spherical steel abrasives that angular particles can result in four times more erosion than spherical particles.

Table 1: Abrasive particles and rates of erosion of AISI 1020 steel [26]

Particle composition	**Density (g/cm^3)**	**Mohs hardness**	**Vickers' hardness H_v ($\mathbf{kgf/mm^2}$)**	**Erosion rates ($x10^{-4}$ g/g)**	
				α = 30°	**α = 30°**
$CaCo_3$ (calcite)		3	115	0.03	Not measurable
$Ca_5(Po_4)_3$ (apatite)		5	300	0.5	0.3
$Si0_2$	2.7	7	700	3.0	1.6
Al_2O_3	4.0	9	1900	2.6	1.4
SiC	3.2	> 9	3000	3.3	1.9
Steel grit	7.9			5.3	
Steel shot	7.9			1.4	

The rates for the five brittle abrasives are plotted in Figure 18. It was observed that the erosion rates are very low for the softest materials (calcite and apatite) [26].

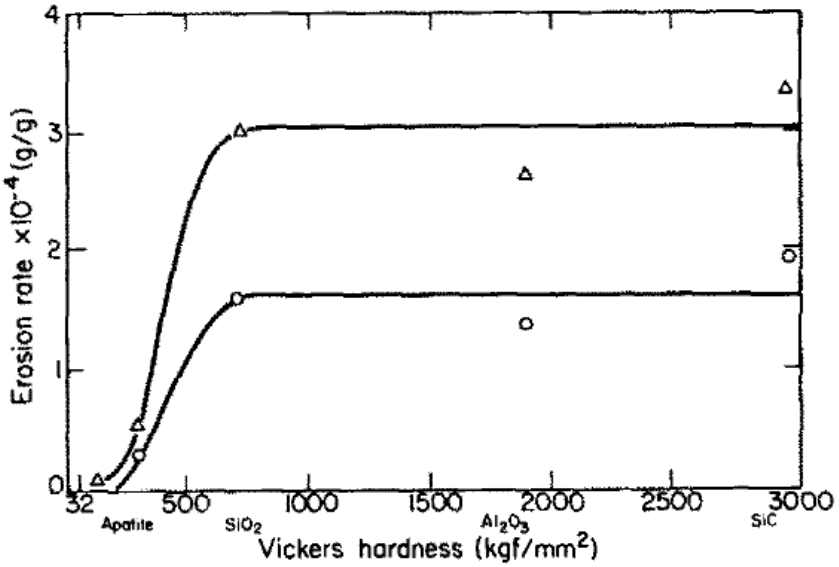

Figure 18: Erosion rates of AISI 1020 steel by the different abrasives: ∆ = 30°, o = 90° [26]

Suckling [30] investigated the high temperature erosive wear of boiler tube steel. He found that the effect of particle type on the wear rate was significant. The denser, harder SiC and $Si0_2$ particles caused greater erosion than the friable plant fly ash. The effect of particle size was found to be significant whereby the smaller SiC and $Si0_2$ particles with a diameter of between 63 - 106 μm cause up to 100% more wear than the larger 106 - 125 μm particle size range.

2.6. Temperature effects

Jianren and Shyam [21] studied the erosion characteristics of alumina ceramics at high temperatures. Upon examination, they noted that the eroded surfaces revealed that the erosion characteristics of alumina at elevated temperatures were significantly different from those at ambient temperature. They also noted that there was plastic deformation occurring on the eroded surfaces at shallow impingement angles and at high temperatures because the secondary glassy phase softens and so undergoes more plastic deformation upon external impacts [21]. The variation of erosion rate with temperature for five kinds of alumina's is shown in Figure 19. They also noted that for most alumina's, erosion rates are almost unaffected by the changes in temperature from ambient to 400°C.

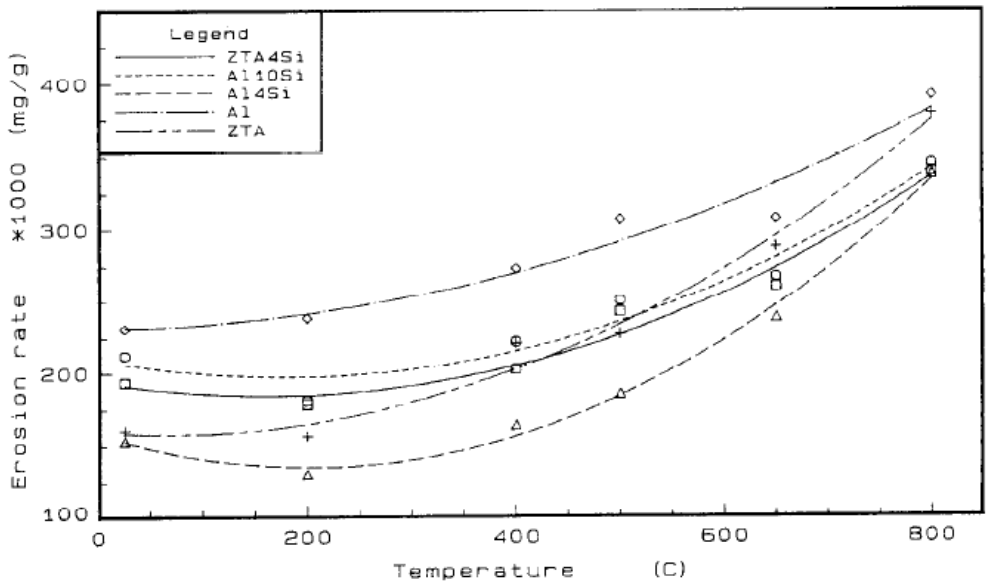

Figure 19: Variation of erosion rate as a function of temperature at normal impact (velocity, 50 m/s) [21]

Minghao et al [23] investigated the effect of temperature on solid particle impact erosion wear mechanism of 5 mol% Yttria Stabilized Zirconia (5YSZ) ceramics and observed that the erosion wear rate increases with the rising temperature. Figure 20 shows the curve for the solid particles impact volume erosion rate of 5YSZ ceramics vs. elevated temperature [23].

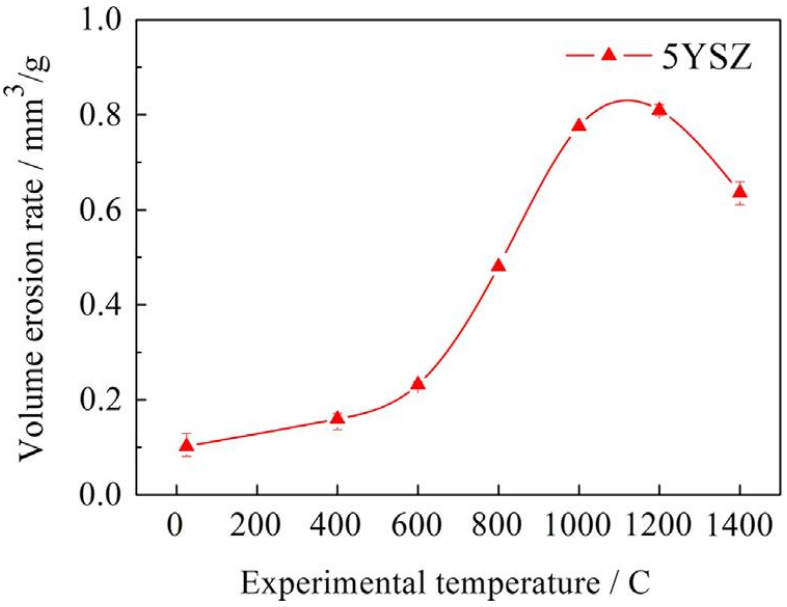

Figure 20: The effect of temperature on the volume erosion rates of 5YSZ ceramics [23]

Shida and Fujikawa [33] studied the particle erosion behaviour of typical boiler tube materials, including carbon steel, low alloy steels and austenitic steels, at elevated temperatures up to 650 ˚C

using irregularly shaped silica particles. They noted that the erosion rate varied significantly between materials, e.g. the Incoloy 800 alloy eroded the most and the 12Cr-1Mo-V steel eroded the least at every temperature used. Every material showed an increase in the erosion rate with temperature. Using their erosion rate data obtained at 20° for every material at every temperature with the tensile properties of the steels, they found that the yield strength of materials correlates reasonably well with the erosion rate.

Figure 21 shows that the erosion rate to increase with temperature was obtained for every steel [33]. Shida and Fujikawa concluded that the alloy-800 exhibited the greatest erosion rate at all temperatures while the 12Cr-lMo-V steel exhibited the smallest. The carbon steel, the 2.25Cr-1Mo steel and the 304-steel showed similar erosion rates [33].

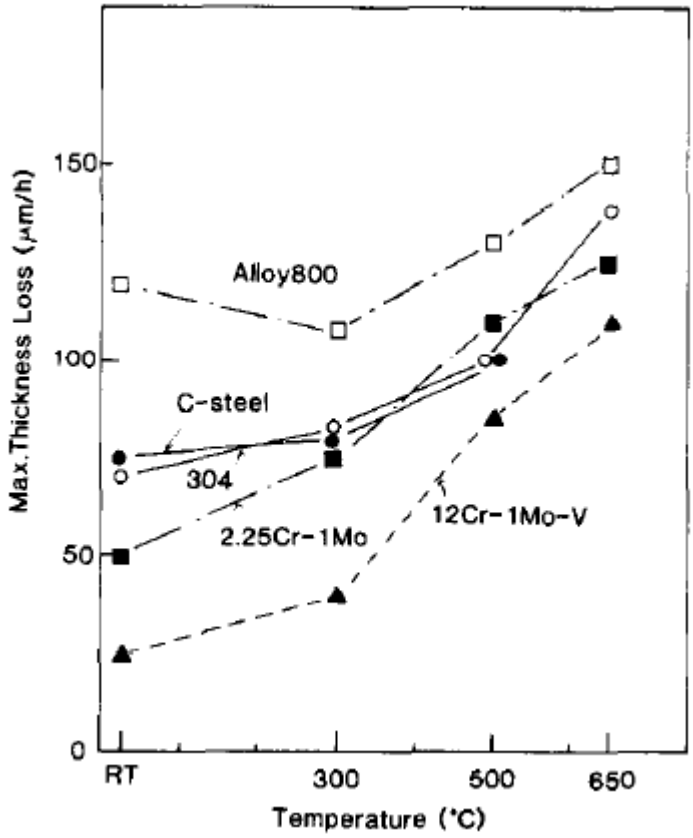

Figure 21: Effect of temperature on the erosion thickness loss rate of various steels, impingement angle 20°; velocity, 120 m/s; particle concentration, 120 g/mm^3 [33]

Tabakoff et al [25] also observed an increase in the erosion rate and a tendency for the velocity exponent to decrease with temperature using a 304 steel, a titanium alloy (Ti-6Al-4V) and a nickel-base superalloy (Inconel 718). The authors mention that the erosion rates of the Ti-GAl-4V and

Inconel 718 alloys increase abruptly as the specimen temperature approaches the annealing temperature of the materials.

2.7. Experimental methods of erosion

Erosion experiments were carried out using an air-jet erosion test rig with silica abrasive at impact velocity of 60 m/s for three impingement angles 30°, 45° and 90° [41]. The erosion specimens were machined and thoroughly cleaned using acetone solvent. Grit blasting was carried out with high air pressure, alumina grit (600 - 680 μm). The surface finish (Roughness (Ra)) achieved on the test specimens was Ra 5 to 6 μm. The standard blasting conditions are shown in Table 2.

Table 2: Grid blasting parameters [41]

Parameters	Description
Pressure	2.4 $\frac{Kg}{cm^2}$/ or 2.3536 bar
Grid and size	Alumina 24 mesh
Blasting time (s)	20 - 40

During these experiments, the erosion experiments were carried out as per the solid erosion particle testing standard [44]. The erosion test parameters are shown in Table 3.

Table 3: Test parameters for dry erosion test [44]

Erodent material	Silica
Particle size (μm)	120 - 150
Particle shape	Angular
Particle velocity (m/s)	60
Feed rate (g/min)	1.2132
Impact angles (°)	30, 45, 60
Test duration (min)	10
Nozzle distance (mm)	10

According to Polym [42], the design of experiments approach utilizing Taguchi's orthogonal arrays was applied to test the specimens on a compressed air jet type erosion test rig. Before the erosive wear experiments, all specimens were cleaned with acetone. Great care was taken to ensure a

clean surface before and after wear experiments. Sand and dust particles were cleaned after the erosion test with air blasting and then balanced. The weight of the samples before and after the erosion process was measured by using precision digital electronic balance erosion rates (E_R) were calculated from the differences of weight (W) loss by considering unit of time as follows [42].

$$E_R = \frac{W_{before} - W_{after}}{Time} \quad (3)$$

Suckling [30] established the erosion rig conditions shown in Table 4.

Table 4: Established erosion rig conditions [30]

Working pressure	< atmos. i.e. 90 kPa
Working temperature	ranges from 20 to 600 °C (speciment)
Erodent velocity	10 m/s to 40 m/s
Erodent mass flux	5 to 20% of the gas flow by mass
Erodent type	plant fly ash
Erodent particle size	Ranging from 20 to 150 µm
Operating time/run	30 minutes initially, with scope for modification

Suckling used low carbon, high strength low alloy steel plate material during erosion experiments. Specimen dimensions were 20 mm wide, 6 mm thick and 35 mm long. The abrasives that were used are ash, SiC and SiO_2. The abrasives were sieved prior to testing within the size ranges required which were 63 - 106 μm (220 grit) and 106 -125 μm (120 grit) using a Fritsch vibratory sieving device and King test stainless steel sieves. The sieves were cleaned between experiments by using a soft brush to remove particles wedged in the sieve apertures. The specimens were ground with a diamond wheel to Ra = 0.5 μm and then further polished using a 600-grit abrasive paper to Ra = 0.05 μm prior to an erosion test. During initial room temperature erosion work, ground specimens were used to obtain mass loss data [30].

Wellman [39] studied the solid particle erosion of ceramics using three different abrasives (SiO_2, Al_2O_3 and SiC). The samples were all eroded under standard experimental conditions as summarised in Table 5.

Table 5: Operating conditions [39]

Erodent	Al_2o_3 120 grit SiC 120 grit SiO_2 100, 120, 140 grit
Impact angle (°)	30, 45, 60, 90
Velocity (m/s)	30, 40, 50
Working distance (cm)	3
Operating temperature	Room temperature
Particle feed rate (g/s)	0.446

According to Wellman [39], the mass loss per gram of abrasive is converted to volume loss by dividing by the density of the steel.

$$E = m'/\rho \quad (4)$$

Where: m' = constant from the linear regression of the cumulative material mass loss versus cumulative abrasive data and ρ = density of the specimen.

The steady state erosion rates were calculated from the cumulative mass losses of eight consecutive erosion experiments using linear regression and reported as mass loss per gram of abrasive. In order to ascertain the reproducibility of the experiments duplicate experiments were performed on some of the samples. Between each test, the samples were washed in alcohol in an ultrasonic bath for 5 s. They were then dried thoroughly and weighed on an analytical balance, which was accurate to 0.01 mg [39].

During all the experiments that were conducted the samples were placed at a distance of 30 mm from the outlet of the tube and an area of 53 mm^2 was exposed to the particle stream [39]. During erosion testing a cover was placed over the target in order to ensure that a standard area (53 mm^2) was exposed to the abrasive stream [39].

Okonkwo et al [43] studied the erosion behaviour of API X100 pipeline steel at various impact angles and particle speeds. The erosion test rig was according to the ASTM standard [44]. Prior to each test, the steel specimens were ground using 240, 320 and 600 grit silicon carbide papers. Alumina particles were used as the abrasive at ambient temperature for the experiments. The feed rate of the solid particles was determined by measuring the weight of the abrasive particles coming through the nozzle per unit time. The particle velocity was determined as a function of pressure using the

double disc method. The test parameters used for the erosion studies on API X100 steel are shown in Table 6.

Table 6: Test parameters used for the erosion of API X100 steel [43]

Test temperature	**Room temperature**
Test gas	Dry compressed air
Particle speed (m/s)	20, 40, 60, 80
Nozzle diameter (mm)	1.5
Test duration (s)	10, 300, 600
Angle of incidence (°)	30, 90
Standoff distance of test specimen (mm)	10

In this erosion study of pipeline steels [43], the stand-off distance between the steel specimen and nozzle was kept constant at 10 mm to enhance uniform distribution of the aluminium oxide solid particle stream. The API X100 steel specimen is mounted on the specimen holder facing the nozzle as displayed in Figure 1. The dry erosion experiments were run at 10, 300, and 600 s for each of the tested impact angle and particle speeds. Each test was repeated three times for reproducibility. Specimens were weighed before and after each test using a digital balance with accuracy of 0.00001 g to calculate the difference in weight loss.

The following test procedure was extracted from ASTM G76 - 07 [44]:

- Establish and measure the particle velocity and particle flow specified. Adjust equipment controls to obtain proper velocity and flow conditions before inserting test specimens. Particle flow rate values are determined by collecting (particles may be collected by directing the flow from the nozzle into a large vented container. Care must be taken to avoid causing any significant back pressure on the nozzle as this will disturb the system flow conditions) and subsequently weighing the abrasive exiting from the nozzle for a measured time period,
- Clean the specimen surface carefully,
- Mount the specimen in proper location and orientation in the apparatus. Subject the specimen to particle impingement for a selected time interval. Remove the specimen, clean carefully (important considerations in cleaning include surface oils or greases, surface rust or corrosion, adhering abrasive particles, etc.), re-weigh and calculate the mass loss,
- The abrasive particle velocity shall be 30 ± 2 m/s, measured at the specimen location. At this velocity the gas flow rate will be approximately 8 L/min and the system pressure will be approximately 140 kPa although the pressure will depend on the specific system design,

- The test time shall be 10 min to achieve steady state conditions. Longer times are permissible so long as the final erosion crater is no deeper than 1 mm,
- The angle between the nozzle axis and the specimen surface shall be 90 ± 2°,
- The test temperature shall be the normal ambient value (typically between 18°C to 28°C),
- The particle feed rate shall be 2.0 ± 0.5 g/min,
- The distance from specimen surface to nozzle end shall be 10 ± 1 mm,
- The erosion value (mm^3/g) is calculated by dividing erosion rate (mg/min) by the abrasive flow rate (g/min) and then dividing by the specimen density (g/cm^3).

2.8. Scanning electron microscopy

Studies on solid particle erosion of ceramics was performed by Wellman [39]. During SEM analysis of the eroded surfaces of the brittle materials, Wellman observed pores on the impacted surfaces. The micrograph shown on the left of Figure 22 is of a single impact on a semi-exposed pore of M97F material, extensive cracking occurred in the material above the unexposed section of the pore and one of the surface cracks had extended away from the pore. Other cracks were stopped from further propagation by intersecting with the exposed region of the pore which effectively blunts the crack. The micrograph shown on the right of Figure 22 illustrates at a lower magnification at the same location the way in which the other crack has been stopped by intersecting with another pore.

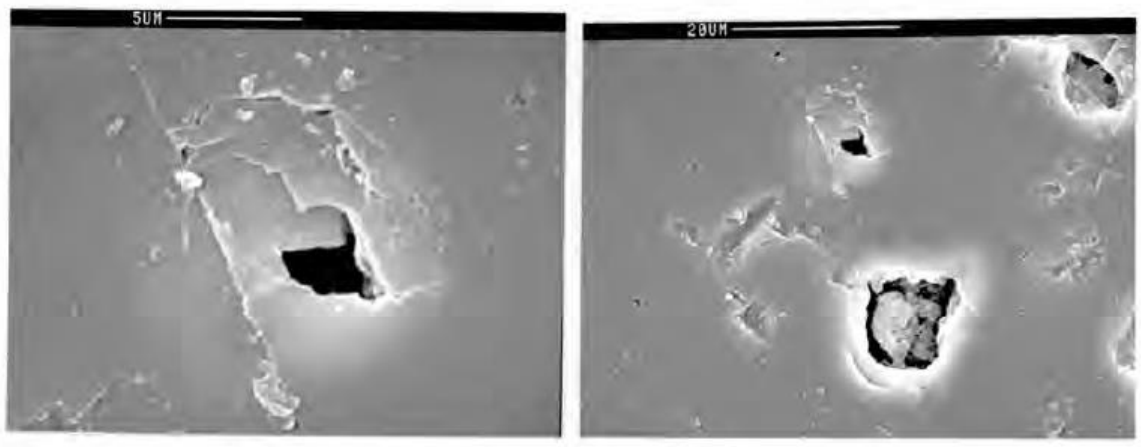

Figure 22: SEM micrograph of a single impact site on a sub-surface pore [39]

Feng [36] performed SEM analysis on sintered alumina material and observed the extent of porosity on the polished cross section of this material as shown in Figure 23. The pores in alumina material are sites where cracks can initiate during erosion and damage occurs without any crack initiation. From a single impact site, damaged areas were characterised by relatively deep pits formed primarily through plastic deformation and intergranular cracking without any evidence of radial or

lateral cracking around this area. This is due to the weakness of the grain boundaries of this material. It was concluded that the steady state eroded surface if alumina material by different abrasives were very similar, differing only in the ratio of plastic deformation to fracture.

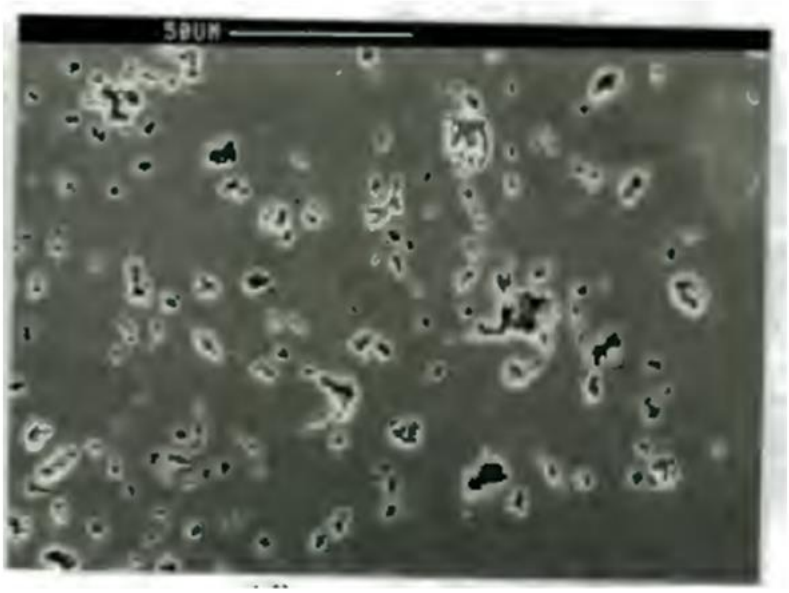

Figure 23: Micrograph of sintered alumina material showing porosity [36]

Malik et al [47] evaluated the effect of hardness on erosion characteristics of aluminium and steels. Eroded stainless steel 310S SEM results at impact angles of 15° and 90° are shown in Figure 24. The severe material degradation is caused by extrusion/ploughing action. Moreover, the indications of material removal such as deformation scratches are also shown. The damage at a 90° impact angle is much less severe with no deformation scratches. In this case, crates and pits are visible indicating that most of the kinetic energy of incident particles is dissipated in deforming/displacing the material rather than actual material removal.

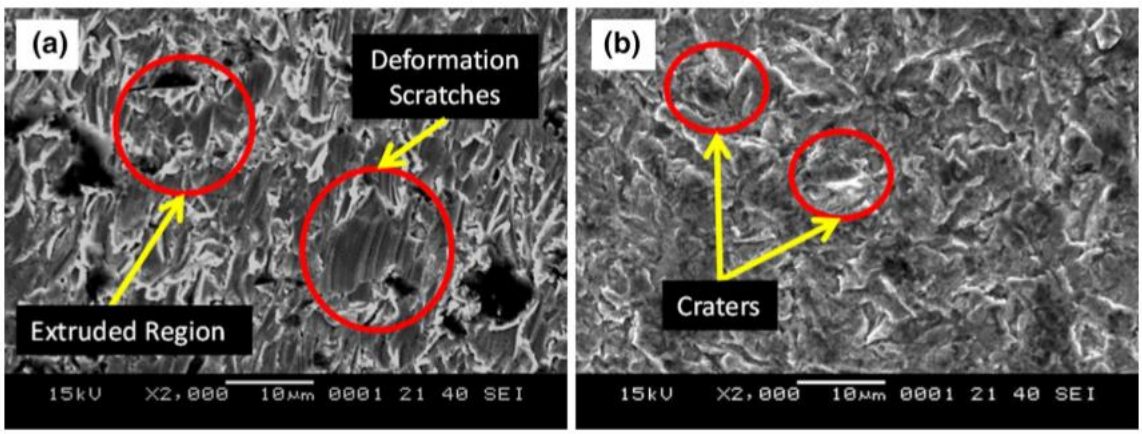

Figure 24: SS 310S eroded at impact angles of 15° (left) and 90° (right) [47]

The eroded surfaces of carbon steel 1020 reported by Malik et al [47] are shown in Figure 25. It was noted that at an impact angle of 15° there was higher wear damage compared to a 90° impact angle. The deformation scratches and lip formation due to plastic deformation by extrusion/ploughing action are shown. At a 90° impact angle, the ductile erosion behaviour in carbon steel AISI 1020 is characterized by dimples, pits, and crater morphologies.

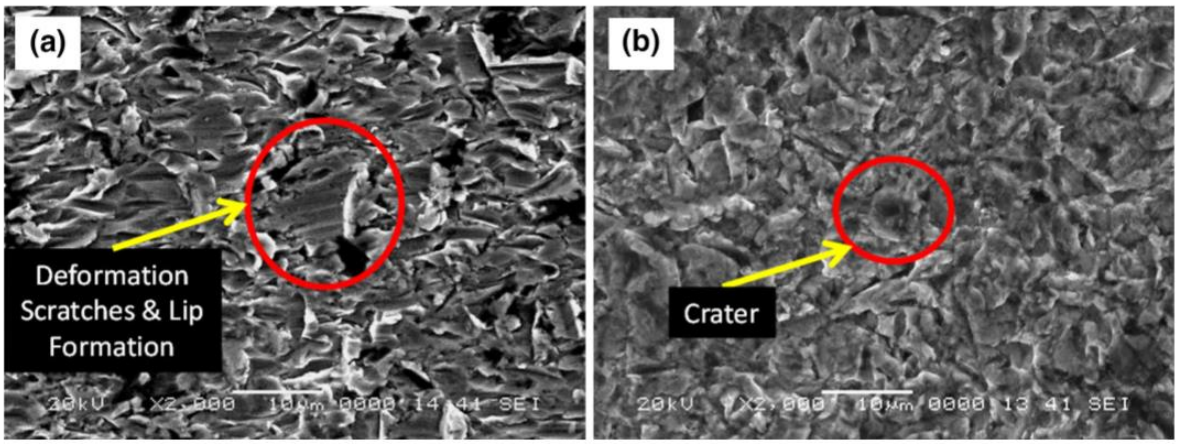

Figure 25: Carbon steel AISI 1020 eroded at impact angles of 15° (left) and 90° (right) [47]

The erosion at room temperature of carbon steel material is due to cutting wear and plastic deformation as mentioned by Mbabazi et al [4]. They observed that cutting wear occurred at low impact angles and deformation wear occurred at high impact angles.

Solid particle erosion experiments of different metallic materials such as aluminium, mild steel and stainless steel was performed by Juan et al [8]. They observed during SEM analysis of the eroded surfaces that the worn surfaces had many wear mechanisms such as lip formation, platelets, micro-cracking, micro-ploughing and small craters of indentation. On the mild steel material at a 30° impact angle, wear debris were observed inside craters, at a 90° impact angle, pitting action and irregular indentations was observed. For stainless steel 304 material at an impact angle of 30°, ploughing and pitting action was noted while at an impact angle of 90°, embedded abrasive particles and pitting was observed.

SEM analysis performed by Morrison et al [46] on stainless steel 304 material showed similar morphologies for low and high impact angles which were observed in ductile materials when subjected to sharp particle impacts.

Chapter 3: Research method

A detailed literature review was performed to determine and understand the variables which affect the erosion of materials. The focus of the research is given to the cold areas in power stations (examples include the PF and burner locations in a power plant). From the literature review, it was noted that there is no significant change in the erosion rate up to 400°C. Therefore, an ambient temperature experimental rig was used to perform solid particle erosion experiments at the selected impact angles (30°, 60° and 90°) to determine the erosive volume wear rate (erosion value) of each material. Five wear protection materials (ductile, brittle and semi-ductile) was pre-selected for the experiments.

QEMSCAN analysis was performed to determine and select which commercially available abrasive in SA has similar characteristics to fly ash and PF found at SA power plants. The selected abrasive was used to perform all experiments.

Erosion testing was done under controlled, reliable and repeatable conditions. Thus, a test methodology was employed to produces reliable results. A literature review was performed to determine which variables influence erosion. Using the literature review, a matrix (Table 7) was developed to highlight the variables that will be controlled and monitored in each test for the current erosion experiments.

SEM was used to analyse each material after it is exposed to erosive wear experiments at impact angles of 30°, 60° and 90°. SEM analysis was used to determine how the different materials at different impact angles was eroded when exposed to solid particle erosion testing. The mechanism of material removal for each type of material (ductile, brittle and semi-ductile) was observed and compared to published literature.

The erosion rate experimental results that was obtained by Mbabazi et al [4] on carbon steel material showed a good correlation with experimental results obtained by other authors in the literature review when comparing the erosion rate trend from a 30° to 90° impact angle. The results from the current experiments was compared to the results obtained in published literature by Mbabazi et al [4] on carbon steel material where fly ash from three different power stations was used as the abrasive material. If a correlation, such as a trend of the erosion rate from a 30° to 90° impact angle exists between the experimental results when compared to those in published literature by Mbabazi et al [4], then there will be a good level of confidence and repeatability. Relative erosion values were determined on the pre-selected materials thereafter.

With regards to uncertainty in erosion experiments, different methods of measuring volume loss were considered and the environment for testing was controlled, such as nozzle distance to the

samples, the abrasive flow rates and loading of particles for every test. These methods assisted with regards to the reproducibility and repeatability of erosion experiments performed in the laboratory.

The volume loss of the sample material divided by the total mass of abrasive particles that impacted the specimen is equal to the erosion value. The volume loss for each sample was determined and the erosion value was calculated.

Criteria for validation

- The abrasive and its particle size and shape for the current experiments will be selected by evaluating the QEMSCAN results of power plant fly ash and PF samples from SA and commercially available Al_2O_3 and SiO_2 abrasives in SA. The commercially available abrasive which closely matches the SA power plant sample properties will be selected as the abrasive for the current experiments.
- The current experimental results for carbon steel material will be validated against erosion results from published literature by Mbabazi et al [4] who used fly ash from three SA power plants. Thereafter relative erosion rates are determined on the other pre-selected materials.

Table 7: Matrix showing the current erosion experiments parameters

Material	Behaviour type of material	Particle velocity (m/s)	Angle of impact (°)	Particle size of abrasive (μm)	No. of experiments per impact angle	Erosion test time per sample (minutes)
Carbon steel	Ductile	30 ± 2	30, 60 and 90	75 - 200	5	10
VRN 400	Ductile	30 ± 2	30, 60 and 90	75 - 200	3	10
92% Alumina ceramic tiles	Brittle	30 ± 2	30, 60 and 90	75 - 200	3	10
96% Alumina ceramic tiles	Brittle	30 ± 2	30, 60 and 90	75 - 200	3	10
Stainless steel (grade 316L)	Semi-ductile	30 ± 2	30, 60 and 90	75 - 200	3	10

Chapter 4: Materials

4.1. Selection of the specimen materials

There are many applications that require wear protection at a coal fired power plant. The materials that were selected for the current erosion experiments are as shown in Table 8. A selection of ductile, brittle and semi-ductile materials was chosen for the current experiments. These materials were selected based on current SA power plant experience, the material availability in SA, verbal communication with material experts from SA power plants and wear protection that was recommended by SA companies that tested these materials in a lab.

The material properties of the pre-selected wear protection materials are shown in Appendix A. The specimen material dimensions are shown in Table 8.

Table 8: Specimen material dimensions

Material	Specimen dimensions (mm)
Carbon steel (ductile)	30x20x10
VRN 400 (ductile)	30x20x10
Stainless steel (grade 316L) (semi-ductile)	30x20x10
92% Alumina ceramic tile (brittle)	48x25x5
96% Alumina ceramic tile (brittle)	48x25x5

4.2. Selection of the abrasive material

QEMSCAN equipment was used to determine the PF, fly ash, SiO_2 and Al_2O_3 abrasive particle size and shape together with its elemental composition. PF and fly ash from coal fired power station A, power station B, power station C and power station D and commercially available SiO_2 and Al_2O_3 underwent QEMSCAN analysis.

The process for the selection of the most suitable abrasive is shown in Figure 26. Fly ash from the SA power stations wasn't selected as an abrasive during these experiments due to the task of cleaning up the rig and the environment around it. PF from the SA power stations were not selected as the abrasive in these experiments due to the possibility of an explosion risk.

Accelerated erosion testing was achieved by using the commercially available abrasive which had the highest abrasive index as determined from the QEMSCAN analysis.

Therefore, the commercially available abrasive with the closest match to shape, size and mineralogy to the PF and fly ash from the SA power stations was selected for the experiments from the QEMSCAN analysis.

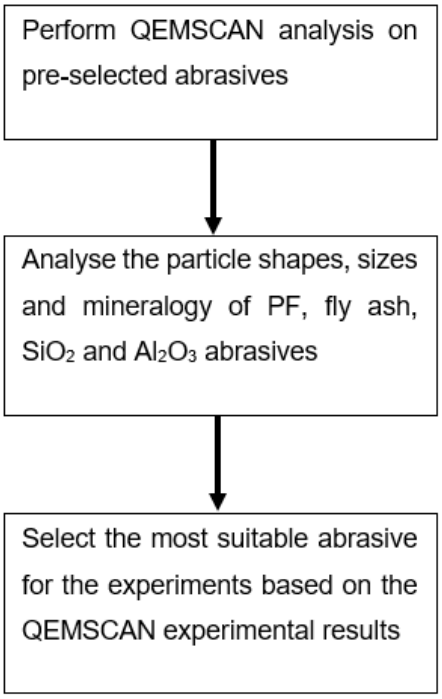

Figure 26: Process for selecting the abrasive

Chapter 5: Experimental setup and procedure

5.1. Experimental rig setup

The erosion rig used during this experiment is shown from Figure 27 to Figure 30. Figure 27 shows the erosion rig with the motor and abrasive feeder at the top right of the image and the variable speed controller is shown at the top left of the image.

Figure 27: Erosion rig setup

This rig was designed and built by Thermaspray (Pty Ltd) in accordance to the ASTM Standard Test Method for Conducting Erosion Experiments by Solid Particle Impingement Using Gas Jets[44]. The nozzle to specimen distance was measured for every test and the specimen to nozzle distance was adjusted accordingly using the height adjustable mechanism shown in Figure 29. The abrasive particle flow rate values was determined by collecting and

subsequently weighing the abrasive exiting from the nozzle for a measured time period and experiments was only conducted once the flow rate was within specification [44]. The impact angle was checked against the sample holder markings (Figure 30) before each test was performed. Erosion of the nozzle during experiments was monitored to ensure it did not exceed 10% increase in the initial diameter at the start of the experiments.

Figure 28 shows the pressure gauge that was used to control the compressed air supply pressure for the experiments.

Figure 28: Pressure gauge

Figure 29 shows the components and the setup of the solid particle erosion rig. The nozzle is attached to the accelerator tube which has and height adjustable mechanism to cater for the nozzle to sample holder distance during the experiment. The compressed air and abrasive supply lines are also shown.

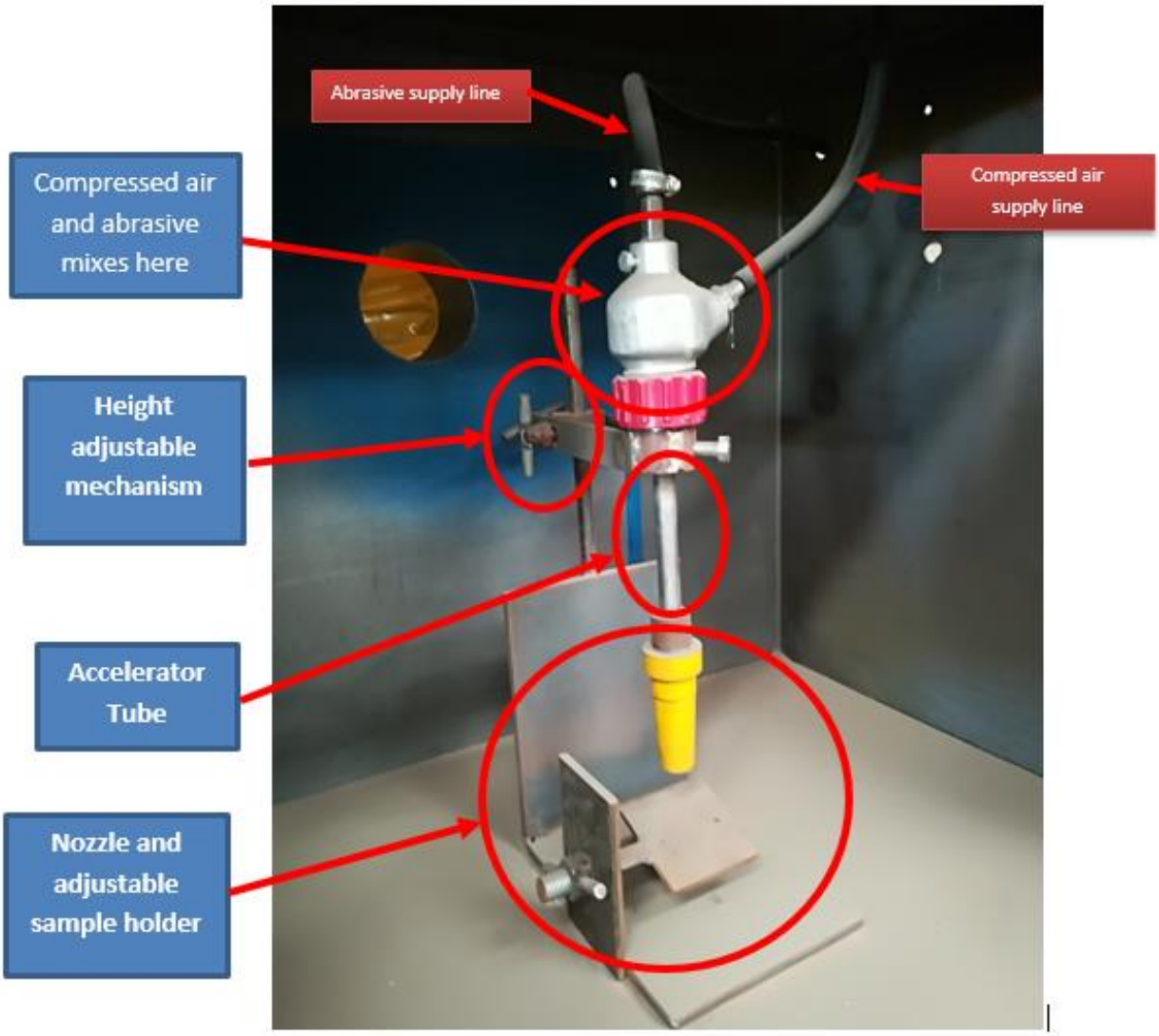

Figure 29: Erosion rig experiment setup

Figure 30 shows the adjustable sample holder mechanism which catered for the various impact angles used in this experiment.

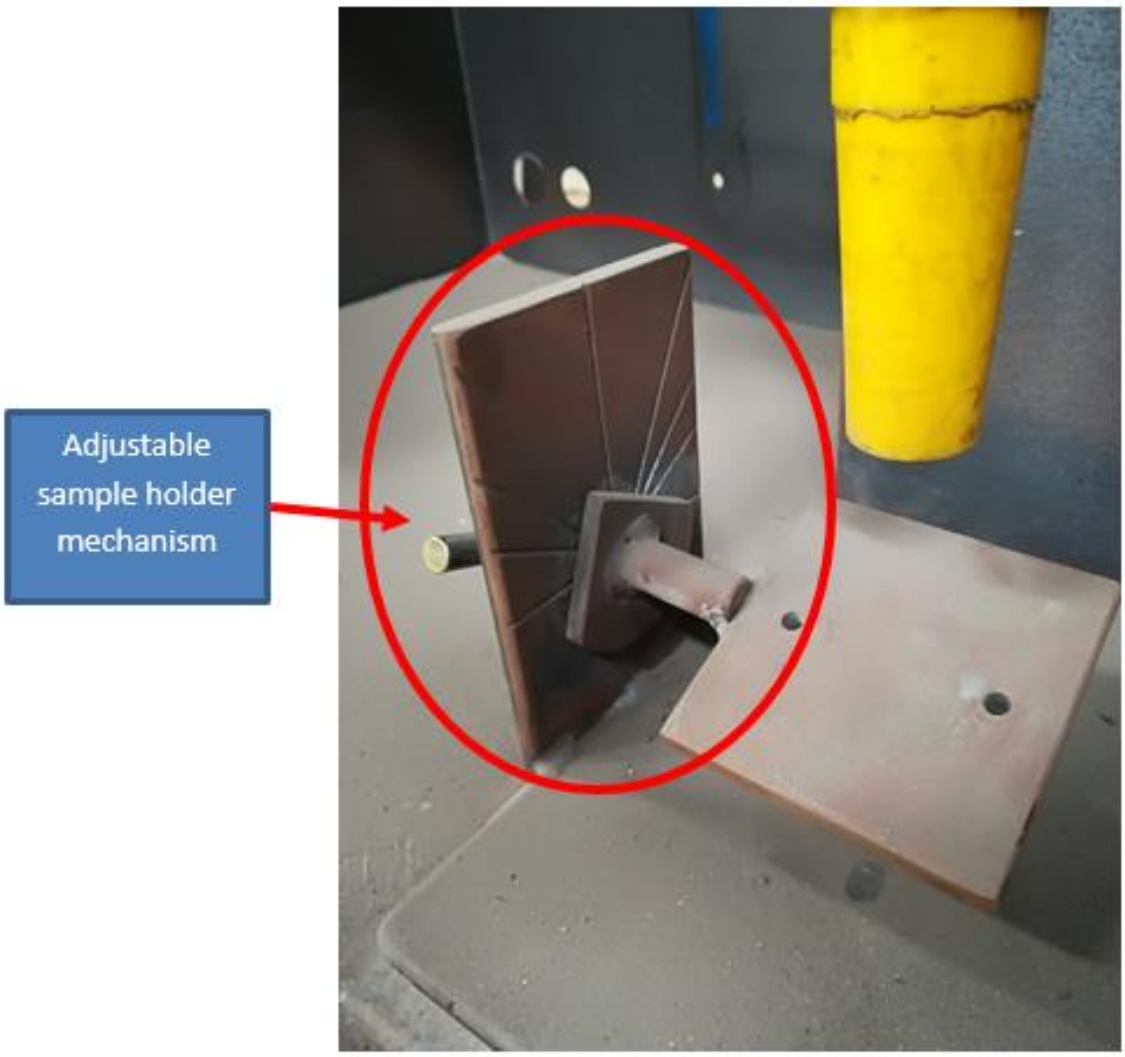

Figure 30: Sample holder setup

The actual particle velocity was not measured due to the measuring equipment not being available. The particle velocity could not be measured because the erosion rig could not be modified.

5.2. Experimental procedure

The following test methodology was used for the solid particle erosion experiments [44]

- The specimens were thoroughly cleaned using acetone solvent.
- Abrasive particles were cleaned off from the specimen after each erosion experiment with air blasting and acetone and then balanced carefully. The weight of the specimens before and after the erosion process was measured using a digital electronic balance with an uncertainty of ± 0.01 mg.
- The distance from specimen surface to nozzle end was maintained at 10 ± 1 mm.
- The system pressure was maintained at approximately 140 kPa.
- The abrasive particle feed rate was determined and maintained at 2 ± 0.5 g/min.
- The following parameters were fixed, Al_2O_3 abrasive, velocity of the particles with irregular shape and ambient temperature.
- In order to ascertain the reproducibility of the experiment - each test was repeated at least three times for reproducibility.
- The test time was 10 minutes in-order to achieve steady state conditions.
- The standard system was run under pre-described parameters which resulted in a velocity of 30 ± 2 m/s.
- The erosion rate is calculated from the differences of weight loss by considering unit of time as follows;

$$\mathrm{E_R} = \frac{\mathrm{W_{before}} - \mathrm{W_{after}}}{\mathrm{Time}} \tag{5}$$

- The erosion value $(\mathrm{mm^3/g})$ is calculated by dividing erosion rate $(\mathrm{mg/min})$ by the abrasive flow rate $(\mathrm{g/min})$ and then dividing by the specimen density $(\mathrm{g/cm^3})$.

NOTE: The erosion value discussed in this report is based on volume as per the ASTM standard [44] while in the literature review chapter of this report it is sometimes referred to as the erosion rate by other authors. The erosion value incorporates the erosion rate, the density of each material and the flow rate of the abrasive particles experienced during the current experiments.

Chapter 6: Results and discussion

6.1. Quantitative evaluation of materials by scanning electron microscopy

The fly ash and PF samples from SA power plants together with the commercially available abrasives underwent QEMSCAN analysis. PF samples from power station A, B, C and D and fly ash samples from power station B, C and D was collected and submitted for QEMSCAN analysis. Fly ash from power station A was not readily available at the time of analysis.

The purpose of the QEMSCAN analysis was to determine the particle sizes and shapes of the PF and fly ash samples from the power stations mentioned above. The PF and fly ash mineral identification standard was used to characterise the mineral/phases in the PF and fly ash samples that were analysed. The detailed QEMSCAN analysis results are shown in Appendix B.

The QEMSCAN results of the PF and fly ash samples are as follows;

- QEMSCAN based abrasive index for Power station D, A, B and C are 783, 366, 289 and 222 mg/Fe respectively. Power station D contained the highest proportion of abrasive sandstone when compared to Power station A, B and C,
- Power station B fly ash contained a higher proportion of quartz when compared to power station D,
- The shape factor distribution of fly ash and PF: the higher proportion of cenospheres in fly ash increases the proportion of particles with a shape factor <1.3 relative to PF. The proportion of elongated minerals is relatively low and there is no distinct difference between the respective fly ash and PF samples.

Based on the above QEMSCAN results on the PF and fly ash samples, it was concluded that power station D has the mineralogical properties which is likely to marginally increase wear rate relative to power station A, B and C.

Commercially available Al_2O_3 and SiO_2 abrasive underwent a QEMSCAN analysis to determine the shape and size of these abrasive. These results will be used to determine which commercially available abrasive closely matches power station A - D PF samples and power station B - D fly ash sample size and shape.

The following was noted from the QEMSCAN analysis of the Al_2O_3 and SiO_2 abrasive samples;

- The SiO_2 abrasive is predominately spherical sand (quartz), whereas the Al_2O_3 abrasive sample is a mixture of angular aluminium oxide, iron titanium oxide, iron silicate, clay/garnet and quartz,
- The average size of the SiO_2 and Al_2O_3 abrasive is 573 and 85 μm respectively,
- The Al_2O_3 abrasive sample had a higher proportion of angular particles compared to the SiO_2 abrasive sample. Al_2O_3 is finer and marginally more angular than the SiO_2 abrasive sample.

Al_2O_3 abrasive has an average predicted Mohr hardness of 8.3, compared to 7 for the SiO_2 particles. The predicted abrasive index is shown in Table 9.

Table 9: Predicted abrasive index (mg/Fe)

	Power Station D (fly ash)	**Power Station C (fly ash)**	**Power Station B (fly ash)**	**Power Station A - D (PF samples)**	**Al_2O_3**	**SiO_2**
Predicted abrasive index (mg/Fe)	604	313	604	222 - 783	3650	2800

Al_2O_3 was found to be finer and marginally more angular than the SiO_2 particles. The literature review suggests that angular particles are more abrasive than spherical particles. Al_2O_3 abrasive was selected for the experiments. This selection was based on the following:

- high hardness and associated higher abrasive index,
- the average particles size is marginally coarser than fly ash,
- the degree of angularity.

6.2. Determining the material specimen density

Density is the mass of a substance per unit of volume as follows:

$$\rho = \frac{m}{V} \tag{6}$$

The mass of the samples was weighed using an electronic balance. A precise graduated cylinder (1 ml increments) was filled with water for each experiment and the volume of this water was recorded. The sample for each experiment was then placed into the graduated cylinder and the final volume (water and sample) was recorded. The volume of the sample was calculated by using the difference between the final and the initial volume of water for

each experiment. The density was then calculated by dividing the mass of the sample by the volume of the sample for each experiment.

The results of the pre-selected material density experiments are shown in Table 10. Precautions were taken to check the reading at the bottom of the meniscus. The marked scale on the graduated cylinder was 1 ml, therefore the uncertainty in the measurement was taken as half the quantity between markings on the cylinder. The experimental error in measuring the volume during this experiment was taken as ± 0,5 ml and the error in the mass measurement of the specimen was ± 0,01 mg. The experimental error measurement of the mass (± 0,01 mg) does not have a significant bearing on the calculation of the erosion value, therefore it was omitted.

Table 10: Material density results

Materials	Initial Volume of water without sample (ml)	Final Volume of water with sample (ml)	Volume of sample material (ml)	Mass of sample (g)	Density of material (ρ) (g/cm^3)	Experimental error (%)	Experimental error (g/cm^3)	Density of material (ρ) with Experimental error (g/cm^3)
Carbon steel sample #1	23,5	29	5,5	45,833	8,333	9,091	0,758	8,333 ± 0,758
Carbon steel sample #2	40	45,5	5,5	45,638	8,298	9,091	0,754	8,298 ± 0,754
96% Alumina sample #1	77	84	7	27,801	4,114	7,143	0,294	4,114 ± 0,294
96% Alumina sample #2	110	117	7	28,321	4,046	7,143	0,289	4,046 ± 0,289
92% Alumina sample #1	107	114	7	25,077	3,583	7,143	0,256	3,583 ± 0,256
92% Alumina sample #2	72	79	7	25,880	3,697	7,143	0,264	3,697 ± 0,264
VRN 400 sample #1	33	39	6	45,754	7,626	8,333	0,635	7,626 ± 0,635
VRN 400 sample #2	32	38	6	45,801	7,634	8,333	0,636	7,634 ± 0,636
316L stainless steel sample #1	42	48	6	47,408	7,901	8,333	0,658	7,901 ± 0,658
316L stainless steel sample #2	43,5	49,5	6	47,347	7,891	8,333	0,658	7,891 ± 0,658

6.3. Solid particle erosion test results

All pre-selected materials were tested under the same conditions. The carbon steel erosion rate (mg/g) results are shown in Table 11. The experimental error measurement of the mass (± 0,01 mg) does not have a significant bearing on the calculation of the erosion rate or erosion value, therefore it was omitted. The experimental error in measuring the volume during the material density experiments was taken as ± 0,5 ml and was used in the calculations that were performed in this section of the report.

Table 11: Erosion rate of carbon steel material

Impact angle (°)	Weight before (g)	Weight after (g)	Erosion rate (mg/min)	Abrasive flow rate (g/min)	Erosion rate (mg/g)
30	46,2011	45,8601	34,1000	1,9248	17,7161
	46,4522	46,1319	32,0300	1,9248	16,6407
	48,3121	47,9671	34,5000	2,0178	17,0978
	47,3538	47,0112	34,2600	2,0523	16,6935
	46,5623	46,2086	35,3700	2,0523	17,2343
60	45,9946	45,906	8,8600	1,6420	5,3959
	45,4586	45,3722	8,6400	1,6420	5,2619
	45,5546	45,4692	8,5400	1,6420	5,2010
	45,6761	45,5689	10,7200	2,0523	5,2234
	45,8761	45,7682	10,7900	2,0523	5,2575
90	45,9012	45,8434	5,7800	1,6420	3,5201
	45,2375	45,1784	5,9100	1,6420	3,5993
	45,4202	45,3507	6,9500	2,0178	3,4444
	48,6351	48,5631	7,2000	2,0523	3,5083
	48,9861	48,9152	7,0900	2,0523	3,4547

The results from Table 11 are plotted in Figure 31. The erosion rate trend from a 30° to 90° impact angle for carbon steel material is shown in Figure 31. The trend of the erosion rates for carbon steel material from this experiment will be compared to the trends observed in published literature [2.3]. The literature review from this report shows that there is a good correlation of results from all authors with regards to the trend of the carbon steel material erosion rate from a 30° to 90° impact angle. The results shown in Figure 32 are from experiments that was performed by Mbabazi et al [4] on carbon steel material using fly ash

from power station B, C and D. Fly ash from power station A - D together with commercially available abrasives was analysed via QEMSCAN in this report and the most suitable commercially available abrasive that closely matched the fly ash properties was selected for the experiments. Therefore the trend of the carbon steel material erosion rate results obtained in the current experiments (Figure 31) will serve as a good comparison to the results obtained by Mbabazi et al [4] as per the research method described in this report.

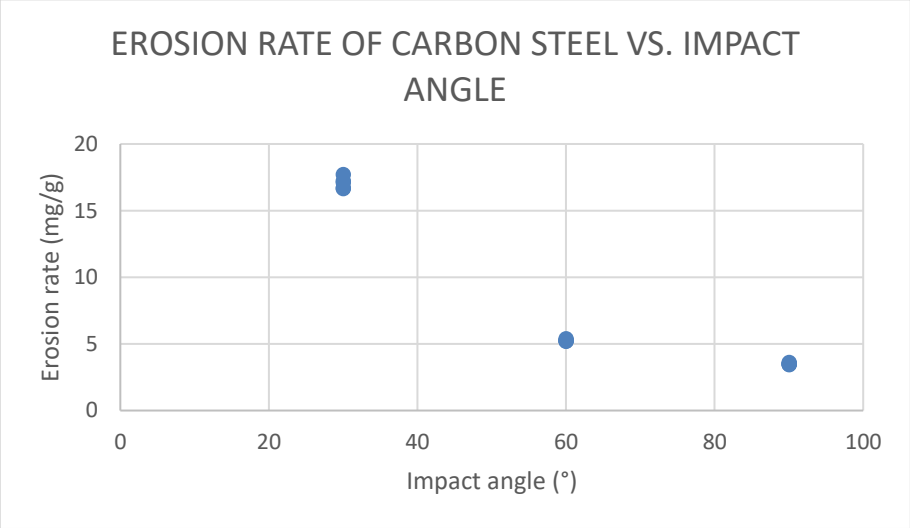

Figure 31: Erosion rate of carbon steel vs. impact angle

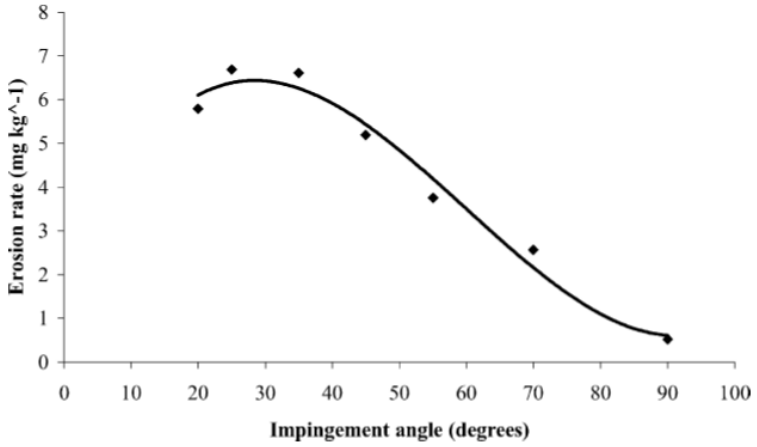

Figure 32: Mild steel erosion rate at various ash particle impingement angles with ash from Matimba: impact velocity 24.77m/s [4]

There is a good correlation between the carbon steel erosion rate trend from a 30° to 90° impact angle as shown in Figure 31 (current experimental results) vs the carbon steel erosion rate trend shown in Figure 32 which was obtained by Mbabazi et al [4]. Since there is a good correlation between the carbon steel erosion results from this experiment when compared to

literature, therefore relative erosion evaluation and ranking was performed on the rest of the pre-selected materials.

The erosion value (mm^3/g) was calculated by dividing erosion rate ($\mathrm{mg/min}$) by the abrasive flow rate ($\mathrm{g/min}$) and then dividing by the specimen density ($\mathrm{g/cm}^3$). The erosion values (mm^3/g) of each pre-selected material were determined at impact angles of 30°, 60° and 90° as shown in Table 12. The detailed erosion test results are shown in Appendix C.

All samples were subjected to one constant particle velocity based on the erosion rig settings. The aim was to determine the relative erosion rate of the pre-selected materials. However, since the rig could not be used to measure more than one abrasive particle velocity, one particle velocity was sufficient to achieve the aim.

The results from the current experiments was compared to the results obtained by Mbabazi et al [4] for carbon steel material. The erosion rate trend from a 30° to 90° impact angle for the current experiments was similar to the results obtained by Mbabazi et al [4]. The current experimental results from Figure 31 show that the peak erosion rate occurs at a 30° impact angle and the experimental results reported by Mbabazi et al [4] in Figure 32 show that the peak erosion rate for carbon steel material occurs at an impact angle of 30°.

Table 12: Erosion value of the pre-selected materials

	Erosion value ($\mathbf{mm^3/g}$)				
Impact angle (°)	**Carbon steel**	**VRN 400**	**316L stainless steel**	**96% Alumina**	**92% Alumina**
30	2,134 ± 0,194	0,485 ± 0,040	0,4596 ± 0,038	0,475 ± 0,034	0,632 ± 0,045
30	2,005 ± 0,182	0,467 ± 0,039	0,4709 ± 0,039	0,469 ± 0,034	0,644 ± 0,046
30	2,06 ± 0,187	0,484 ± 0,040	0,462 ± 0,038	0,489 ± 0,035	0,64 ± 0,046
30	2,011 ± 0,183				
30	2,076 ± 0,189				
60	0,65 ± 0,059	0,428 ± 0,036	0,4969 ± 0,041	0,608 ± 0,043	0,729 ± 0,052
60	0,634 ± 0,058	0,436 ± 0,036	0,4957 ± 0,041	0,621 ± 0,044	0,701 ± 0,050
60	0,627 ± 0,057	0,43 ± 0,036	0,485 ± 0,040	0,614 ± 0,044	0,778 ± 0,056
60	0,629 ± 0,057				
60	0,633 ± 0,058				
90	0,424 ± 0,039	0,405 ± 0,034	0,4254 ± 0,035	0,758 ± 0,054	0,801 ± 0,057
90	0,434 ± 0,039	0,396 ± 0,033	0,4136 ± 0,034	0,776 ± 0,055	0,8 ± 0,057
90	0,415 ± 0,038	0,386 ± 0,032	0,4218 ± 0,035	0,759 ± 0,054	0,81 ± 0,058
90	0,423 ± 0,038				
90	0,416 ± 0,038				

The following was noted from Figure 33 for carbon steel material:

- the maximum erosion values were observed at an impact angle of 30° while the minimum erosion values were observed at an impact angle of 90°,
- as the impact angle increases from 30° to 90°, the erosion rate decreases significantly.

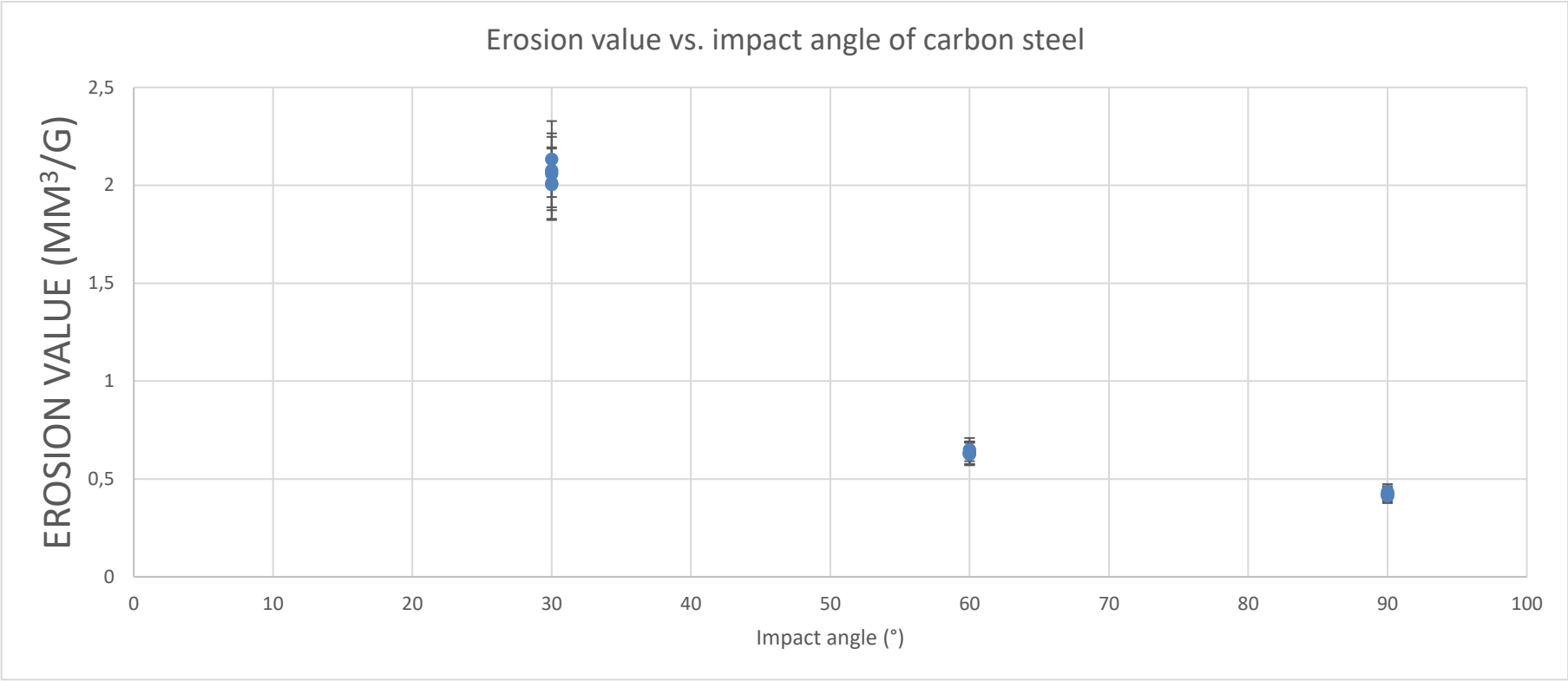

Figure 33: Erosion value vs. impact angle for carbon steel material

The following was noted from Figure 34 for VRN 400 material:

- the maximum erosion values were observed at an impact angle of 30° while the minimum erosion values were observed at an impact angle of 90°,
- as the impact angle increases from 30° to 90°, the erosion rate decreases.

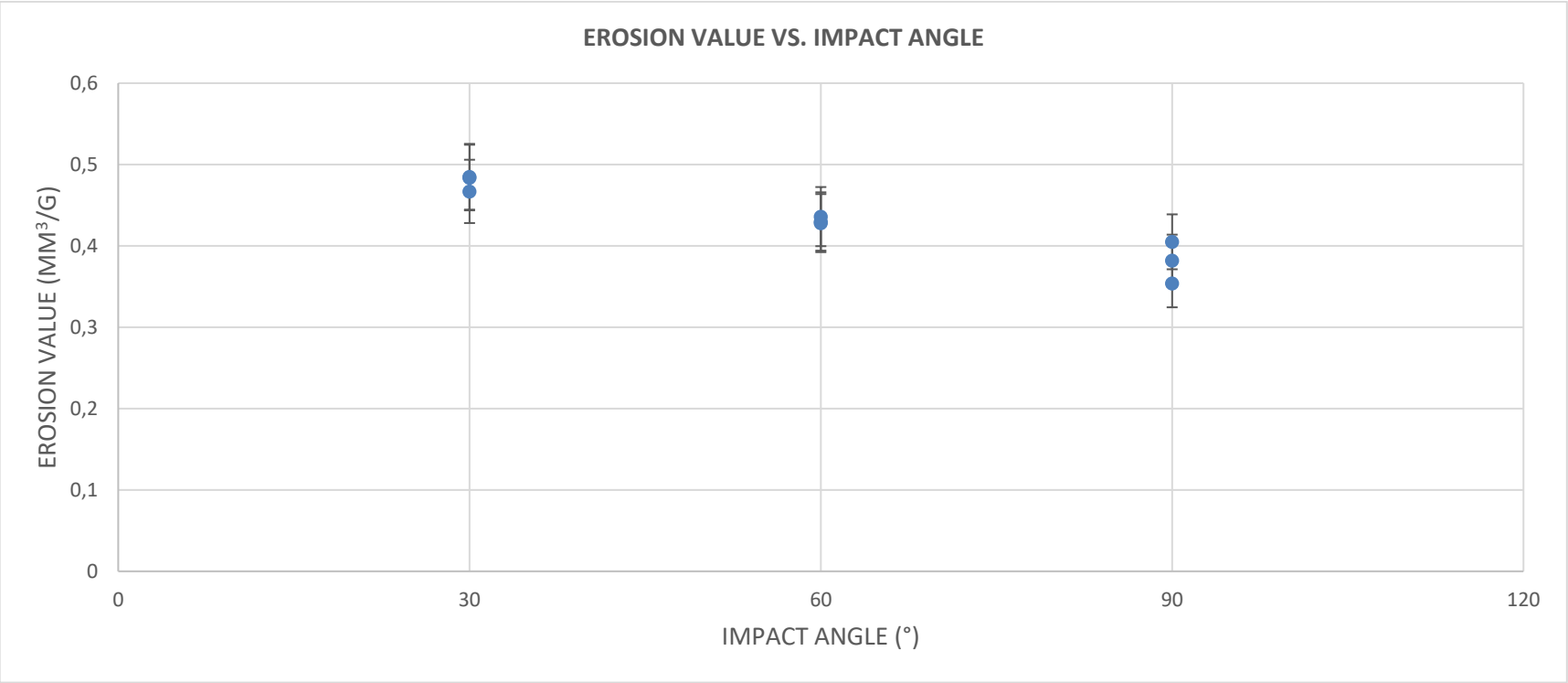

Figure 34: Erosion value vs. impact angle for VRN 400 material

The following was noted from Figure 35 for 96% alumina tile material:

- the maximum erosion values were observed at an impact angle of 90° while the minimum erosion values were observed at an impact angle of 30°,
- as the impact angle increases from 30° to 90°, the erosion rate increases.

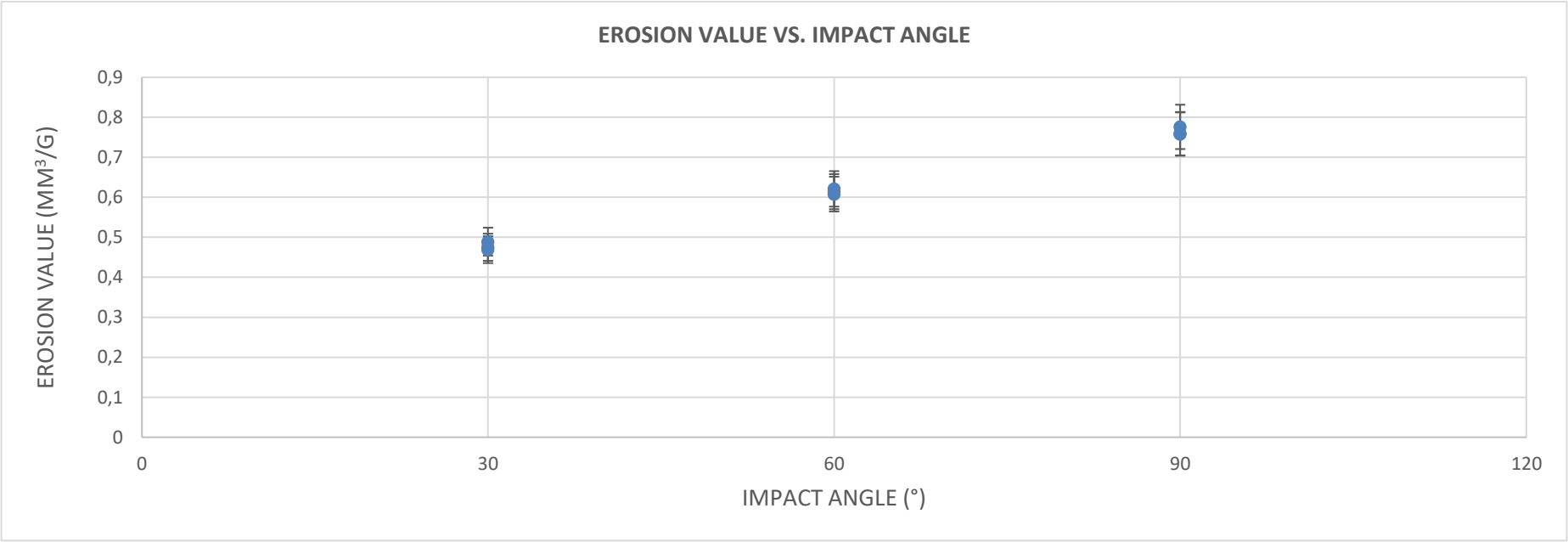

Figure 35: Erosion value vs. impact angle for 96% Alumina tile material

The following was noted from Figure 36 for 92% alumina tile material:

- the maximum erosion values were observed at an impact angle of 90° while the minimum erosion values were observed at an impact angle of 30°,
- as the impact angle increases from 30° to 90°, the erosion rate increases.

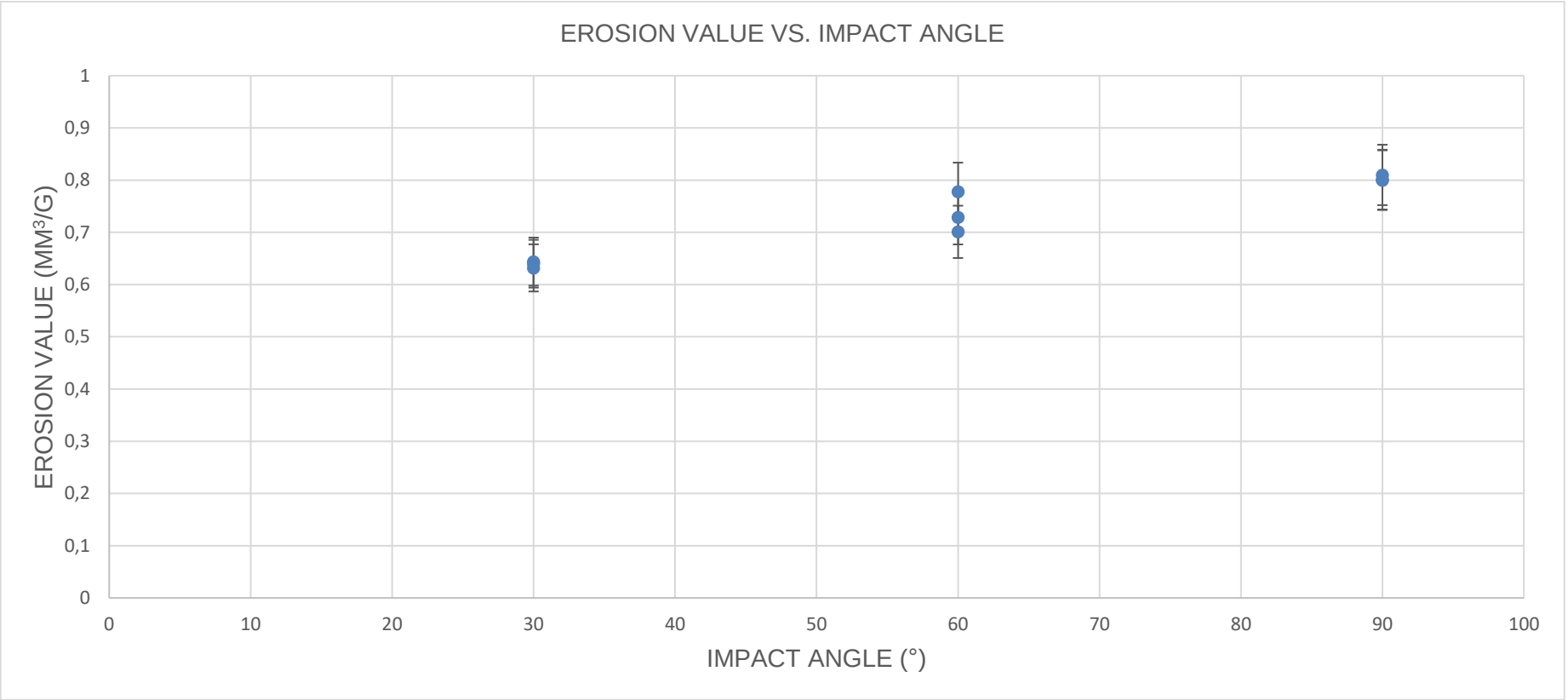

Figure 36: Erosion value vs. impact angle for 92% Alumina tile material

The following was noted from Figure 37 for 316L stainless steel material:

- the maximum erosion values were observed at an impact angle of 60° while the minimum erosion values were observed at an impact angle of 90°,
- as the impact angle increases from 30° to 60°, the erosion rate increases,
- as the impact angle increases from 60° to 90°, the erosion rate decreases.

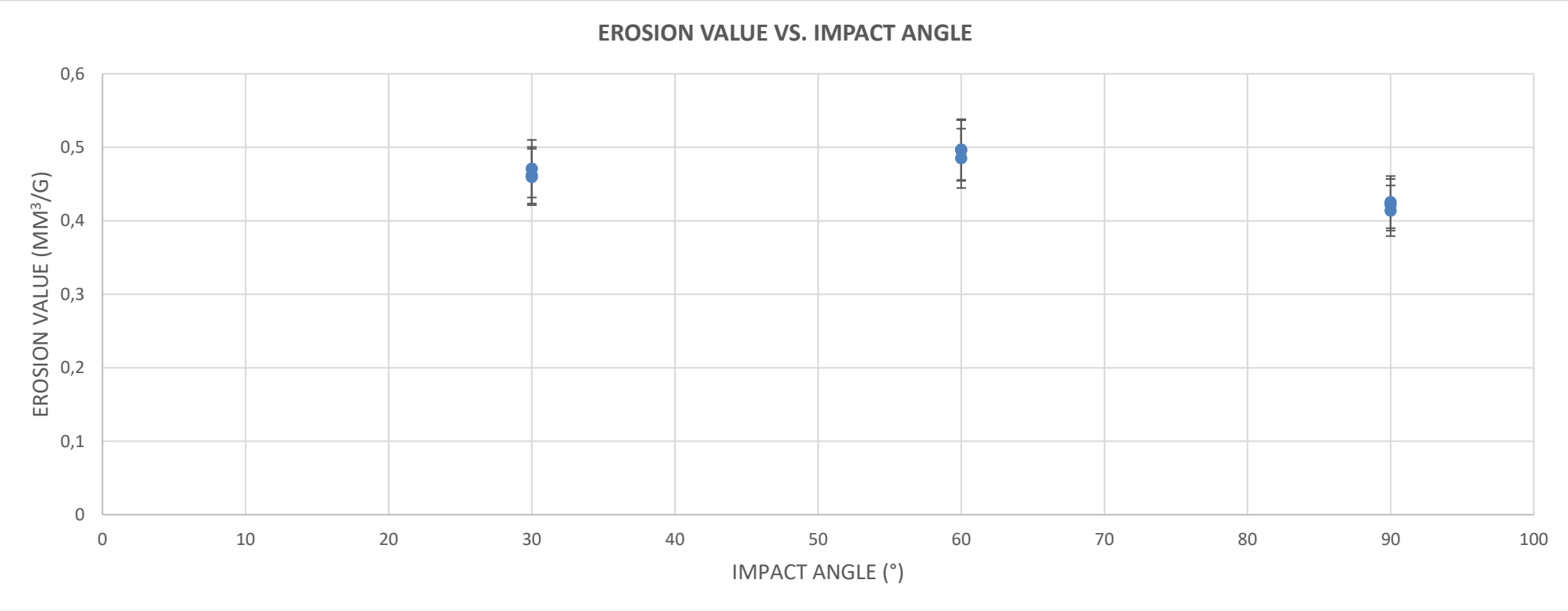

Figure 37: Erosion value vs. impact angle for 316L stainless steel material

Table 13 shows the relative erosion performance based on carbon steel for each pre-selected material at the selected impact angles.

Table 13: Relative erosion values to carbon steel material

	Impact angles		
	30°	**60°**	**90°**
Carbon steel	1,0000	1,0000	1,0000
VRN 400	0,2327	0,6797	0,9367
316L stainless steel	0,2256	0,7761	0,9949
96% alumina tile	0,2322	0,9681	1,8095
92% alumina tile	0,3105	1,1598	1,9026

Based on the relative erosion values (Table 13) to carbon steel at an impact angle of 30°, the 316L stainless steel material showed the best erosion resistance. However, the 96% alumina tile and VRN 400 material proved to be almost as resistant as the 316L stainless steel material. Carbon steel material showed the least erosion resistance at an impact angle of 30°.

Based on the relative erosion values (Table 13) to carbon steel at an impact angle of 60°, VRN 400 material showed the best erosion resistance followed by 316L stainless steel material. The 92% alumina tile material showed the least erosion resistance at an impact angle of 60°.

Based on the relative erosion values (Table 13) to carbon steel at an impact angle of 90°, VRN 400 showed the best erosion resistance while 92% alumina tile material showed the least erosion resistance.

Table 13 shows that VRN 400 and 316L stainless steel material is superior to carbon steel material at all impact angles tested but also shows that 92% alumina tile material has worse erosion resistance than carbon steel at higher impact angles.

The variables which affect the erosion resistance of a material is covered in the literature review. Due to the limitation of available measuring equipment for the particle velocity on the erosion rig as an example, this parameter was not further investigated.

6.4. Scanning electron microscopy results

SEM analysis was performed on each of the highest erosion rate pre-selected materials at 30°, 60° and 90° impact angles. Observations from the SEM analysis of the eroded surfaces are shown in Figure 38 to Figure 40.

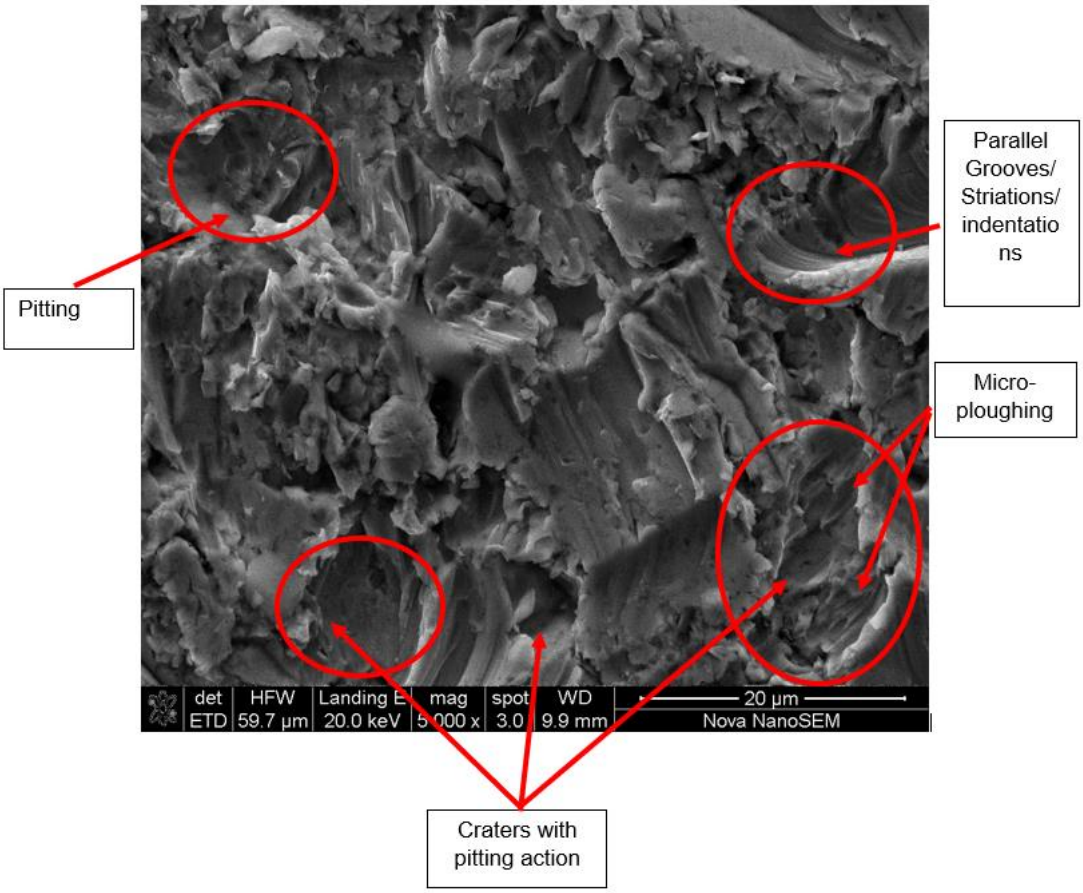

Figure 38: SEM observations of eroded surfaces

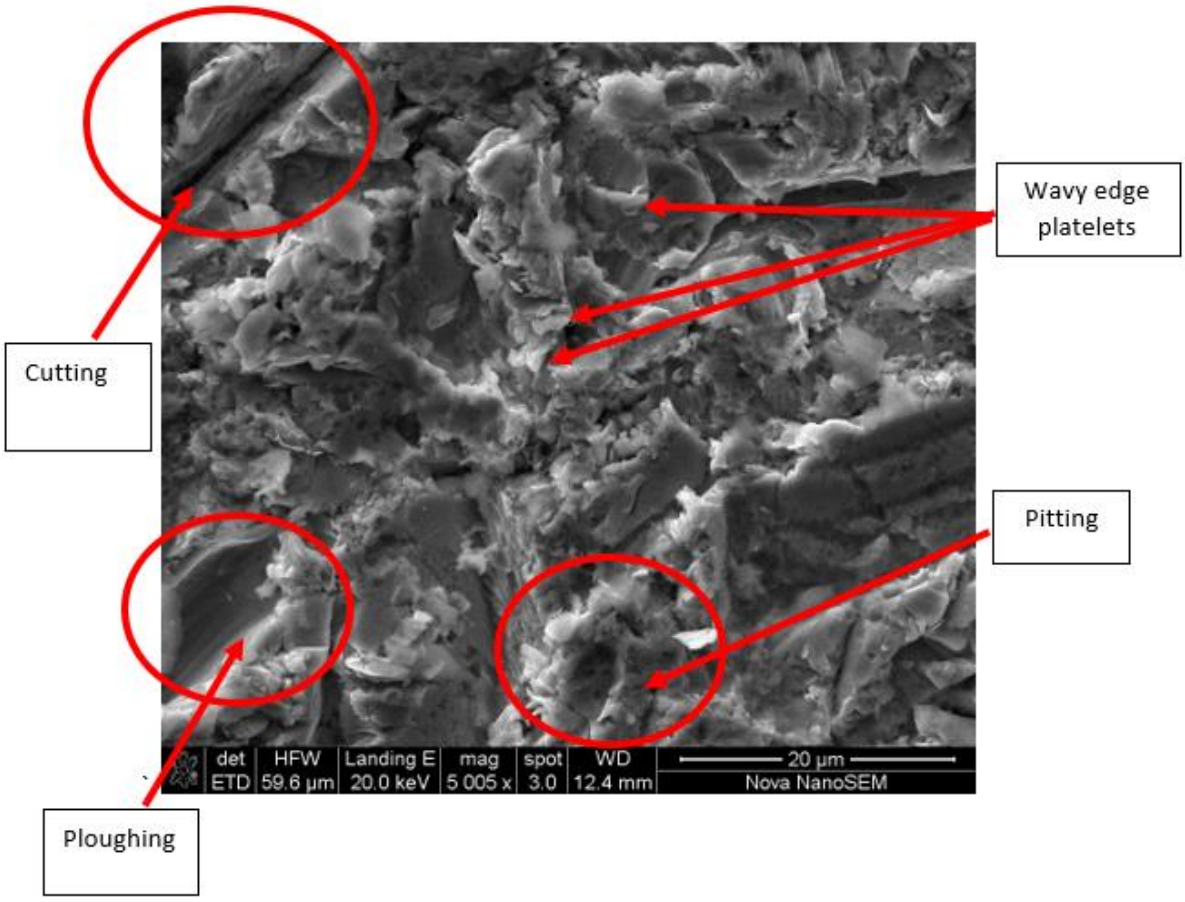

Figure 39: SEM observations of eroded surfaces

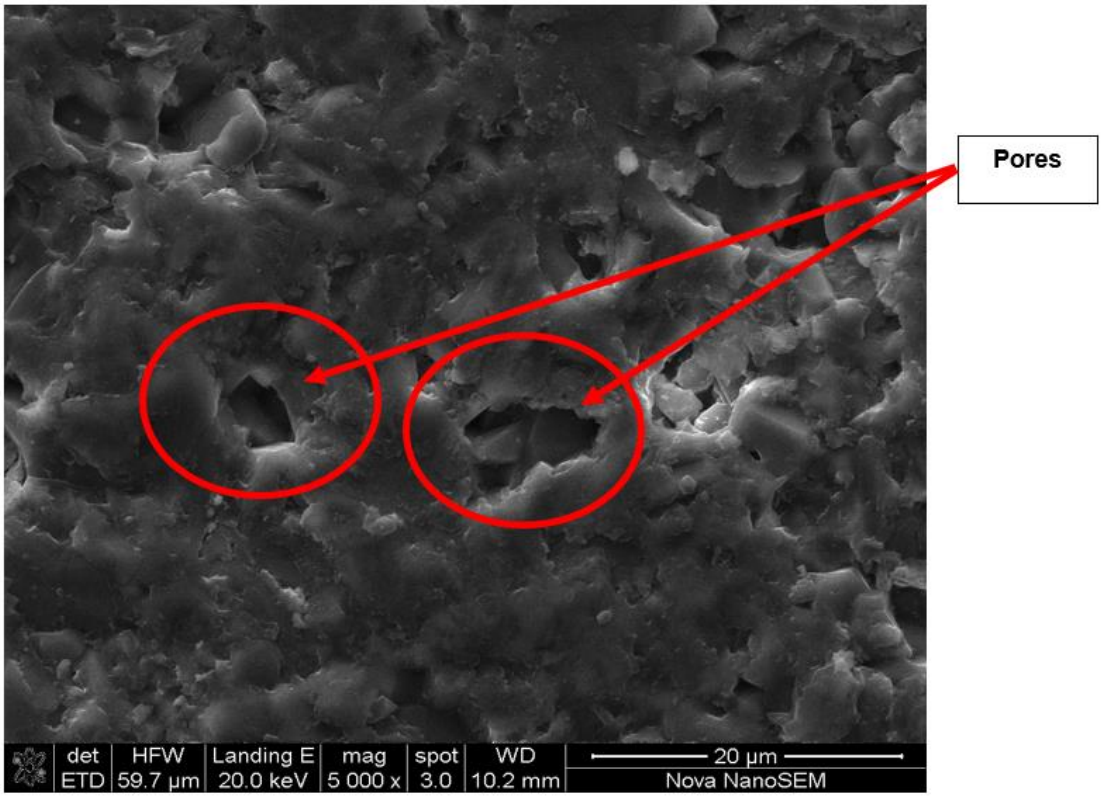

Figure 40: SEM observations of eroded surfaces

The observations from the SEM results of each material at the selected impact angles are discussed below.

Table 14: Carbon steel SEM observations

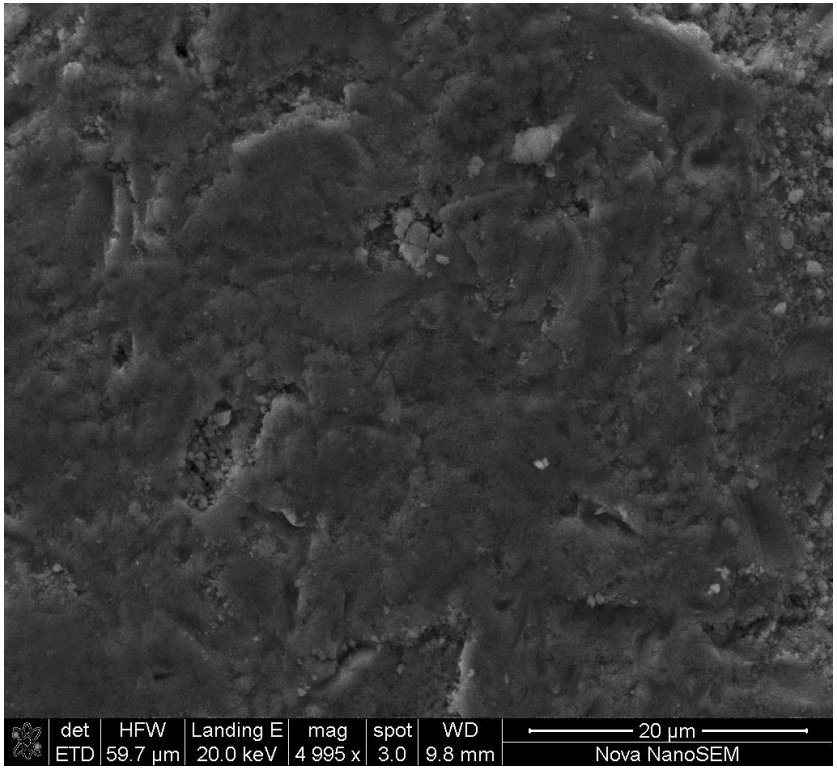

Figure 41: Uneroded Carbon Steel
(Mag: 4995X)

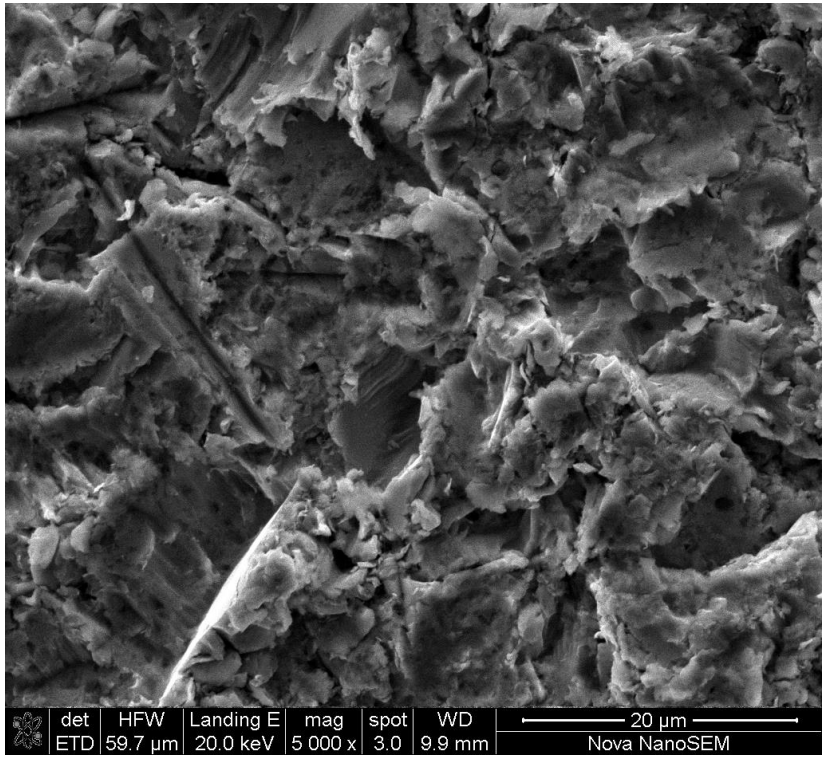

Figure 42: 30° impact angle (Mag: 5000X)

- Cutting action
- Pitting,
- craters,
- parallel grooves/striations/indentation,
- wavy edge platelets

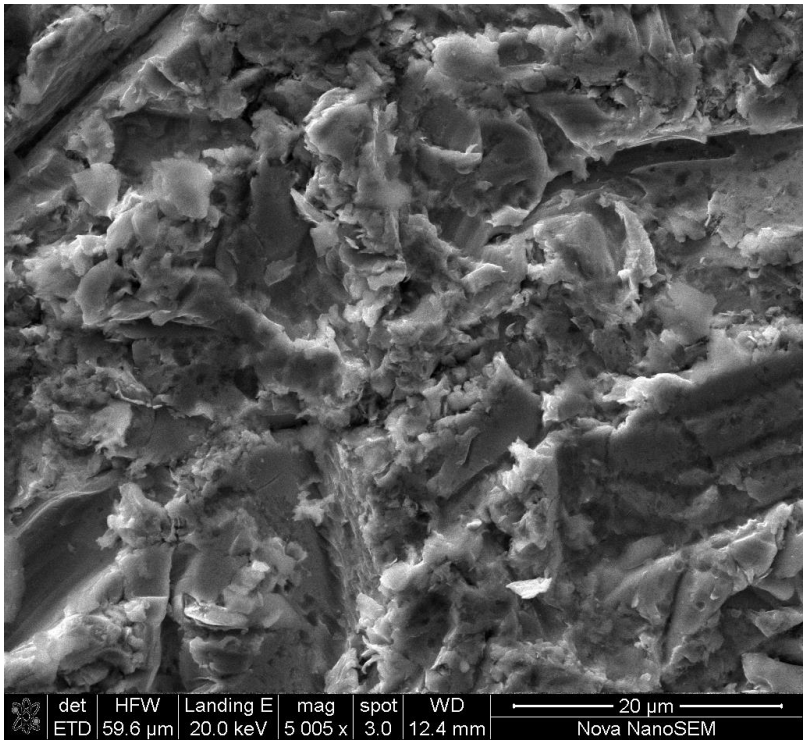

Figure 43: 60° impact angle (Mag: 5005X)

- Pitting,
- craters,
- ploughing action,
- wavy edge platelets

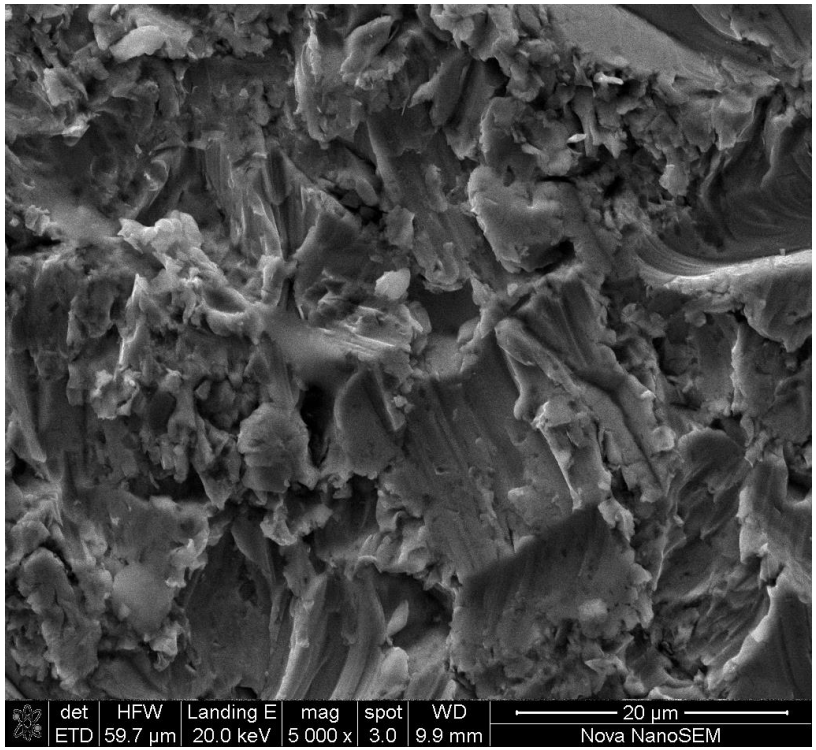

Figure 44: 90° impact angle (Mag: 5000X)

- Pitting,
- craters,
- ploughing action
- wavy edge platelets

Table 15: VRN 400 Material SEM observations

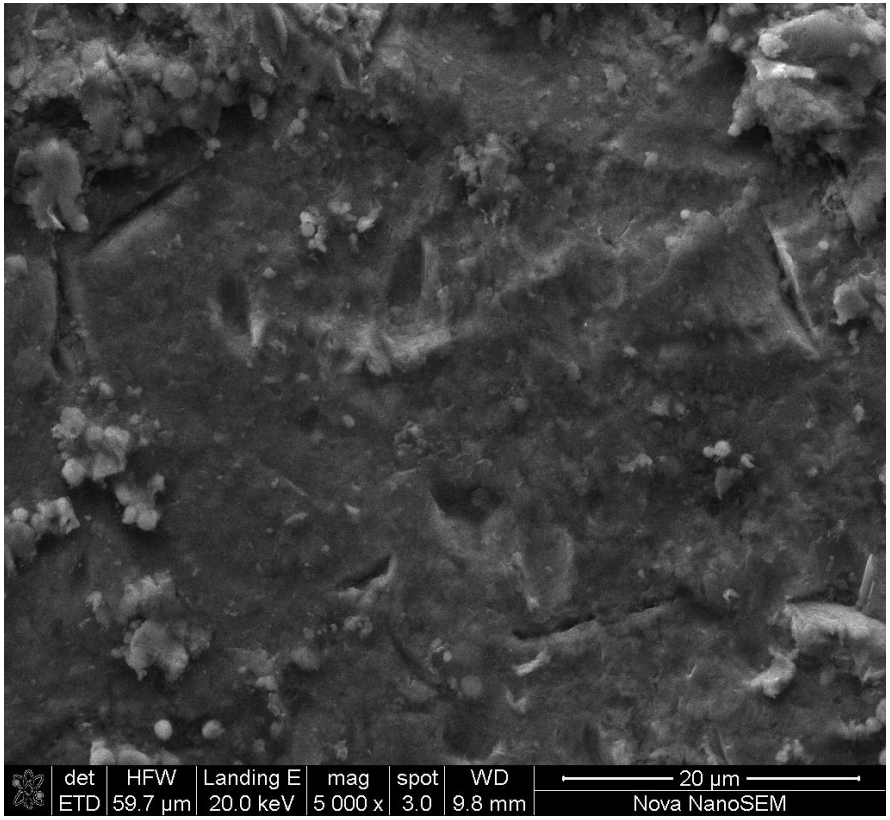

Figure 45: Uneroded VRN 400 material
(Mag 5000X)

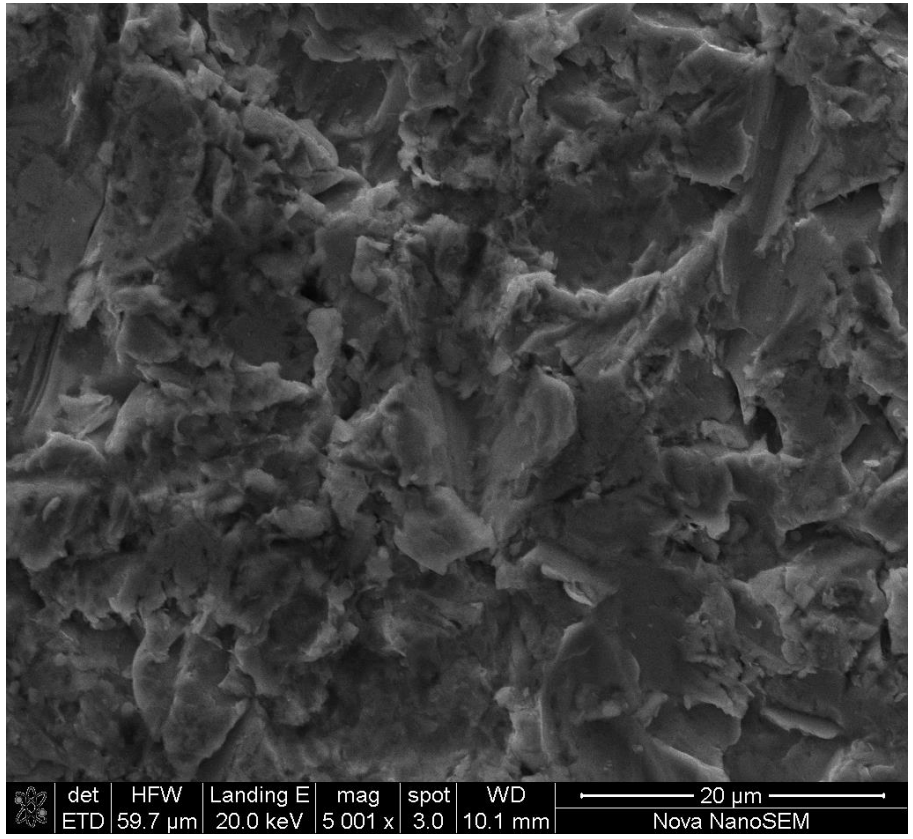

Figure 46: VRN 400 material at 30° impact angle
(Mag 5000X)

- Craters and
- Cutting action

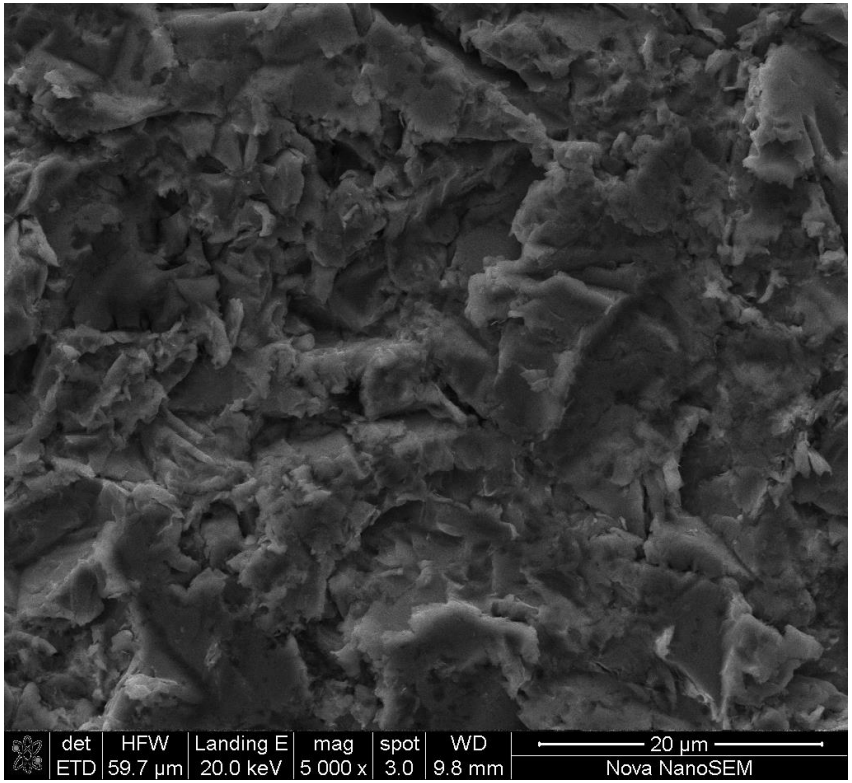

Figure 47:VRN 400 material at 60° impact angle
(Mag: 5000X)

- Craters,
- Ploughing/cutting action

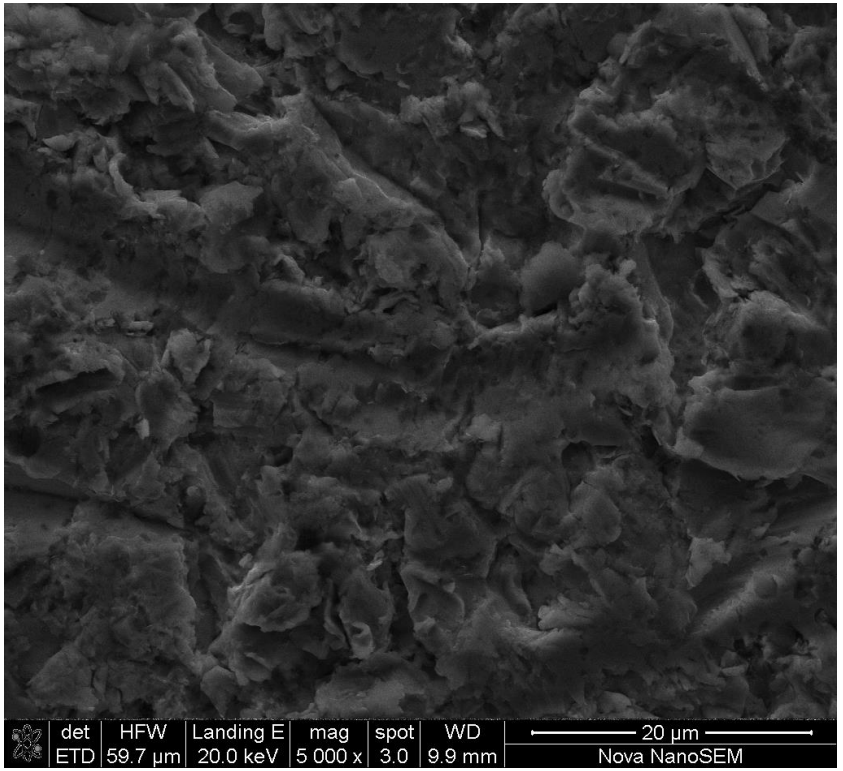

Figure 48: VRN 400 material at 90° impact angle
(Mag: 5000X)

- Craters,
- Ploughing action

Table 16: 316L SS Material SEM observations

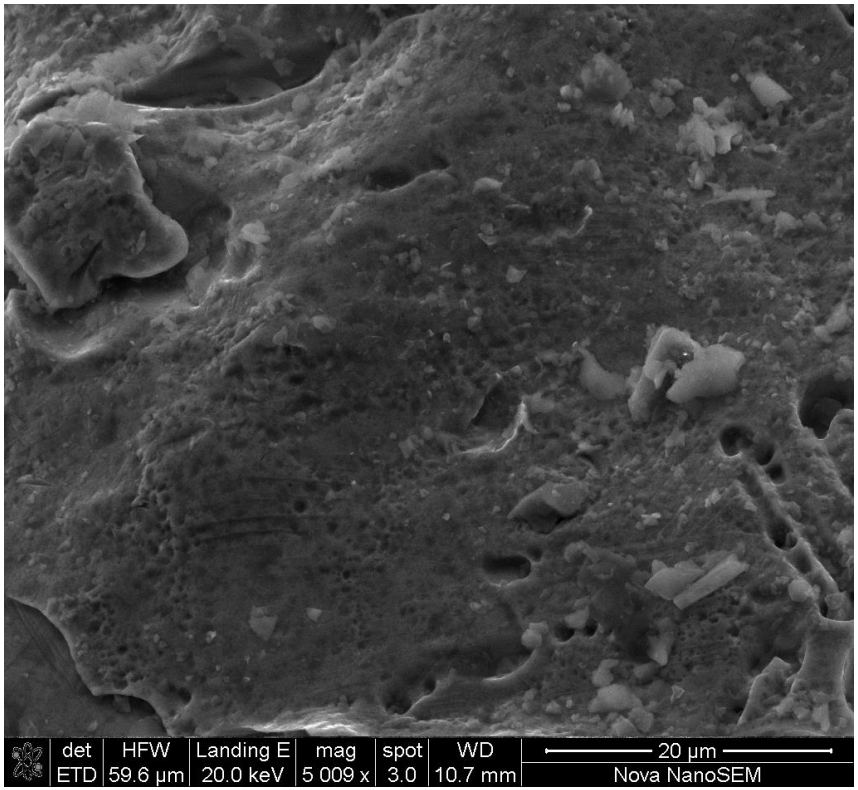

Figure 49: Uneroded 316L SS material
(Mag: 5009X)

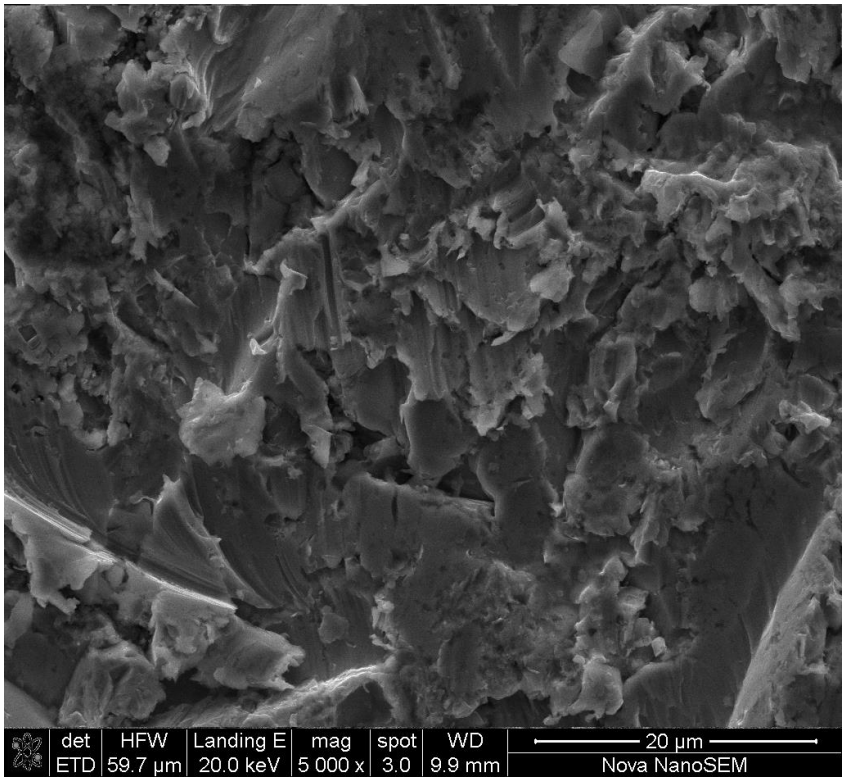

Figure 50: 316L SS material (30° impact angle)
(Mag: 5000X)

- Cutting action
- Craters
- Pitting
- Grooving / parallel indentation

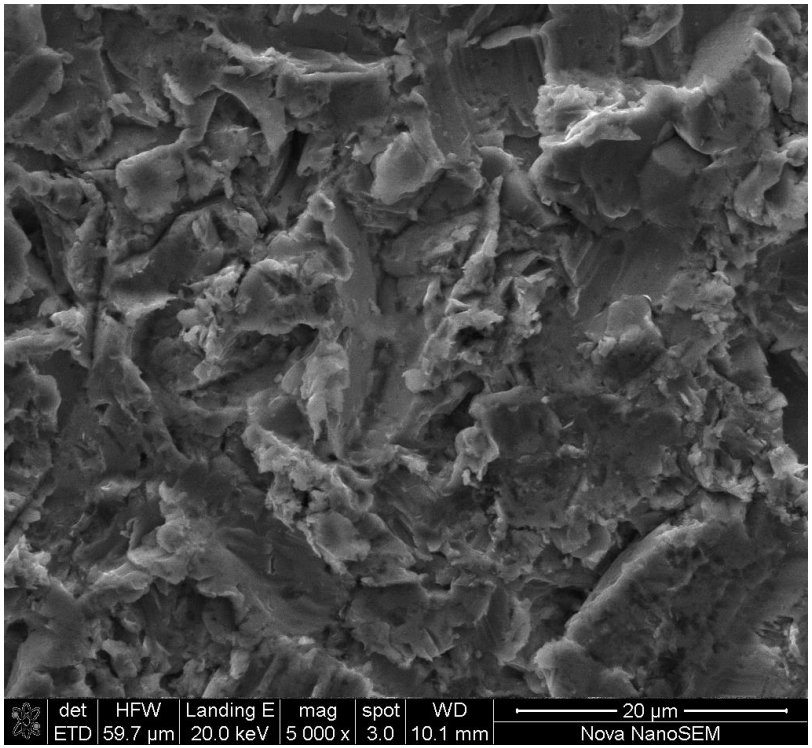

Figure 51: 316L SS material (60° impact angle)
(Mag: 5000X)

- Ploughing action
- Craters
- Pitting

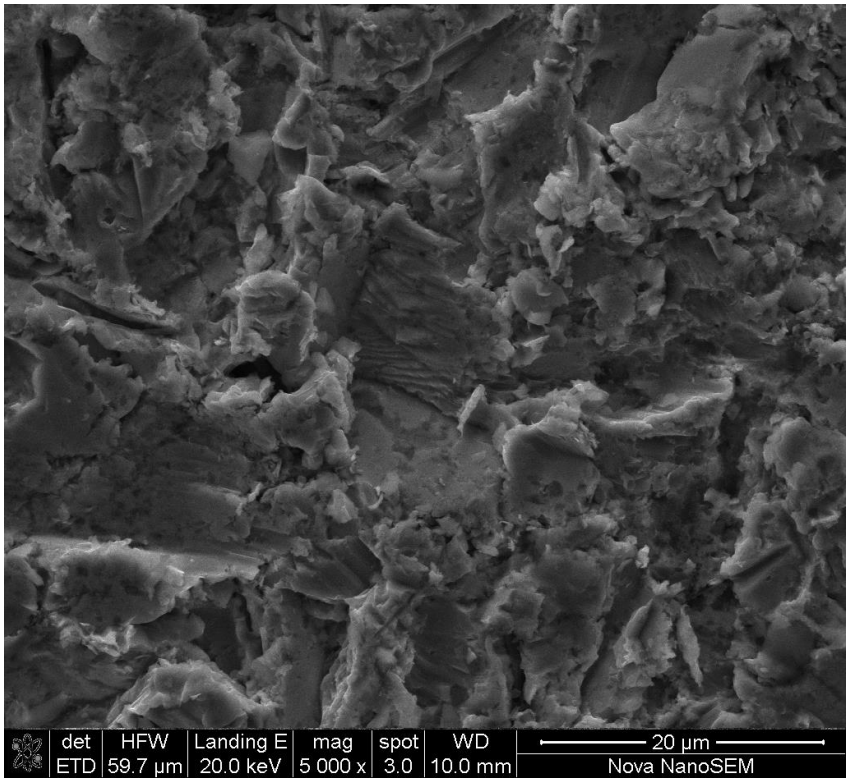

Figure 52: 316L SS material (90° impact angle)
(Mag: 5000X)

- Craters
- Pitting
- Grooving / parallel striations

Table 17: 92% Alumina Tile Material SEM observations

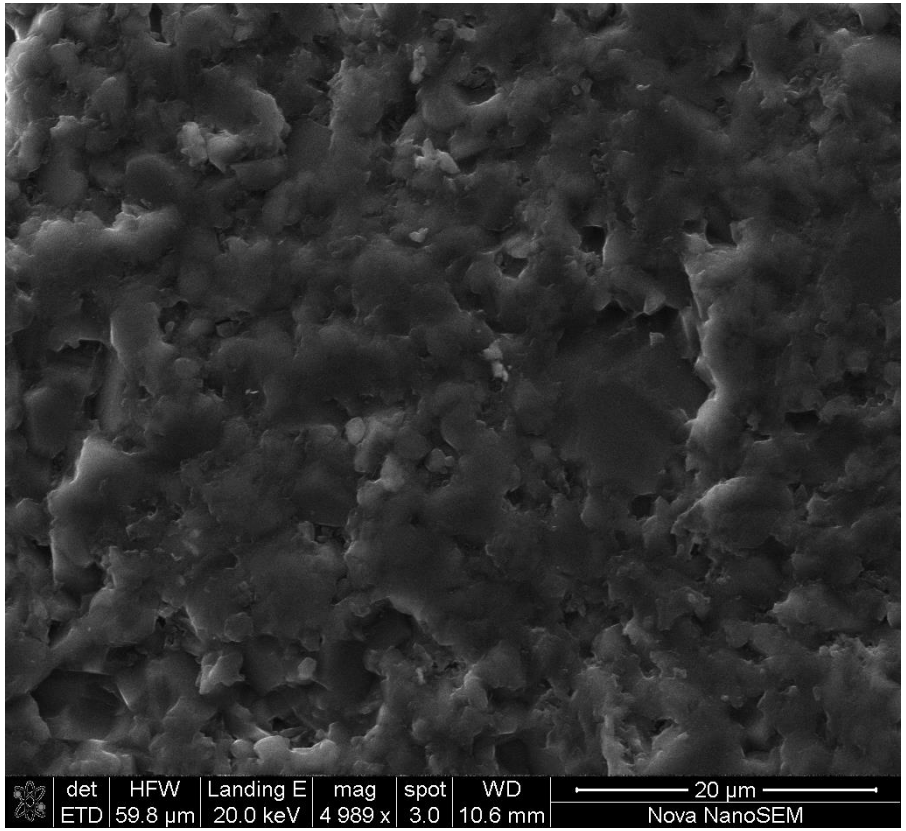

Figure 53: Uneroded 92% Alumina Tile material
(Mag: 4989X)

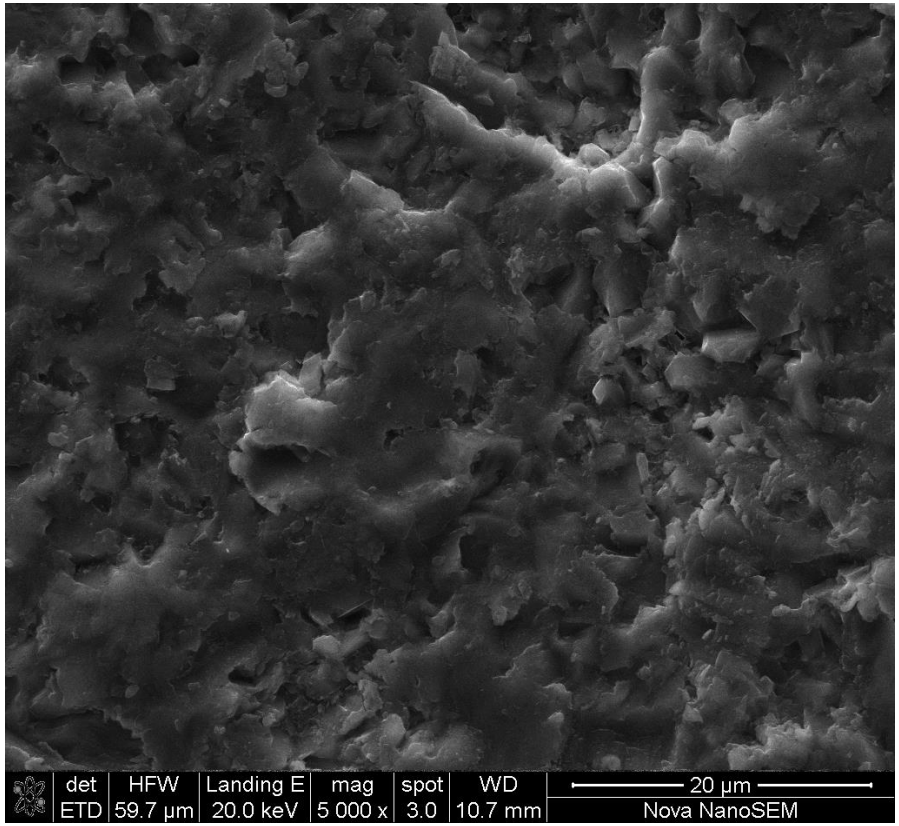

Figure 54: 92% Alumina Tile material (30° impact angle)
(Mag: 5000X)

- There was minimum change in the material surface when compare to the un-eroded surface,
- Pitting/pores

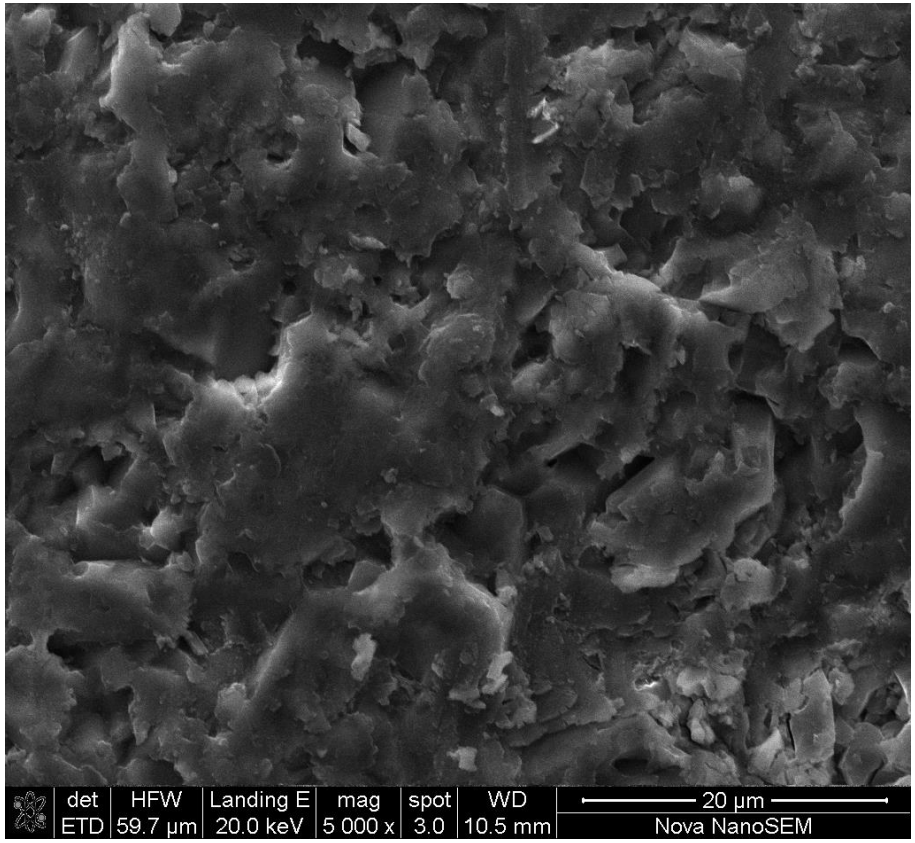

Figure 55: 92% Alumina Tile material (60° impact angle)
(Mag: 5000X)

- Minimum change in the material surface when compare to the un-eroded surface,
- Pitting/pores

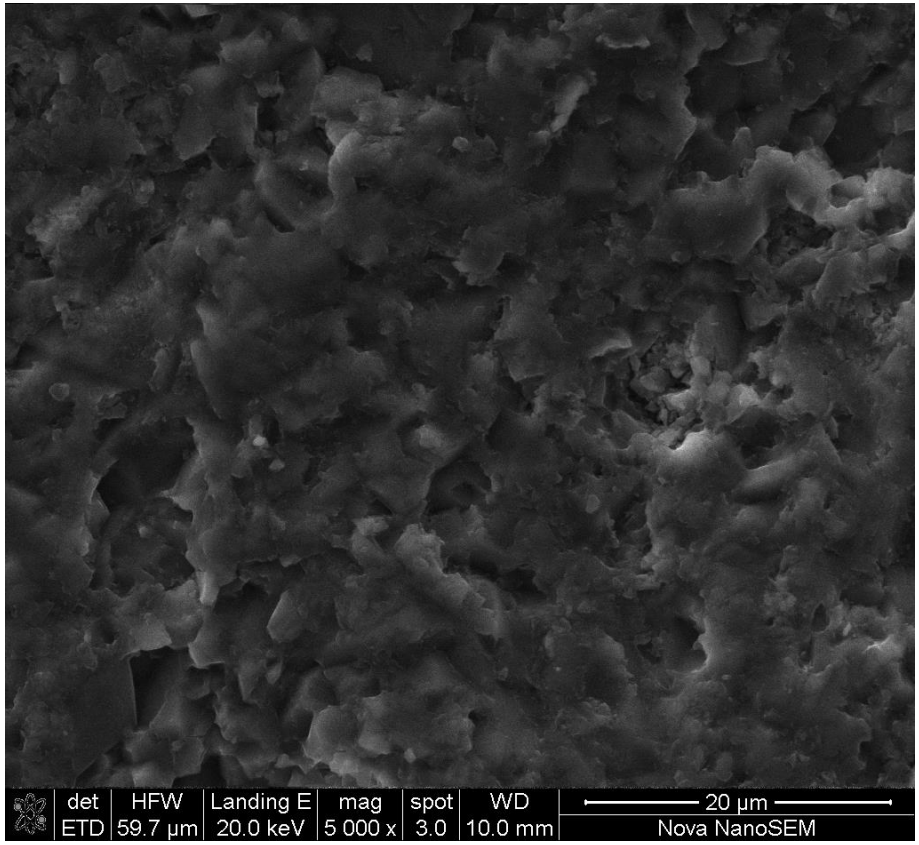

Figure 56: 92% Alumina Tile material (90° impact angle)
(Mag: 5000X)

- Pitting/pores

Table 18: 96% Alumina Tile Material

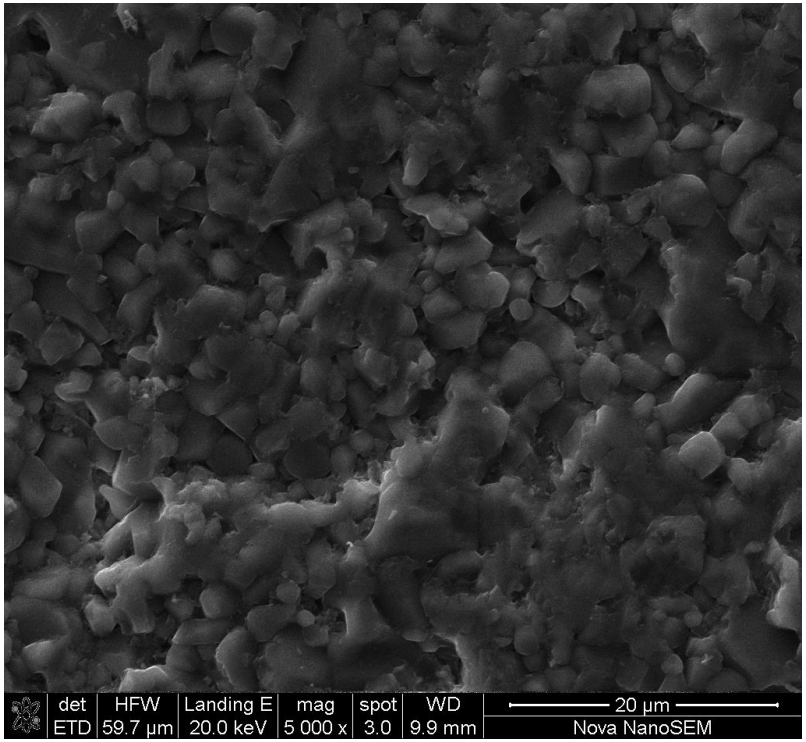

Figure 57: Uneroded 96% Alumina Tile material
(Mag: 5000X)

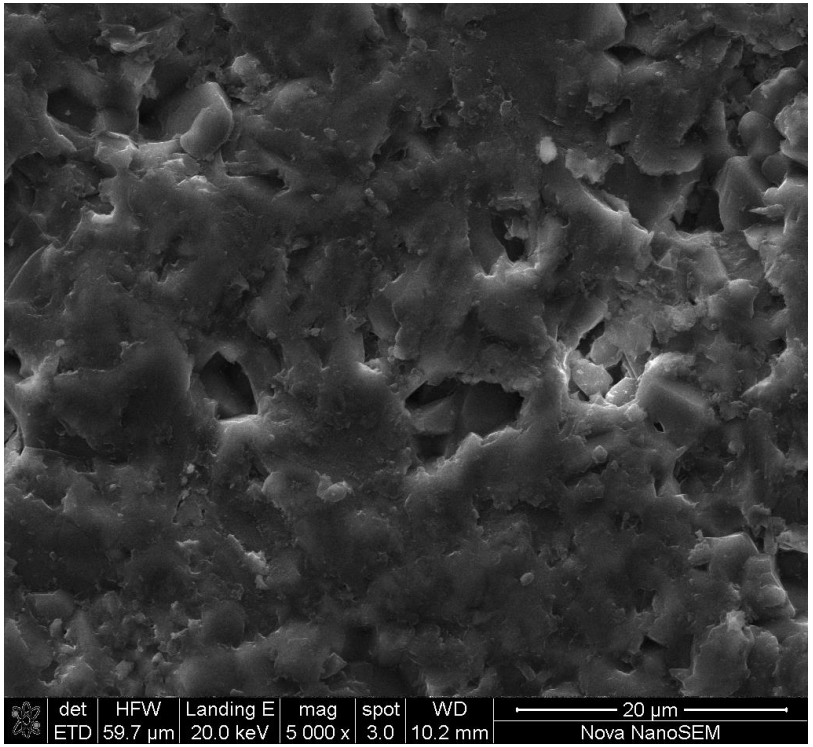

Figure 58: 96% Alumina Tile material (30° impact angle)
(Mag: 5000X)

- Pitting/pores

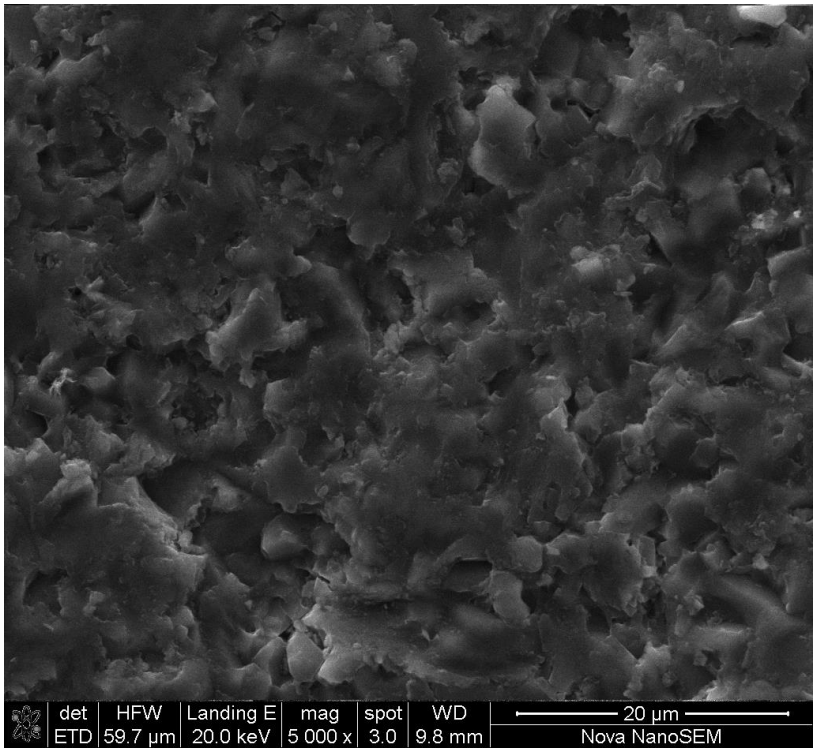

Figure 59: 96% Alumina Tile material (60° impact angle) (Mag: 5000X)

- Pitting/pores

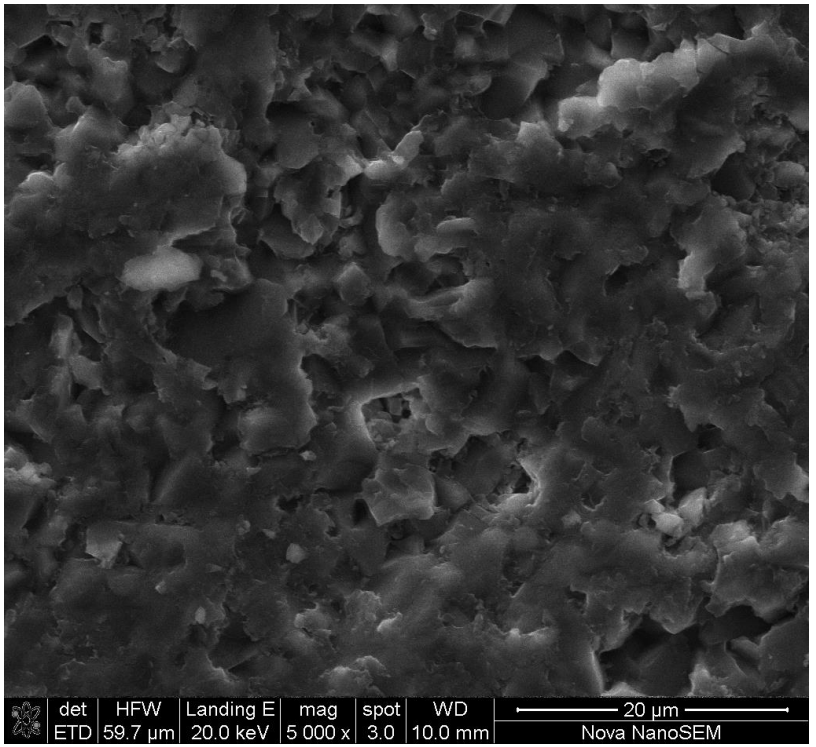

Figure 60: 96% Alumina Tile material (90° impact angle) (Mag: 5000X)

- Pitting/pores

From the SEM results for carbon steel material, there was material build up which formed "platelets" around the impact of the crater which is a characteristic of plastic deformation. For carbon steel material, platelets are initially extruded from shallow craters made by the impacting particle and the removal of material occurs through the processes of micro-plastic deformation and/or brittle fracture. From the SEM analysis it was observed that room temperature erosion of carbon steel materials is due to cutting wear and plastic deformation. This was also observed by Mbabazi [4]. The SEM results for carbon steel material (ductile material) correlates with published literature.

For brittle material, pitting/pores was observed and as the impact angle is increased from 30° to 90°, the pitting/pores are observed to be more prominent. The increased number of pores at a 90° impact angle can be attributed to the higher erosion rate when compared to the 30° impact angle. The pores make the material more susceptible to material loss each time the abrasive hits the surface. Feng [36] , Wellman [39] and other authors observed pores in eroded brittle materials via SEM analysis.

The SEM observations for 316L stainless steel material (semi-ductile), are similar to that of the ductile materials tested. This behaviour was observed in published literature [8].

Chapter 7: Conclusion

QEMSCAN analysis was performed on commercially available abrasives and on fly ash and PF from coal fired power plants in SA and Al_2O_3 was selected as the most appropriate abrasive to be used in the experiments.

From the experimental results, for carbon steel and VRN 400 materials, as the impact angle increases from 30**°** to 90**°**, the erosion rate decreases while for 92% and 96% Alumina tile materials, as the impact angle increases from 30**°** to 90**°**, the erosion rate increases and for 316L stainless steel material, the maximum erosion value was observed at 60**°**. These results correlate with published literature.

Based on published literature, when considering the erosion value vs. impact angle of the pre-selected materials, the experimental results confirm that carbon steel and VRN 400 materials behave in a ductile manner, 92% and 96% alumina tile materials behave in a ductile manner and 316L stainless steel material behaves in a semi-ductile manner.

From SEM analysis, it was observed that cutting wear occurred at low impact angles (30°) and deformation wear occurred at high impact angles (90°) ductile materials and for brittle

materials, pitting/pores was observed and as the impact angle is increased from 30° to 90°, the pitting/pores are observed to be more prominent, while for semi-ductile material, the observations were similar to that of ductile materials for all angles of impact tested.

The ranking of the pre-selected materials for each material in terms of best erosion protection material to worst erosion protection material from this research is as follows:

- At 30° impact angle: 316L stainless steel > 96% alumina > VRN 400 > 92% alumina > carbon steel
- At 60° impact angle: VRN 400 > 316L stainless steel > 96% alumina > carbon steel > 92% alumina
- At 90° impact angle: VRN 400 > 316L stainless steel > carbon steel > 96% alumina > 92% alumina

Actual erosion service involves particle shapes and sizes, impact angles, environments, and so forth, that will vary over a wide range. Hence, any single laboratory test may not be sufficient to evaluate expected service performance or to provide recommendations on the exact wear protection material to use at a specific location of a coal fired power plant. The design and/or maintenance team at a coal fired power plant can use the current experimental results of the wear protection materials per impact angle together with the actual plant design, operational conditions, available budgets and so forth to decide on which material will best suit a plant location/component.

The selecting of the most appropriate material for each power plant application will depend on many factors but are not limited to the following:

- weight of material (structural integrity must not be compromised),
- impact angle experienced,
- installation,
- cost,
- maintenance of the protection material,
- inspection methods/technology for each material
- criticality (risk/consequence of failure) of the component being protected,
- nature of the environment (corrosion, temperature, pressure, velocity).

References

[1] D. Aquaro and E. Fontani, Erosion of Ductile and Brittle Materials, 2002

[2] S.K. Das, K.M. Godiwalla, Shubha S. Hegde, S.P. Mehrotra, P.K. Dey, A mathematical model to characterize effect of silica content in the boiler fly ash on erosion behaviour of boiler grade steel, 2007

[3] E. Raask, Mineral Impurities in Coal Combustion, Behaviour, Problems, and Remedial Measures, Hemisphere Publishing Corporation, 1985

[4] J.G. Mbabazi, T.J. Sheer, R. Shandu, A model to predict erosion on mild steel surfaces impacted by boiler fly ash particles, 2004

[5] S K Das, K M Godiwalla, S P Mehrotra, K M Sastry and P K Dey, Analytical model for erosion behaviour of impacted fly-ash particles on coal-fired boiler components, 2006

[6] Ritesh Kaundal, Amar Patnaik, Alok Satapathy, Solid Particle Erosion of Short Glass Fiber Reinforced Polyester Composite, 2012

[7] Aglan, H.A., and Chenock Jr, T.A., Erosion damage features of polyimide thermoset composites, 41-47, 1993

[8] Juan R. Laguna-Camacho, M. Vite-Torres, E.A. Gallardo-Hernández and E.E. Vera-Cárdenas, Solid Particle Erosion on Different Metallic Materials

[9] An Optoelectronic Abrasive Particle Velocimeter, in V. Srinivasan and K. Vedula (eds.), Corrosion and particle erosion at high temperature, The minerals, Metals and Materials Society 1989; 349-368

[10] J. R. Laguna Camacho, An analysis of the solid particle erosion damage caused on AISI 304, 2014

[11] D.O. Moumakwa, K. Marcus, Tribology in coal-fired power plants, 2005

[12] Mater Lett, Erosion of alumina and silicon carbide at low impact velocities, 55:269–73, 2002

[13] Yu-Fei Wang, Zhen-Guo Yang, Finite element model of erosive wear on ductile and brittle materials, 2008

[14] M.S. ElTobgy, E. Ng, M.A. Elbestawi, Finite element modeling of erosive wear, 2005

[15] D. Alman, J. Tylczak, J. Hawk, M. Hebsur, Solid particle erosion behaviour of an Si3N4-MoSi2, Mater. Sci. Eng. A261 (1999) 245-251

[16] J. Bitter, A study of erosion phenomena, part 2, Wear 8 (1963) 161–190

[17] D. Alman, J. Tylczak, J. Hawk, M. Hebsur, Solid particle erosion behavior of an Si3N4–MoSi2, Mater. Sci. Eng. A261 (1999) 245–251

[18] D. Aquaro, E. Fontani, Erosion of ductile and brittle materials, Mecanica 36 (2001) 651–661, 2002

[19] Henk Wensink, Miko C. Elwenspoek, A closer look at the ductile-brittle transition in solid particle erosion, 2002

[20] G.L. Sheldon, I. Finnie, The ductile behaviour of nominally brittle materials during erosive cutting, J. Eng. Ind. 88 (1966) 387-392]

[21] Jianren Zhou, Shyam Bahadur, Erosion characteristics of alumina ceramics at high temperatures, 1994

[22] J.R. Zhou and S. Bahadur, High-temperature erosion-corrosion behavior of stainless steels, in V. Srinivasan and K. Vedula (eds.), Corrosion and Particle Erosion at High Temperatures, TMS, Warrendale, 1989, pp. 315-333

[23] Minghao Fang, FengjiaoLiu, XinMin, ZhaohuiHuang, Yan'gai Liu, XiaowenWu, Chao Tang, LinaZhang, FeiPeng, Effect of temperature on solid particle impact erosion wear mechanism of 5 mol% Yttria Stabilized Zirconia ceramics, 2015

[24] Xiaojun Wang, Solid particle erosion of alumina ceramics at elevated temperature, 2013

[25] W. Tabakoff, R. Kotwal and A. Hamed, Erosion study of different materials affected by coal ash particles, 1978

[26] Allan V. Levy and Pauline Chik, The Effects of Abrasive Composition and Shape on the Erosion of Steel, 1982

[27] G. P. Tilly and Wendy Sage, The Interaction of Particle and Material Behaviour in Erosion Processes, 1970

[28] G.P. Tilly, A two stage mechanism of ductile erosion, Wear 23 (1973) 87-96

[29] S. Yerramareddy, S. Bahadur, Effect of operational variables, microstructure and mechanical properties on the erosion of Ti-6Al-4V, Wear 142 (1991) 253-263.

[30] Martin Suckling, Thesis on High Temperature Erosive Wear of a Boiler Tube Steel, UCT, 1996

[31] A.W. Ruff & L.K. Ives, Measurement of Solid particle velocity in erosive wear, Wear 35, 1975, 195-199

[32] P.H. Shipway & I.M. Hutchings, A method for optimising the particle flux in erosion testing with a gas blast apparatus, Wear 17 4, 1994, 169-175.

[33] Y. Shida & H. Fujikawa, Particle erosion behaviour of boiler tube materials at elevated temperature, April 1985

[34] Fry et al, Metrology to Enable High Temperature Erosion Testing – A New European Initiative

[35] I. M. Hutchings, Tribology: Friction and Wear of Engineering Materials, Boca Raton, Fl: CRC Press, 1992

[36] Z. Feng, The Erosion of Materials, UCT, 1998

[37] Shipway, P.H. and Hutchings, I. M., Wear, 162-164, 1993, 148

[38] J H Morris, The Tribological and wear properties of carbon-graphite composites, UCT, 1994

[39] R.G. Wellman, Solid Particle Erosion of Ceramics, UCT, 1993

[40] R.C. Pennefather, The Solid Particle Erosion of WC-Co Alloys, UCT, 1986

[41] Erosion Studies, Chapter 5, http://shodhganga.inflibnet.ac.in/bitstream/10603/11559/10/10_chapter%205.pdf

[42] J Polym Eng, Erosion characteristics of Teflon under different operating conditions, 2015; 35(9): 889–904

[43] Paul C. Okonkwo et al, Erosion Behaviour of API X100 Pipeline Steel at Various Impact Angles and Particle Speeds, 2016

[44] ASTM G76 - 07, Standard Test Method for Conducting Erosion Experiments by Solid Particle Impingement Using Gas Jets, https://www.astm.org/DATABASE.CART/HISTORICAL/G76-07.htm

[45] Standard Terminology Relating to Wear and Erosion, https://www.astm.org/Standards/G40.htm

[46] Morrison et al, Erosion of 304 stainless steel, 1985

[47] Malik et al, Evaluating the Effect of Hardness on Erosion Characteristics of Aluminium and Steels, 2014

[48] QEMSCAN, Centre for minerals research, UCT, http://www.cmr.uct.ac.za/cmr/ra/process-mineralogy-qemscan

APPENDICES

Appendix A : Material data

Cust order no. PO101321

Order no.	Cert Number
MP 8053583	P26583 A

Gross mass 6130 Kg Invoice mass - 5652 Kg

SAP Order number	Transport	Page
1700593178	ROAD	1 of 1

Dimensions (mm): 12000 X 3000 X 010,00

GENESIS STEEL (PTY) LTD
PO Box 10265
DALVIEW
1544

STEEL PLATES
Material supplied: AS ROLLED
Test piece condition: 10 - AS ROLLED

INSPECTION CERTIFICATE
AS PER EN10204: 2004; TYPE 3.1

ArcelorMittal South Africa Limited
Reg. No 1989/002164/06
Vanderbijlpark Works

ArcelorMittal

Specification: EN 10025-2-S355JR+AR 2004

SPECIFICATION REQUIREMENTS

CEQ Formula 1: C + MN/6 + (CR + MO + V) / 5 + (NI + CU)/15
CEQ Formula 2:

Impact: Subsize charpy specimen on thickness less than 12mm

Temperature	Positions	Single values	Average values	Temperature	Positions	Single values	Average values

Tensile: Test piece Positions	YS (MPa) Min	YS (MPa) Max	TS (MPa) Min	TS (MPa) Max	EL %	RA Min	Hardness Unit	Hardness Min	Hardness Max	Bend Angle	Bend Dia	Grain Type Min	Grain Type Max
TX	355		470	630	20,0								

Chemical Analysis

	Elements	C %	MN %	P %	S %	SI %	N %	AL %	CU %	MO %	V %	NI %	CR %	NB %	TI %	B %	CEQ1	Hot Temp	Hot Value
Ladle	Minimum							0,0200											
Ladle	Maximum	0,2400	1,6000	0,0350	0,0350	0,5500			0,5500								0,47		
Product	Elements																		
Product	Minimum																		
Product	Maximum																		

TEST RESULTS

Impact Tests: Test piece Dimensions (mm) Wth, Thk; Test piece position and cond; Temp °C; Results Deca-Joules 1, 2, 3, Avrg.; Lat. Exp. — (no entries)

Hardness Test (* if applicable HR-W) — (no entries); Hot Test — (no entries)

Cast no. / Lift card	Serial Tested	Qty	# Tensile tests: Test piece position and cond	YS (MPa) (0,2%)	TS (MPa)	Yield / Tensile Ratio	EL 5,65*√A %	RA %
F804089 VPC73109	2033	001	TX 10	387	566	0,68	28	
F804272 VPC73109	4290	001	TX 10	355	512	0,69	30	

Cast no.	ANAL	C / MO %	MN / V %	P / NI %	S / CR %	SI / NB %	N / TI %	AL / B %	CU %	CEQ1 / CEQ2
F804089	L	0,1630 / 0,0030	1,4550 / 0,0520	0,0160 / 0,0100	0,0038 / 0,0290	0,1640 / 0,0010	0,0051 / 0,0010	0,0340 / 0,0003	0,0100	0,42
F804272	L	0,1245 / 0,0040	1,3850 / 0,0540	0,0230 / 0,0080	0,0036 / 0,0280	0,1640 / 0,0010	0,0038 / 0,0010	0,0290 / 0,0002	0,0100	0,37

Purchaser's Authorised Inspection Representative

MCSTHWP000009 Tensile testing metallic materials based on ASTM E8, BS EN ISO 6892-1, BS EN ISO 10002-1. ASTM A370, JIS Z2241, ASTM E517 and ASTM E646

SERIALS TESTED MAY DIFFER FROM CONSIGNMENT NOTE SERIALS AS ALL MATERIAL DOESN'T REQUIRE TESTING AS PER SPECIFICATION

Figure 61: Carbon steel material data certificate

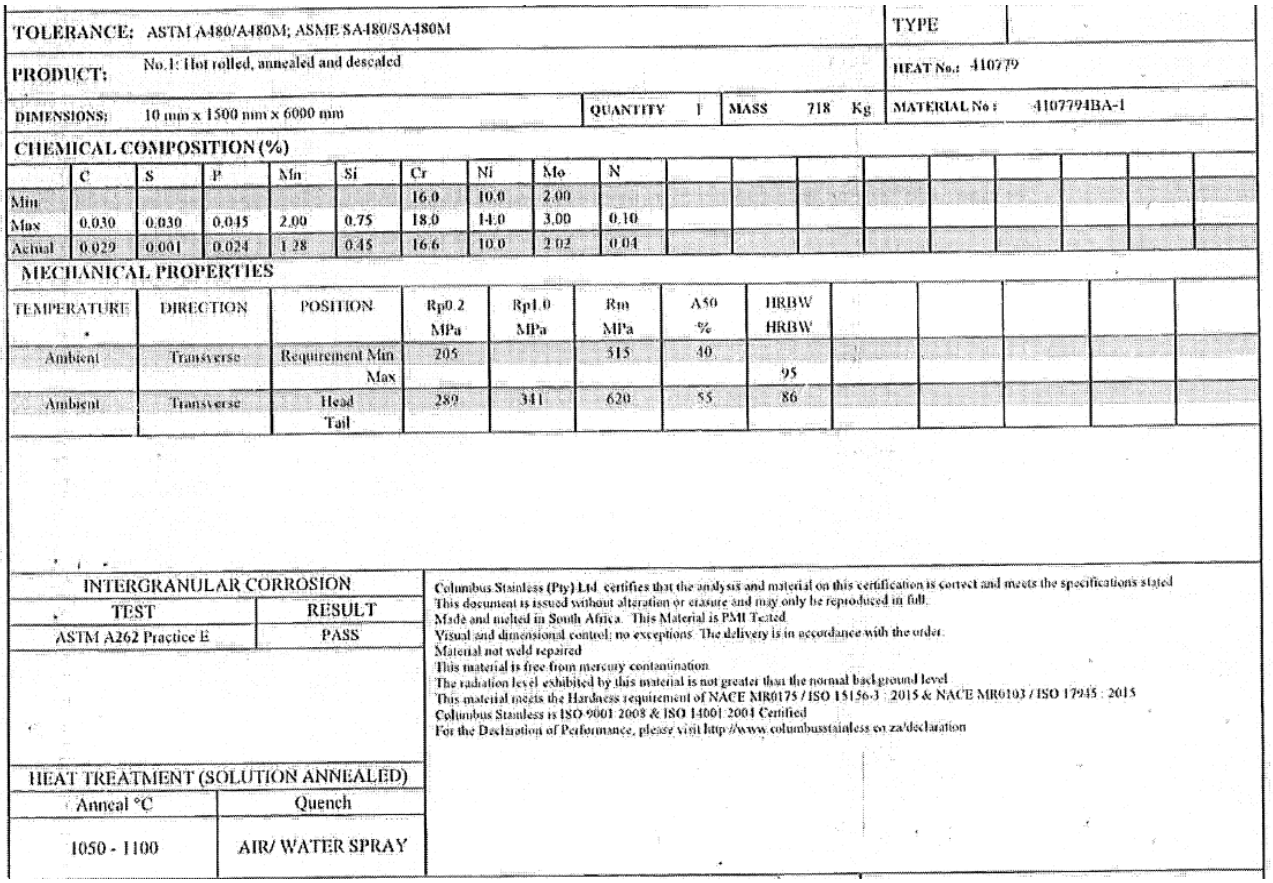

TOLERANCE: ASTM A480/A480M; ASME SA480/SA480M — TYPE

PRODUCT: No.1: Hot rolled, annealed and descaled — HEAT No.: 410779

DIMENSIONS: 10 mm x 1500 mm x 6000 mm — QUANTITY 1 — MASS 718 Kg — MATERIAL No.: 4107794BA-1

CHEMICAL COMPOSITION (%)

	C	S	P	Mn	Si	Cr	Ni	Mo	N
Min						16.0	10.0	2.00	
Max	0.030	0.030	0.045	2.00	0.75	18.0	14.0	3.00	0.10
Actual	0.029	0.001	0.024	1.28	0.45	16.6	10.0	2.02	0.04

MECHANICAL PROPERTIES

TEMPERATURE	DIRECTION	POSITION	Rp0.2 MPa	Rp1.0 MPa	Rm MPa	A50 %	HRBW HRBW
Ambient	Transverse	Requirement Min	205		515	40	
		Max					95
Ambient	Transverse	Head	289	341	620	55	86
		Tail					

INTERGRANULAR CORROSION	
TEST	RESULT
ASTM A262 Practice E	PASS

HEAT TREATMENT (SOLUTION ANNEALED)

Anneal °C	Quench
1050 - 1100	AIR/ WATER SPRAY

Columbus Stainless (Pty) Ltd certifies that the analysis and material on this certification is correct and meets the specifications stated
This document is issued without alteration or erasure and may only be reproduced in full.
Made and melted in South Africa. This Material is PMI Tested
Visual and dimensional control; no exceptions. The delivery is in accordance with the order.
Material not weld repaired
This material is free from mercury contamination
The radiation level exhibited by this material is not greater than the normal background level
This material meets the Hardness requirement of NACE MR0175 / ISO 15156-3 : 2015 & NACE MR0103 / ISO 17945 : 2015
Columbus Stainless is ISO 9001:2008 & ISO 14001:2004 Certified
For the Declaration of Performance, please visit http://www.columbusstainless.co.za/declaration

Figure 62: 361L Stainless Steel Material Certificate

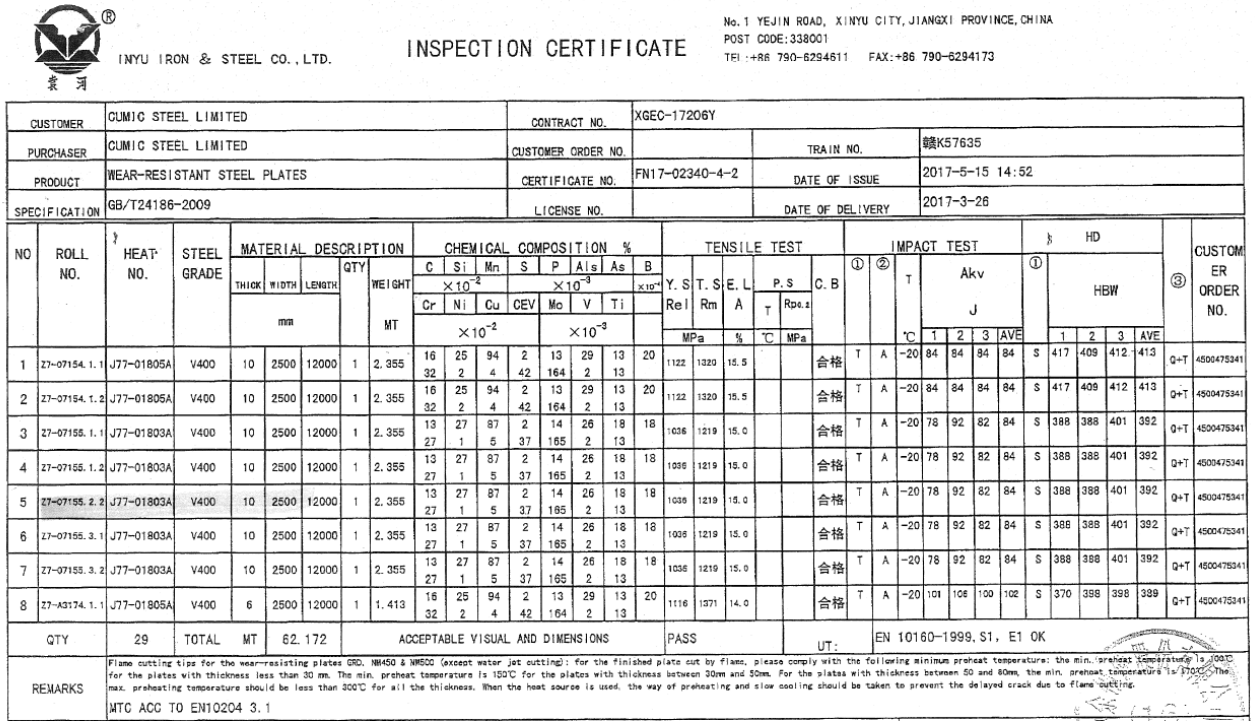

XINYU IRON & STEEL CO., LTD.

INSPECTION CERTIFICATE

No. 1 YEJIN ROAD, XINYU CITY, JIANGXI PROVINCE, CHINA
POST CODE: 338001
TEL: +86 790-6294611 FAX: +86 790-6294173

CUSTOMER	CUMIC STEEL LIMITED	CONTRACT NO.	XGEC-17206Y
PURCHASER	CUMIC STEEL LIMITED	CUSTOMER ORDER NO.	TRAIN NO. 赣K57635
PRODUCT	WEAR-RESISTANT STEEL PLATES	CERTIFICATE NO. FN17-02340-4-2	DATE OF ISSUE 2017-5-15 14:52
SPECIFICATION	GB/T24186-2009	LICENSE NO.	DATE OF DELIVERY 2017-3-26

NO	ROLL NO.	HEAT NO.	STEEL GRADE	MATERIAL DESCRIPTION THICK (mm)	WIDTH (mm)	LENGTH (mm)	QTY	WEIGHT (MT)	CHEMICAL COMPOSITION % C (×10⁻²)	Si (×10⁻²)	Mn (×10⁻²)	S (×10⁻³)	P (×10⁻³)	Als (×10⁻³)	As (×10⁻³)	B (×10⁻⁴)	Cr (×10⁻²)	Ni (×10⁻²)	Cu (×10⁻²)	CEV (×10⁻²)	Mo (×10⁻³)	V (×10⁻³)	Ti (×10⁻³)	TENSILE TEST Y.S ReL (MPa)	T.S Rm (MPa)	E.L A (%)	P.S T (℃)	P.S Rp0.2 (MPa)	C.B	IMPACT TEST ①	②	T (℃)	Akv J 1	2	3	AVE	HD ① HBW 1	2	3	AVE	③	CUSTOMER ORDER NO.
1	Z7-07154.1.1	J77-01805A	V400	10	2500	12000	1	2.355	16	25	94	2	13	29	13	20	32	2	4	42	164	2	13	1122	1320	15.5			合格	T	A	-20	84	84	84	84	S	417	409	412	413	Q+T	4500475341
2	Z7-07154.1.2	J77-01805A	V400	10	2500	12000	1	2.355	16	25	94	2	13	29	13	20	32	2	4	42	164	2	13	1122	1320	15.5			合格	T	A	-20	84	84	84	84	S	417	409	412	413	Q+T	4500475341
3	Z7-07155.1.1	J77-01803A	V400	10	2500	12000	1	2.355	13	27	87	2	14	26	18	18	27	1	5	37	165	2	13	1036	1219	15.0			合格	T	A	-20	78	92	82	84	S	388	388	401	392	Q+T	4500475341
4	Z7-07155.1.2	J77-01803A	V400	10	2500	12000	1	2.355	13	27	87	2	14	26	18	18	27	1	5	37	165	2	13	1036	1219	15.0			合格	T	A	-20	78	92	82	84	S	388	388	401	392	Q+T	4500475341
5	Z7-07155.2.2	J77-01803A	V400	10	2500	12000	1	2.355	13	27	87	2	14	26	18	18	27	1	5	37	165	2	13	1036	1219	15.0			合格	T	A	-20	78	92	82	84	S	388	388	401	392	Q+T	4500475341
6	Z7-07155.3.1	J77-01803A	V400	10	2500	12000	1	2.355	13	27	87	2	14	26	18	18	27	1	5	37	165	2	13	1036	1219	15.0			合格	T	A	-20	78	92	82	84	S	388	388	401	392	Q+T	4500475341
7	Z7-07155.3.2	J77-01803A	V400	10	2500	12000	1	2.355	13	27	87	2	14	26	18	18	27	1	5	37	165	2	13	1036	1219	15.0			合格	T	A	-20	78	92	82	84	S	388	388	401	392	Q+T	4500475341
8	Z7-A3174.1.1	J77-01805A	V400	6	2500	12000	1	1.413	16	25	94	2	13	29	13	20	32	2	4	42	164	2	13	1116	1371	14.0			合格	T	A	-20	101	106	100	102	S	370	398	398	389	Q+T	4500475341
QTY		29	TOTAL MT	62.172			ACCEPTABLE VISUAL AND DIMENSIONS																	PASS					UT:	EN 10160-1999, S1, E1 OK													

REMARKS

Flame cutting tips for the wear-resisting plates GRD, NM450 & NM500 (except water jet cutting): for the finished plate cut by flame, please comply with the following minimum preheat temperature: the min. preheat temperature is 100℃ for the plates with thickness less than 30 mm. The min. preheat temperature is 150℃ for the plates with thickness between 30mm and 50mm. For the plates with thickness between 50 and 80mm, the min. preheat temperature is 175℃. The max. preheating temperature should be less than 300℃ for all the thickness. When the heat source is used, the way of preheating and slow cooling should be taken to prevent the delayed crack due to flame cutting.

MTC ACC TO EN10204 3.1

Figure 63: VRN 400 Material Certificate

DATA SHEET

Material: MP 92 Standard Applications

Material Composition	Unit	Value
SiO_2	%	5.37
Fe_2O_3	%	0.055
Al_2O_3	%	92.28
TiO_2	%	0.041
CaO	%	0.49
MgO	%	0.83
K_2O	%	0.25
Na_2O	%	0.59

Physical Properties:

Property	Unit	Value
Bulk Density	$g*cm^{-3}$ minimum	3.55
Porosity	%	0.0
Water Absorption	%	0.01
Modulus of Rupture	MPa minimum	240
Modulus of Elasticity	GPa	295
Fracture Toughness	$MN*m^{-2/3}$	3.0
Vickers Hardness HV (5kg)	$kg*mm^{-2}$	1023
Abrasion Resistance	cm^3h^{-1} maximum	0.30
Thermal Expansion	$*10^{-6}K^{-1}$ (400°C) $*10^{-6}K^{-1}$ (800°C) $*10^{-6}K^{-1}$ (1000°C)	6.66 7.92 8.26
Thermal Conductivity	$W*m^{-1}K^{-1}$	15

Figure 64: 92% Alumina Tile Material Data Sheet

DATA SHEET

Material: MP96 Standard Applications

Chemical Composition

Material Composition	Unit	Value
Al_2O_3	%	96.0
SiO_2	%	1.7
MgO	%	1.4
CaO	%	0.8

Physical Properties

Property	Units	Typical Value
Bulk Density	$g*cm^{-3}$	3.75
Porosity	%	0.0
Water Absorption	%	0.0
Modulus of Rupture	MPa	280
Modulus of Elasticity	GPa	330
Fracture Toughness	$MN*m^{-3/2}$	3.5
Vickers Hardness	$kg*mm^2$ (5kgf)	1 277
Thermal Expansion	$10^{-6}°C^{-1}$ (400°C) $10^{-6}°C^{-1}$ (800°C) $10^{-6}°C^{-1}$ (1000°C)	6.66 7.98 8.31
Thermal Conductivity	$W*m^{-1}*K^{-1}$	23
Maximum temperature	°C	1 500
Sound Velocity	$m*s^{-1}$	10 100

Figure 65: 96% Alumina Tile Material Data Sheet

Ingredient	Formula	Cas#	Typical Composition
Aluminium Oxide	Al_2O_3	1344-28-1	95.0%
Titanium Oxide	TiO_2	13463-67-7	3.0%
Silicon Oxide	SiO_2	7631-86-9	1.5%
Iron Oxide	Fe_2O_3	1309-37-1	0.2%
Magnesium Oxide	MgO	1309-48-4	0.1%
Calcium Oxide	CaO	1305-78-8	0.1%

Figure 66: Aluminium Oxide Abrasive Properties

Appendix B : QEMSCAN Results

Table 19: Condensed QS Minerals (PF samples)

Condensed QS Minerals	Power Station D	Power Station C	Power Station B	Power Station A
Kaolinite	30.4	26.4	31.1	22.1
Quartz	14.8	4.5	10.7	7.6
Vitrinite	18.7	25.1	28.6	21.4
RSF	13.9	19.0	9.4	20.0
Fusinite	12.8	15.3	9.0	18.9
Other	9.4	9.7	11.2	10
Total	100	100	100	100

Table 20: Particle proportions (PF samples)

Particle proportions	Power Station D	Power Station C	Power Station B	Power Station A
Sandstone	10.8	2.5	1.8	3.8
Siltstone	4.7	1.7	10.5	2.5
Mudstone	14.7	15.4	18.4	7.4
Carbominerite	32.8	22.8	28.4	30
Reactive intermediate	15.1	22.3	6.6	26.3
Vitrite (RSF)	14.1	26.0	26.7	17.7
Other	7.8	9.3	7.6	12.3
Total	100	100	100	100

Table 21: Ash reconciliation (PF samples)

Particle proportions	Power Station D	Power Station C	Power Station B	Power Station A
Ash (particles)	47.2	31.9	44.3	31.3
Ash (QS modal)	47.3	32.4	44.3	31.6
Ash (db)	42.7	30.1	34.2	30.9

Table 22: Fly ash mass%

Fly ash mass%	Power Station D	Power Station C	Power Station B
Aluminosilicate (Kaolinite)	49.10	55.10	40.00
Quartz	20.30	10.00	39.50
Aluminosilicate glass	21.30	24.7	9.10
Other	9.30	10.20	11.40
Total	100	100	100

Table 23: Total slagging (Fly ash samples)

Total slagging	Power Station D	Power Station C	Power Station B
Fly ash Mass% slagging	24.49	26.38	14.93
Fly ash slagging kg/hr 1MWt	23.30	13.67	8.87

(QEMSCAN false colour image – coal)

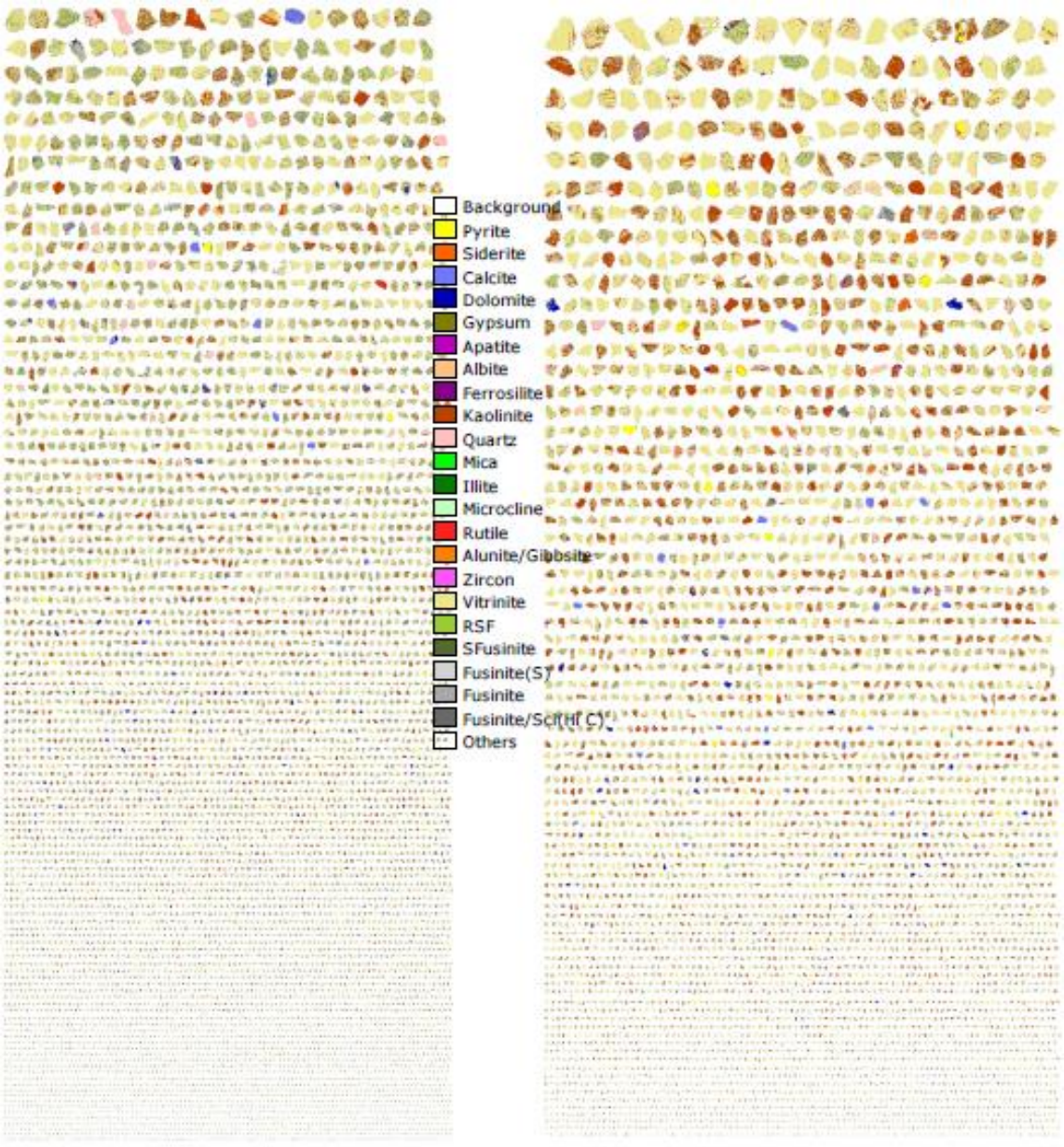

Figure 67: Power station A (left) and Power station B (right) PF

(QEMSCAN false colour image – coal)

Figure 68: Power station C (left) and Power station D (right) PF

(QEMSCAN false colour image – fly ash)

Figure 69: Power station D fly ash

(QEMSCAN false colour image – fly ash)

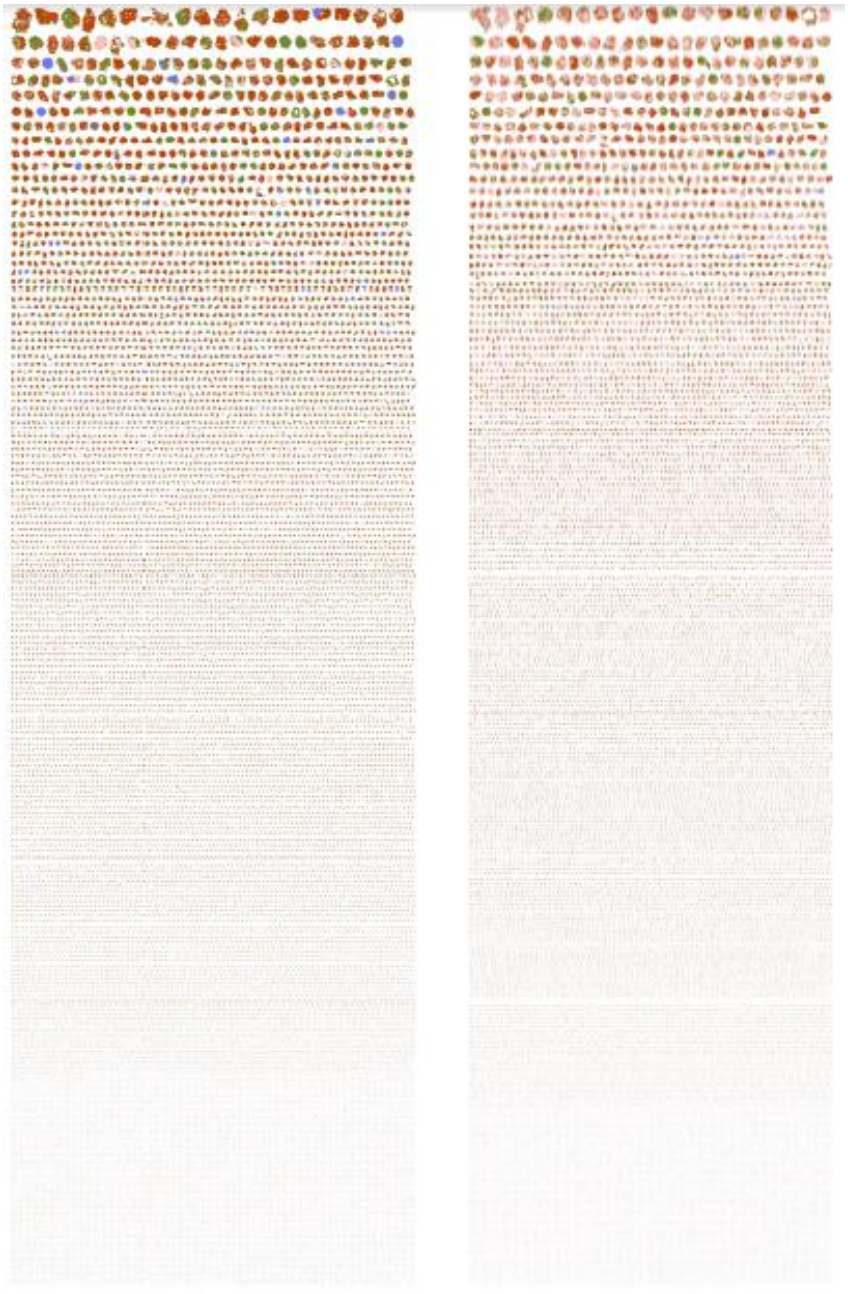

Figure 70: Power station C (left) and Power station B (right) fly ash

Table 24: Indicative mineral and particle compositions in SiO_2 and Al_2O_3

	SiO_2	**Al_2O_3**
Iron Titanium Oxide	0.3	7.1
Steel	0.1	0.5
Scale: Calcite/Lime/Anhydrite	0	0
Iron Silicate	0	4.9
Aluminium Oxide	0	70.7
Clay: Fe-Al-Silicate/Kaolinite	0.8	10.7
Sand: Quartz/Feldspar	98.7	5.9
Spinel	0	0.2

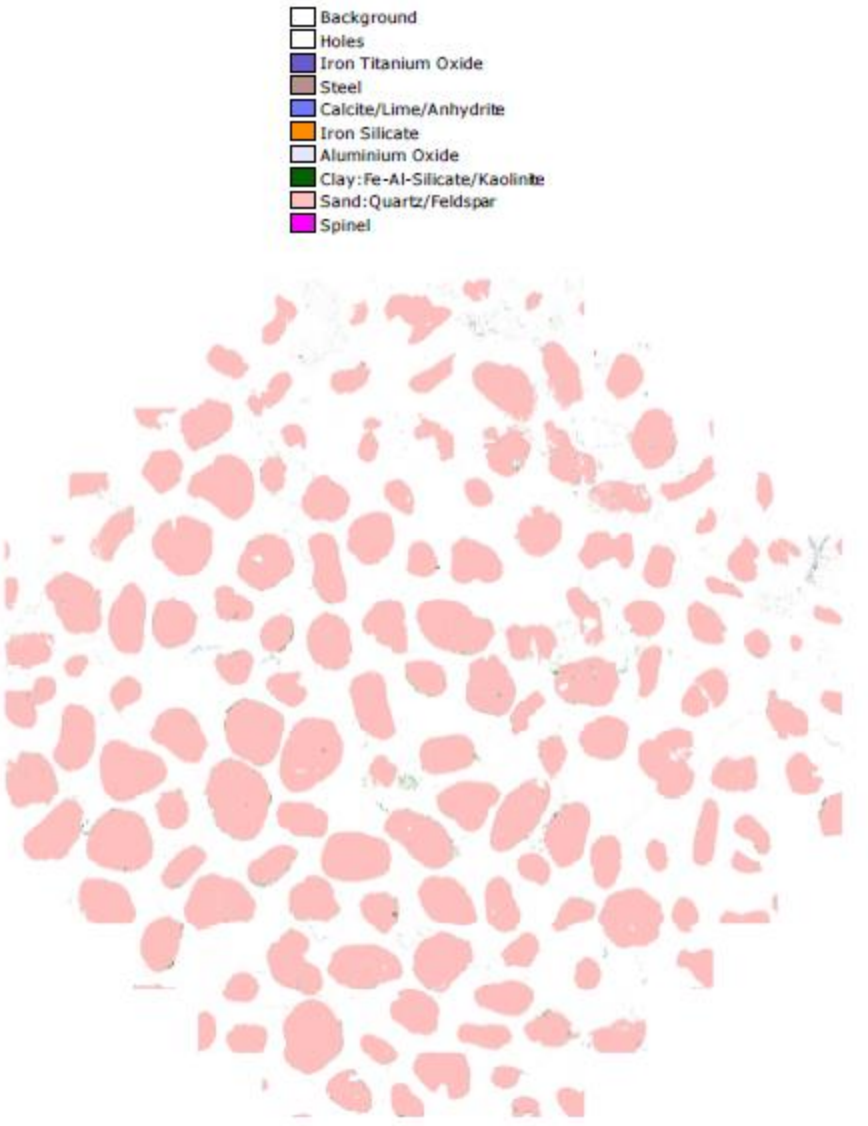

Figure 71: SiO_2 abrasive

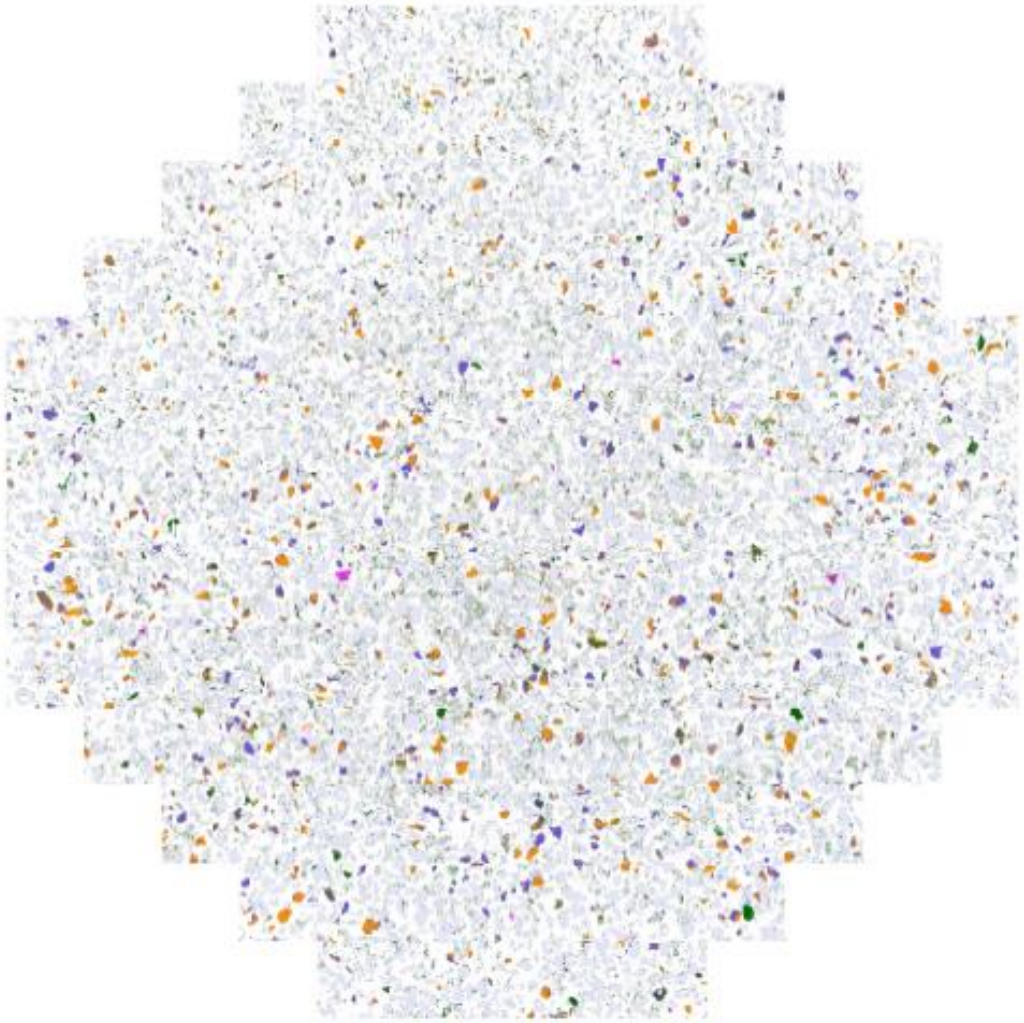

Figure 72: Al_2O_3 abrasive

Appendix C : Experimental Results

Table 25: Carbon steel erosion results

Impact angle (°)	Velocity (m/s)	Temperature (°C)	Sample ID	Time (min)	Weight before (g)	Weight after (g)	Erosion Rate (mg/min)	Abrasive Flow Rate (g/min)	Specimen Density (g/cm^3)	Erosion value (mm^3/g)	Erosion value with experimental error (mm^3/g)
30	30 ± 2	Ambient	J	10	46,2011	45,8601	34,1	1,9248	8,3	2,134	2,134 ± 0,194
			K	10	46,4522	46,1319	32,03	1,9248	8,3	2,005	2,005 ± 0,182
			3	10	48,3121	47,9671	34,5	2,0178	8,3	2,06	2,06 ± 0,187
			4	10	47,3538	47,0112	34,26	2,0523	8,3	2,011	2,011 ± 0,183
			5	10	46,5623	46,2086	35,37	2,0523	8,3	2,076	2,076 ± 0,189
60	30 ± 2	Ambient	A	10	45,9946	45,906	8,86	1,642	8,3	0,65	0,65 ± 0,059
			B	10	45,4586	45,3722	8,64	1,642	8,3	0,634	0,634 ± 0,058
			C	10	45,5546	45,4692	8,54	1,642	8,3	0,627	0,627 ± 0,057
			6	10	45,6761	45,5689	10,72	2,0523	8,3	0,629	0,629 ± 0,057
			7	10	45,8761	45,7682	10,79	2,0523	8,3	0,633	0,633 ± 0,058
90	30 ± 2	Ambient	G	10	45,9012	45,8434	5,78	1,642	8,3	0,424	0,424 ± 0,039
			H	10	45,2375	45,1784	5,91	1,642	8,3	0,434	0,434 ± 0,039

			1	10	45,4202	45,3507	6,95	2,0178	8,3	0,415	0,415 ± 0,038
			2	10	48,6351	48,5631	7,2	2,0523	8,3	0,423	0,423 ± 0,038
			8	10	48,9861	48,9152	7,09	2,0523	8,3	0,416	0,416 ± 0,038

Table 26: VRN400 erosion results

Impact angle (°)	Velocity (m/s)	Temperature (°C)	Sample ID	Time (min)	Weight before (g)	Weight after (g)	Erosion Rate (mg/min)	Abrasive Flow Rate (g/min)	Specimen Density (g/cm^3)	Erosion value (mm^3/g)	Erosion value with experimental error (mm^3/g)
30	30 ± 2	ambient	V3	10	45,7599	45,681	7,89	2,143	7,6	0,485	0,485 ± 0,040
			1	10	45,7169	45,5647	7,61	2,143	7,6	0,467	0,467 ± 0,039
			2	10	45,7854	45,5491	7,88	2,143	7,6	0,484	0,484 ± 0,040
60	30 ± 2	ambient	A	10	45,6839	45,612	7,19	2,2122	7,6	0,428	0,428 ± 0,036
			B4	10	44,3659	44,2926	7,33	2,2122	7,6	0,436	0,436 ± 0,036
			E	10	44,3554	44,2831	7,23	2,2122	7,6	0,43	0,43 ± 0,0360
90	30 ± 2	ambient	V4	10	45,8195	45,7535	6,60	2,143	7,6	0,405	0,405 ± 0,034
			C	10	45,7291	45,6626	6,65	2,2122	7,6	0,396	0,396 ± 0,033
			D	10	45,6641	45,5992	6,49	2,2122	7,6	0,386	0,386 ± 0,032

Table 27: 96% Alumina tile erosion results

Impact angle (°)	Velocity (m/s)	Temperature (°C)	Sample ID	Time (min)	Weight before (g)	Weight after (g)	Erosion Rate (mg/min)	Abrasive Flow Rate (g/min)	Specimen Density (g/cm^3)	Erosion value (mm^3/g)	Erosion value with experimental error (mm^3/g)
30	30 ± 2	Ambient	X	10	28,2876	28,2501	3,75	1,9248	4,1	0,475	0,475 ± 0,034
			Y	10	27,9857	27,9487	3,7	1,9248	4,1	0,469	0,469 ± 0,034
			Z6	10	28,1019	28,0633	3,86	1,9248	4,1	0,489	0,489 ± 0,035
60	30 ± 2	Ambient	A	10	28,5202	28,4698	5,04	2,0212	4,1	0,608	0,608 ± 0,043
			B6	10	28,2992	28,2477	5,15	2,0212	4,1	0,621	0,621 ± 0,044
			C	10	27,9509	27,9	5,09	2,0212	4,1	0,614	0,614 ± 0,044
90	30 ± 2	Ambient	D	10	27,2079	27,1451	6,28	2,0212	4,1	0,758	0,758 ± 0,054
			E6	10	28,0477	27,9834	6,43	2,0212	4,1	0,776	0,776 ± 0,055
			F	10	27,6927	27,6298	6,29	2,0212	4,1	0,759	0,759 ± 0,054

Table 28: 92% Alumina tile erosion results

Impact angle (°)	Velocity (m/s)	Temperature (°C)	Sample ID	Time (min)	Weight before (g)	Weight after (g)	Erosion Rate (mg/min)	Abrasive Flow Rate (g/min)	Specimen Density (g/cm^3)	Erosion value (mm^3/g)	Erosion value with experimental error (mm^3/g)
30	30 ± 2	ambient	X	10	29,1995	29,1492	5,03	2,212	3,6	0,632	0,632 ± 0,045
			Y2	10	26,9209	26,8696	5,13	2,212	3,6	0,644	0,644 ± 0,046
			Z	10	27,8183	27,7673	5,1	2,212	3,6	0,64	0,64 ± 0,046
60	30 ± 2	ambient	X	10	25,5047	25,4542	5,05	1,9248	3,6	0,729	0,729 ± 0,052
			5	10	26,2249	26,1763	4,86	1,9248	3,6	0,701	0,701 ± 0,050
			C2	10	26,1867	26,1328	5,39	1,9248	3,6	0,778	0,778 ± 0,056
90	30 ± 2	ambient	7	10	25,8474	25,7919	5,55	1,9248	3,6	0,801	0,801 ± 0,057
			E	10	29,2429	29,1792	6,37	2,212	3,6	0,8	0,8 ± 0,057
			F2	10	26,1308	26,0663	6,45	2,212	3,6	0,81	0,81 ± 0,058

Table 29: 316L stainless steel erosion results

Impact angle (°)	Velocity (m/s)	Temperature (°C)	Sample ID	Time (min)	Weight before (g)	Weight after (g)	Erosion Rate (mg/min)	Abrasive Flow Rate (g/min)	Specimen Density (g/cm^3)	Erosion value (mm^3/g)	Erosion value with experimental error (mm^3/g)
30	30 ± 2	ambient	A1	10	47,5613	47,4835	7,78	2,1426	7,9	0,4596	0,4596 ± 0,038
			6	10	47,3979	47,3182	7,97	2,1426	7,9	0,4709	0,4709 ± 0,039
			S3	10	47,558	47,4798	8,22	2,1426	7,9	0,462	0,462 ± 0,038
60	30 ± 2	ambient	1	10	47,1382	47,0541	8,41	2,1426	7,9	0,4969	0,4969 ± 0,041
			2	10	47,3811	47,2972	8,39	2,1426	7,9	0,4957	0,4957 ± 0,041
			Y1	10	47,1234	47,0413	8,21	2,1426	7,9	0,485	0,485 ± 0,040
90	30 ± 2	ambient	3	10	47,6828	47,6108	7,2	2,1426	7,9	0,4254	0,4254 ± 0,035
			8	10	47,3953	47,3253	7	2,1426	7,9	0,4136	0,4136 ± 0,034
			9	10	47,7746	47,7032	7,14	2,1426	7,9	0,4218	0,4218 ± 0,035